IMPERIAL COLLEGE LONDON

BARIUM TITANATE: PHOTOPHYSICS, PHOTOCATALYSIS & THE INFLUENCE OF THE FERROELECTRIC EFFECT

A Doctoral Thesis

by

MADELEINE RACHEL MORRIS

Submitted in partial fulfilment of the requirements for the degree of
Doctor of Philosophy

in the

PLASTIC ELECTRONICS CENTRE FOR DOCTORAL TRAINING
DEPARTMENT OF PHYSICS

AUGUST, 2018

Declaration of Authorship

I hereby declare that the material presented within this thesis is the result of my own work, except where appropriate references are made to contributions by others. This thesis has not been submitted, in whole or in part, in any previous application for a degree, at this or any other university.

Madeleine Rachel Morris
August, 2018

Abstract

Photocatalytic and photoelectrochemical water splitting processes remain hindered by fast recombination of photogenerated electrons and holes. Ferroelectric materials are increasingly being considered to address this issue; their internal electric fields have been shown to spatially separate electrons and holes, and thus should greatly reduce recombination rates. A kinetic understanding of the extent to which electron–hole recombination can be slowed in ferroelectric materials is essential to ascertain if they can play a significant role in achieving higher solar-driven water splitting efficiencies.

The focus of this thesis is an experimental investigation of charge carrier dynamics in barium titanate ($BaTiO_3$) to observe the effect of internal electric fields on recombination rates. Time-resolved spectroscopic techniques were used in conjunction with photocatalysis studies to determine whether ferroelectricity can significantly reduce recombination rates and lead to enhanced performance. It is found that, although the transient absorption spectrum of ferroelectric $BaTiO_3$ is similar to previously reported metal oxides, the carrier lifetimes are significantly longer, indicating the potential for ferroelectrics to be used in devices limited by fast electron–hole recombination.

In the first results chapter, the transient absorption spectrum of single crystal $BaTiO_3$ is characterised under inert atmosphere over two timescales: femtosecond–nanosecond and microsecond–second. Absorption signals due to photogenerated holes and electrons are identified using electron and hole scavengers, respectively. Comparisons are drawn between $BaTiO_3$ and other single crystal, but non-ferroelectric, metal oxides. It is found that, on timescales relevant for water oxidation, lifetimes in $BaTiO_3$ are at least an order of magnitude longer.

In the second results chapter, the origin of long carrier lifetimes in ferroelectric $BaTiO_3$ is explored. When the polarisation is switched off by both temperature and nanostructuring, carrier lifetimes decrease by four orders of magnitude. Recombination rates in $BaTiO_3$ exhibit a much stronger temperature dependence than other metal oxides, which is rationalised by considering the temperature dependence of the spontaneous polarisation.

The third results chapter investigates the photocatalytic performance of $BaTiO_3$ nanopowders. It is found that, in the presence of an electron scavenger, $BaTiO_3$ photogenerated holes are reactive and can oxidise water to produce oxygen. Transient and photoinduced absorption spectroscopies indicated that hole accumulation in a $BaTiO_3$ sample with a higher tetragonal (ferroelectric) content, which translates to higher rates of oxygen evolution.

The final results chapter probes the influence of a ferroelectric $BaTiO_3$ substrate on α-Fe_2O_3 thin films. Preliminary data suggests the internal field can penetrate through the film and slow electron–hole recombination rates in α-Fe_2O_3.

Acknowledgements

Too often, it is said that the journey of a PhD student should be a solo one. For me, this couldn't be further from the truth, and without the long list of people I have to thank I certainly wouldn't have completed this journey.

Firstly, I must express my gratitude to my supervisor, James Durrant. For recognising when I needed a push and when I needed support, and for the opportunity to work in such a fantastic research group. But mostly, I thank him for the care and respect he continues to show to this group. Thanks also to Steve Dunn for his enthusiastic co-supervision during the first years of research, and for making things seem less insurmountable over a cup of coffee.

Much of my guidance has, of course, come from the postdocs. Steph — thank you for (bravely!) starting this journey with me. Ludmilla — thank you for (bravely!) joining me for the final stretch. And Laia and Ernest — you've both been bravely there throughout, and for this I am eternally grateful. For your help with pretty much everything from technical glitches to scientific discussions to — most importantly — emotional support, I thank you.

Thanks also to Steve's group at QMUL, particularly Joe, who was always welcoming and who provided some much needed expertise. Further thanks to Prof Jongin Hong and his research group in CAU for engaging in a fruitful collaboration, and for making me feel so welcome during my time in Seoul.

Thank you to the whole Durrant team, past and present. I feel truly lucky to have worked with such an exceptionally intelligent and sociable group of people. I will always look fondly on my time here, particularly the cake club, gin club, cups of tea, coffee and (occasional) crossword, political and scientific debates, ceilidhs, endless laughter and copious amounts of beer. Particular thanks must go to Andy, Camilo, Ching-Hong, Dan, Ernest, Hyojung, Jiaying, JK, Laia, Li, Ludmilla, Michael, Pabitra, Robert, Sacha, Scot, Seb, Shababa, Steph, Stoichko, Yifan and Yuhan.

Thanks also to the PE-CDT and wider CPE, Climate-KIC and Imperial communities for the excellent opportunities I've been given over the years. A huge thanks to Cohort 5 for their helpful discussions over the years, but mostly for their camaraderie and the laughs that came with it. Special thanks to Jason, Alex, IainA, IainH and Gwen for their friendship over the years — the pay-day dinners, winter school fun, laughs and countless beers will always be remembered.

I am forever grateful to my parents, sisters and wider family for their unwavering love, support and for their faith in me. Thank you for always being proud of me and for showing your interest, even when my own faltered.

Finally, I owe my thanks to Nathan. Thank you for always being there. For celebrating every high and supporting every low. For believing what I couldn't. Without you I'm not sure I could have reached this point.

Contents

List of Figures

List of Tables

Chapter 1

Introduction

> *"And if in a distant future the supply of coal becomes completely exhausted, civilization will not be checked by that, for life and civilization will continue as long as the sun shines! If our black and nervous civilization, based on coal, shall be followed by a quieter civilization based on the utilization of solar energy, that will not be harmful to progress and to human happiness."*
>
> GIACOMO CIAMICIAN, 1912

1.1 Context and motivation

Extreme weather events; catastrophic disease outbreaks; threats to food and clean water security; the disappearance of islands — and the peoples and cultures on them — due to rising sea levels; biological annihilation. We have been warned to expect all of these within our own lifetime, or within our grandchildren's, unless we make a serious effort to halt the warming of our planet.[1, 2]

In December 2015, the 21st Conference of the Parties (COP21) of the United Nations Framework Convention on Climate Change (UNFCCC) was held in Paris. Negotiated by 196 countries, the result of this event (as well as many years' worth of previous negotiations) was the 'Paris Agreement,' which entered into force on 4th November 2016 after a critical mass of 55 Parties completed the ratification process. The deal marks the first ever agreement which legally binds governments to limit global temperature rises to a level widely declared by climate scientists, social scientists and policymakers to be the threshold above which the consequences of climate change become irreversible and catastrophic.[*] Although widely hailed as a positive historic marker of global cooperation on this issue, the Paris Agreement is an ambitious venture which highlights the urgency with which world leaders must act to avoid approaching the 2 ℃ target.

To translate the 2 ℃ temperature rise into a more easily quantifiable figure, it is helpful to talk in terms of the harmful 'greenhouse gas' (GHG) emissions (expressed as gigatons of carbon dioxide, Gt CO_2, or 'carbon emissions'), which will lead to this warming. The 'carbon budget' is a model which estimates the remaining CO_2 that can be emitted whilst still maintaining

---

[*] Although the 2 ℃ limit is the current universally accepted 'magic number' for climate change and the focus of the Paris Agreement, its scientific basis is somewhat dubious. First proposed in the European Union (EU) in 1996, the figure has a range of critics from both the scientific and economic fields. The details of this debate and validity of the 2 ℃ target are beyond the scope of this thesis and will not be discussed here. For a detailed discussion of this topic, numerous publications are accessible, for example that by Randalls, 2010.[3]

a likely chance of limiting global temperature rises to below the agreed target. Figure 1.1(a) shows historic and projected cumulative CO_2 emissions. The two shaded areas indicate where carbon ‘spending’ breeches the limits above which temperature rises of 2 and 3 ℃ have a probability of 66 to 90 %.[4] Findings suggest that these breeches could be reached as soon as 2037 (2 ℃ rise) and 2069 (3 ℃ rise) if the status quo is maintained.

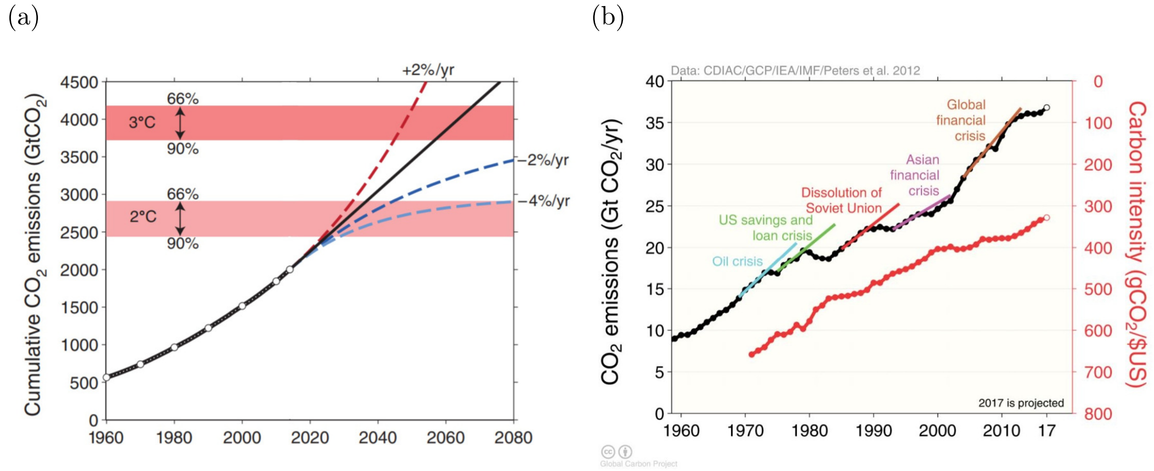

FIGURE 1.1: (a) Historic and projected cumulative global CO_2 emissions. Four simplified future pathways are illustrated: continued growth at the rate of +2 %/yr (dashed red line), based on trends over the past 15 years, constant emission at the rate measured in 2013 (i.e. zero growth in emissions, solid black line), and mitigation at rates of −2 %/yr (dark blue dashed line) and −4 %/yr (light blue dashed line). Shaded areas indicated emission levels where an associated global average temperature increase of 2 ℃ (lighter shade) and 3 ℃ (darker shade) have a probability of 66–90 %. Figure from ref [4]. (b) Apparent relationship between CO_2 emissions and economic activity. Emission intensities have dropped after financial crises, suggesting that economic growth is fueled by an increase energy usage. Figure from ref [5].

Clearly then, the status quo must be altered drastically to begin a downward trajectory of carbon emissions. Findings of the World Energy Outlook 2016 (WEO 2016) indicate that whilst the majority of countries are on track to achieve (and in some cases, exceed) the targets pledged in the Paris Climate Agreement, efforts will fall far short of limiting warming to less than 2 ℃.[6]

Disrupting ‘business as usual’ will undoubtedly be an immensely difficult and delicate challenge, not least because of the apparent correlation between economic growth and carbon emission intensity as illustrated in Figure 1.1(b).[5] A deceleration in carbon emission intensity has, in general, followed every financial crisis since the 1970s, quickly recovering along with the economy. It is likely that the correlation will continue for developing countries given the current global reliance on coal, oil and gas.[7, 8] This presents major ethical dilemmas. Should the developing countries be expected to curb their emissions to the same extent as the developed, at the risk of impeding economic growth and improving living standards? Or should the developed countries — those who have benefited the most from the industrial revolution — foot the bill for the damage caused, despite (allegedly) being unaware of the impact of their actions until relatively recently? The countries who emit the most GHGs export much of the harm thanks to the global intermixing of the Earth’s atmosphere; it’s been shown that those countries who have, historically, emitted the lowest levels of carbon emissions are generally the most vulnerable to the effects of climate change.[9] These most vulnerable countries are also more likely to have a much lower GDP, and thus will face a larger struggle in the attempt to adapt to a changing climate.[9] Some would argue that it is fossil fuel producers — ‘Big Oil’ — who are culpable and who should be held responsible for compensating those affected by the damage. At the time of writing, five of the largest oil companies in the US are facing a billion dollar lawsuit brought against them by New York City, with Paris exploring the possibility of doing the same.[10, 11]

What is clear is that climate justice will not be possible unless there is a clear alternative to our reliance on fossil fuels which can be rolled out globally, and which has the potential to benefit populations in both developed and developing countries in both the near- and long-term.

1.2 The case for renewable energy

The energy sector is responsible for at least two thirds of global carbon emissions and receives an annual investment of $\sim$ £1.3 trillion.[6] The current level of subsidies supporting fossil fuels stands at $>$ \$180 billion, whilst those supporting renewables is around half that, incentivising putting carbon *into* the atmosphere.[12] In 2015, this meant that the amount spent on fossil fuels equated to 6.5 % of the global gross domestic product (GDP).[13] To put this into perspective, the UK spends 5.6 % of its GDP on education.[14] Thus, energy could be seen as the biggest perpetrator of global warming, but also as potentially the biggest driver for positive change. With an ever-growing population and a massive 30 % rise in global energy demand expected by 2040 (that's equivalent to adding another China and India to today's global demand[12]), developing clean, secure, affordable and reliable sources of energy remains one of the greatest challenges of the 21st century.[15] The inherently erratic nature of renewable energies and continually fluctuating energy demand, along with a current shortfall in adequate large-scale electrical storage solutions, renders it unrealistic to assume that the energy crisis will be solved by technologies harnessing only one of these natural sources (solar, wind, hydro and wave, among others). Rather, the future will be one in which all renewables, along with storage solutions, form a diverse and sustainable energy infrastructure.

We are already seeing an increasing contribution from renewable energy sources in the global energy mix. 2016 was a year which saw renewables break numerous records, with solar leading the way. Almost two thirds of new net global power capacity came from renewable energy sources, boosted by a 50 % growth in solar photovoltaic (PV) capacity. This earned solar PV the title of fastest growing source of power in 2016, surpassing coal for the first time in history.[12] Discussion of renewables reaching significant milestones is no longer conducted on a scale of 50 years, but 5 years. By 2022, it is expected that renewable energy will grow by more than 33 % to $>$ 8000 TW h, contributing 25 % of power generation in the UK and an impressive 70 % in Denmark.[16] This rapid deployment has both been driven by and induced a massive reduction in cost; the cost of utility-scale electricity generation by solar PV has decreased by 73 % since 2010 with a further 57 % reduction expected by 2025.[17, 18] According to some estimates, the levelised cost of electricity in the U.S., without subsidies, is cheaper from both utility scale solar PV and wind than from either coal or nuclear.[19]

1.3 Solar potential

Of all the renewable energy sources, solar is by far the most abundant and has the greatest potential to be harnessed for human advantage.[20] Solar energy reaches the surface of the Earth at a rate of approximately 1×10^{14} kW. If only 0.1 % of this energy could be converted at an efficiency of only 10 % it would be four times the world's total generating capacity. In other words, the Sun can provide more than 7500 times the world's total annual primary energy consumption (which is $> 500 \times 10^{18}$ J).[21] In practical terms, solar has the potential to be a highly useful source of energy, despite it currently contributing < 1.5 % to the global energy consumption.[22] It can be harnessed in a variety of forms including electricity (by photovoltaics), heat (solar thermal) or chemical bonds (solar fuels). All have the potential to be zero carbon energy resources. It is a globally available energy source, and both solar thermal and solar PV can be used on large or small scales. While most developed countries are locked into an ailing and increasingly inefficient national grid system, microgeneration gives developing nations and areas the chance to bring more efficient electrification to the nearly 1.3 billion people who are currently off-grid.[23]

1.4 Energy storage

For solar and other renewable energies to be able to replace fossil fuels, a viable large-scale storage solution is necessary. The inherent generation intermittency — on both daily and yearly timescales — means that the integration of renewables into our energy infrastructure brings significant challenges to balance supply and demand. While battery technologies have advanced hugely in recent decades, it is unclear if they will become a viable solution for the national grid systems currently in place on the massive size- and time-scales needed; at present, they are not suitable for interseasonal storage, partly because of the vast amounts of energy needed to be stored. They also, in general, use toxic and/or rare elements (e.g. cadmium, lithium, cobalt), and thus large scale deployment may be problematic, particularly when waste management is considered.

Further, 35 % [24] of energy usage is in the transport sector. Our current infrastructure is such that the transport sector is almost entirely reliant on liquid fuels. Although electric vehicles have seen a seen a boost in recent years, there are doubts about the extent to which they can replace current technologies; it seems unlikely that batteries with large enough capacities will be developed within the necessary timescale to enable electrification of e.g. heavy goods vehicles, aircraft and ships, which require a high-energy-density fuel for viable operation. Thus, scalable solutions to storage and distribution challenges are required.

1.5 A hydrogen economy

One possible solution is transitioning to a 'hydrogen economy,' discussed for over a century not just in the scientific sector but in novels and the popular press.[15, 25–27] Hydrogen is the most abundant element on earth, and also has a higher specific energy (per unit mass) than any liquid fuel or battery (in compressed form). Table 1.1 lists the specific energy values of some common fuels and storage materials.

Although the energy per unit *mass* of H_2 is very high, the energy per unit *volume* — the 'energy density' — when compressed at 700 bar (the pressure you'd feel under 7 km of water) is, in fact, only around a quarter of that of petrol. This poses challenges in the storage of hydrogen, particularly when used as a transportable fuel as the tanks required to carry the H_2 can be heavy and expensive. These challenges are able to be overcome, as evidenced by the fact that hydrogen is already being used successfully and safely as a fuel for space shuttle

Table 1.1: Common storage materials, their specific energy values and some current usages.

Fuel/storage material	**Specific energy** ($MJ\,kg^{-1}$)	**Current uses**
Hydrogen (compressed at 700 bar)	142	Rocket engines
Diesel	48	Automotive engines
Gasoline (petrol)	46	Automotive engines
Jet fuel (kerosene)	43	Aircraft engines
Coal	30	Electric power plants, home heating
Alkaline battery	0.5	Home electronics
Lithium-ion battery	0.36–0.875	Automotive motors, home electronics
Lead-acid battery	0.17	Automotive engine ignition

launches and buses, with passenger trains proposed to be the next vehicles to run on this zero-emission fuel.[28–30]

However, although the hydrogen is zero-emission at the point of use (water is the only combustion product), its production methods are currently far from it. At present, around 95 % of hydrogen is generated from fossil fuels, predominantly by energy-intensive steam reforming of methane.[31] Until hydrogen can be produced sustainably, it has no place in a zero-carbon future. To find a sustainable production route, we can look to nature.

1.6 Artificial photosynthesis

Artificial photosynthesis imitates the natural photosynthetic process of storing energy in chemical bonds by converting sunlight, water and CO_2 into useful 'solar fuels,' plus O_2 as a waste product. Unlike solar photovoltaics, solar fuels could be used around the clock, storing chemical energy during the day which can be converted into electrical or mechanical energy both day and night.

As with the natural process, artificial photosynthesis can be split into oxidation and reduction reactions. The oxidation reaction (oxygen evolution reaction, 'OER,' Equation 1.1) is the same as natural photosynthesis, liberating protons and electrons (e^-), along with the waste product O_2.

$$2\,H_2O \longrightarrow O_2 + 4\,H^+ + 4\,e^- \tag{1.1}$$

Plants use these electrons and protons to generate their fuel — carbohydrate molecules (e.g. sugars) — in the reduction half of the process. In the biomimetric approach, a number of different reactions can be driven depending on the desired product. In close resemblance to plants, carbon fixation reactions can be used to generate small carbon-based molecules for use as fuels and chemical feedstocks, such as CO, HCO_2H, CH_3OH and CH_4, from atmospheric CO_2. As well as being chemically demanding, these fuels are carbon-based. Although such processes could help to close the carbon loop, the evidence overwhelmingly suggests that we must transition to a zero-carbon economy or risk irreversible and irreparable damage to our planet.

A more ideal, and indeed more simple, approach, then, is to use the protons and electrons formed during water oxidation to drive the hydrogen evolution reaction (HER, Equation 1.2).

$$2\,H^+ + 2\,e^- \longrightarrow H_2 \tag{1.2}$$

The overall water splitting reaction is then

$$2\,H_2O \xrightarrow{h\nu} 2\,H_2 + O_2 \tag{1.3}$$

Produced in this way — i.e. with sunlight ($h\nu$) as the only energy input — hydrogen can be considered a truly 'green' storable source of energy. Perhaps the most obvious way to do this is using separate photovoltaic and electrolysis modules, converting from solar to chemical energy via electricity. An alternative option is to build a fully integrated system which converts the sunlight directly into chemical energy. Each approach has its own pros and cons. While 'PV + electrolysis' relies on technologies which are already reasonably mature, it is still not cost competitive with traditional electrolysis (which uses fossil fuels as the source of the energy input) and may require several PV modules to generate a sufficiently high voltage to operate during periods of cloud or haze.[32] Direct solar water splitting — i.e. not via electricity — has the potential of reducing system complexity since no separate electrolyser is needed. A fully integrated system may also reduce the number of points of energy loss, and thus has the potential to be more efficient, but no viable system design has yet been achieved.

1.7 Current status of research

Fortunately for life on Earth, water is an incredibly stable substance, and its transparency to visible light means it will not decompose under normal solar irradiation. In order to split it to our benefit, therefore, we can employ a light-absorbing semiconductor to catalyse the reaction. Nature figured out how to do this hundreds of millions of years ago, and continues to do so at efficiencies which are adequate for its needs. But nature is not in a hurry and mankind is,[26] so although we have already created artificial systems which match the efficiencies of nature, we must find ways of converting sunlight into useful fuels at efficiencies ten times that for it to become viable for large-scale use.[33]

For a solar fuels technology to be deployed widely it must be 1) efficient 2) robust and 3) cost-effective. Prototypes currently exist which satisfy one or two of these criteria, but none satisfy all three. Efficiencies are hindered by e.g. insufficient visible light harvesting, poor collection of light-induced charges and undesirable back-reactions of products. The durability of a device is often limited by long-term sensitivity of the components to light or chemicals (including water), leading to degradation. A robust mechanism for gas separation must also be incorporated to allow safe and efficient collection of products. Costs are therefore often high not just because of the materials themselves (rare/precious metals are currently commonly used), but also because of the measures which must be taken to ensure these materials do not degrade over time, and the complex device architectures required for optimal performance.

Promisingly, the field of solar fuels is an extensive one which continues to expand, with dedicated research hubs and projects across the globe.[†] Researchers are continually on the search for new materials and device architectures which will allow us to increase solar-to-fuel

---

[†] e.g. Joint Center for Artificial Photosynthesis (JCAP, US), Korean Center for Artificial Photosynthesis (K-CAP, Republic of Korea), Towards BioSolar Cells (Netherlands)

efficiencies and create an affordable, robust, scalable and sustainable artificial photosynthesis system. To do this, an intimate understanding of the fundamental interactions between sunlight and semiconductors, and between semiconductors and water, is essential.

One of the common problems in current solar energy conversion devices is the difficulty in keeping electrons and holes (which are generated when a semiconductor absorbs sunlight) apart. To be able to harness all of the sunlight absorbed by a material, these charges must be separately collected. Their attraction to each other, however, means that without a driving force for separation they will recombine with each other. Clever materials design and device architecture can help overcome this recombination to some extent, however current water splitting devices typically require an external electrical energy input to function. This energy input induces an electric field across the device which pulls electrons and holes in opposite directions, reducing the likelihood of them recombining. Clearly, however, the requirement of a non-solar energy input is undesirable, so research to improve materials and/or device design is necessary.

Ferroelectric materials have an *inbuilt* electric field which could reduce electron–hole recombination without the need for an additional electrical energy input. Already, ferroelectrics are being used in devices and show promising signs of being able to enhance efficiencies. However, very little is understood about how the internal electric field can influence recombination rates, which limits the extent to which they can be used to maximise improvements. Although considered semiconductors, the presence of an internal field means that electronic properties of ferroelectrics doesn't conform to 'normal' semiconductor rules. To understand the behaviour, it is useful to study ferroelectric behaviour in the context of conventional semiconductor photocatalysis, and determine whether any differences in physical and/or chemical behaviour when illuminated with light is caused by the internal field.

This thesis explores the photophysical and photocatalytic behaviour of an archetypal ferroelectric, barium titanate, to improve the understanding of how these materials might be used to achieve more efficient solar energy conversion devices.

References

[1] Intergovernmental Panel on Climate Change, *Climate Change 2014: Impacts, Adaptation and Vulnerability*, tech. rep. (2014).

[2] G. Ceballos, P. R. Ehrlich, and R. Dirzo, "Biological annihilation via the ongoing sixth mass extinction signaled by vertebrate population losses and declines", *Proceedings of the National Academy of Sciences*, 201704949 **2017**.

[3] S. Randalls, "History of the 2 ° C climate target", *Wiley Interdisciplinary Reviews: Climate Change* 1, 598–605 **2010**.

[4] R. B. Jackson, P. Friedlingstein, J. G. Canadell, and R. M. Andrew, "Two or Three Degrees: CO2 emissions and Global Temperature Impacts", *Summer Issue of The Bridge on Energy, the Environment, and Climate Change* 45, 16–21 **2015**.

[5] G. C. Le Quéré, P. Peters, R. J. Andres, R. M. Andrew, T. Boden, P. Ciais, P. Friedlingstein, R. a. Houghton, G. Marland, R. Moriarty, S. Sitch, P. Tans, A. Arneth, A. Arvanitis, D. C. E. Bakker, L. Bopp, J. G. Canadell, L. P. Chini, S. C. Doney, A. Harper, I. Harris, J. I. House, a. K. Jain, S. D. Jones, E. Kato, R. F. Keeling, K. K. Goldewijk, A. Körtzinger, C. Koven, N. Lefèvre, A. Omar, T. Ono, G.-H. Park, B. Pfeil, B. Poulter, M. R. Raupach, P. Regnier, C. Rödenbeck, S. Saito, J. Schwinger, J. Segschneider, B. D. Stocker, B. Tilbrook, S. V. Heuven, N. Viovy, R. Wanninkhof, A. Wiltshire, and S. Zaehle, "Global Carbon Budget 2013", *Earth System Science Data Discussion* **2013**.

[6] International Energy Agency (IEA), *World Energy Outlook 2016*, tech. rep. (2016).

[7] C. Le Quere, "Global carbon budget 2017", *Earth System Science Data Discussions* 10, 405–448 **2017**.

[8] International Energy Agency (IEA), *Decoupling of global emissions and economic growth confirmed*, https://www.iea.org/newsroom/news/2016/march/decoupling-of-global-emissions-and-economic-growth-confirmed.html, 2016.

[9] G. Althor, J. E. Watson, and R. A. Fuller, "Global mismatch between greenhouse gas emissions and the burden of climate change", *Scientific Reports* 6, 1–6 **2016**.

[10] O. Milman, *New York City plans to divest $5bn from fossil fuels and sue oil companies*, https://www.theguardian.com/us-news/2018/jan/10/new-york-city-plans-to-divest-5bn-from-fossil-fuels-and-sue-oil-companies, 2018.

[11] M. Mattauch, *Paris explores climate lawsuit against fossil fuel companies*, https://350.org/press-release/paris-explores-climate-lawsuit-against-fossil-fuel-companies/, 2018.

[12] International Energy Agency, *World Energy Outlook 2017*, tech. rep. (2017).

[13] D. Coady, I. Parry, L. Sears, and B. Shang, "How Large Are Global Fossil Fuel Subsidies?", *World Development* 91, 11–27 **2017**.

[14] United Nations Development Programme, *Human development report 2016* (2016), p. 193.

[15] N. S. Lewis, and D. G. Nocera, "Powering the planet: chemical challenges in solar energy utilization.", *Proceedings of the National Academy of Sciences of the United States of America* 103, 15729–35 **2006**.

[16] International Energy Agency, *Renewables 2017: Executive Summary*, tech. rep. 42 (2017), pp. 20142–20142.

[17] International Renewable Energy Agency, *Power Generation Costs in 2017*, tech. rep. (2018), pp. 58–75.

[18] International Renewable Energy Agency, *The power to change: solar and wind cost reduction potential to 2025*, June (2016).

[19] Lazard, *Levelised Cost of Energy Analysis*, tech. rep. November (2017), pp. 1–21.

[20] A. Lopez, B. Roberts, D. Heimiller, N. Blair, and G. Porro, "U.S. Renewable Energy Technical Potentials: A GIS-Based Analysis", *National Renewable Energy Laboratory Document* 1, 1–40 **2012**.

[21] World Energy Council 2013, *World Energy Resources: Solar*, tech. rep. (2013), pp. 1–28.

[22] World Energy Council, *World Energy Resources 2016*, tech. rep. (2016), pp. 1–33.

[23] International Energy Agency (IEA), *Global Energy Trends to 2040* (2014), pp. 53–94.

[24] International Energy Agency (IEA), *Key World Energy Statistics 2017*, tech. rep. (2017), pp. 1–30.

[25] J. Vernes, *The Mysterious Island* (Pierre-Jules Hetzel, 1874).

[26] G. Ciamician, "The Photochemistry of the Future", *Science* 36, 385–394 **1912**.

[27] A. Eisenberg, *The answer is (artificially) blowing in the wind.* http://www.nytimes.com/2011/05/22/business/22novel.html, 2011.

[28] NASA, *Space Applications of Hydrogen and Fuel Cells*, https://www.nasa.gov/content/space-applications-of-hydrogen-and-fuel-cells, 2017.

[29] Aberdeen City Council, *Aberdeen City Region Hydrogen Strategy 2015-2025*, tech. rep. (2015), p. 27.

[30] Alstrom Press Centre, *Alstom's hydrogen train Coradia iLint first successful run at 80 km/h*, 2017.

[31] J. M. Ogden, "Prospects for Building a Hydrogen Energy Infrastructure", *Annual Review of Energy and the Environment* 24, 227–279 **1999**.

[32] M. S. Prévot, and K. Sivula, "Photoelectrochemical Tandem Cells for Solar Water Splitting", *The Journal of Physical Chemistry C* 117, 17879–17893 **2013**.

[33] R. E. Blankenship, D. M. Tiede, J. Barber, G. W. Brudvig, G. Fleming, M. Ghirardi, M. R. Gunner, W. Junge, D. M. Kramer, A. Melis, T. A. Moore, C. C. Moser, D. G. Nocera, A. J. Nozik, D. R. Ort, W. W. Parson, R. C. Prince, and R. T. Sayre, "Comparing Photosynthetic and Photovoltaic Efficiencies and Recognizing the Potential for Improvement", *Science* 332, 805–809 **2011**.

Chapter 2

Background and theory

> *"One shouldn't work on semiconductors. That is a filthy mess. Who knows if they really exist?"*
>
> Wolfgang Pauli

2.1 Semiconductor theory

2.1.1 Principles of semiconductor photocatalysis for solar fuels

When a semiconductor absorbs a photon of energy greater than its bandgap (E_g), an electron is excited from the valence band (VB) to the conduction band (VB), leaving behind a hole (h^+). These photogenerated charges can, provided a number of conditions be met, participate in surface chemical reactions. In the case of water splitting, for example, holes can oxidise water whilst electrons reduce protons. To successfully achieve both of these half reactions by the same semiconducting material, the band energies must 'straddle' the required potentials; that is, the valence band maximum must be more oxidative than the water oxidation potential (+1.23 V vs natural hydrogen electrode (NHE)) and the conduction band minimum must be more reductive than the proton reduction potential (0 V vs NHE). Further, E_g must be sufficiently large to provide the additional overpotential required to drive the overall reaction. So although the potential difference of water splitting is 1.23 V, the minimum bandgap required is, in practice, significantly higher, and has been proposed to be closer to 1.6 eV.[1]

Figure 2.1 illustrates two strategies for semiconductor-based photocatalytic water splitting systems. In particulate systems (Figure 2.1(a)), semiconductor nano- or micro-particles are suspended in water. Photogenerated electrons and holes migrate to the semiconductor/electrolyte interface to drive the redox reactions. These systems benefit from high surface areas and minimisation of the distance between the points of charge generation and interfacial reaction. However, since both half reactions occur on the same surface, the conduction *and* valence bands must match the energetic requirements. Moreover, the generation of both oxidation and reduction products on the same surface poses issues not only of short-circuit reactions (e.g. reduction of oxygen rather than protons) but of an explosive mix of oxygen and hydrogen. Thus, although this system has the potential to be low cost, identifying a single semiconductor which ticks all the boxes is non-trivial.

The photoelectrochemical cell set-up illustrated in Figure 2.1(b) provides an alternative route

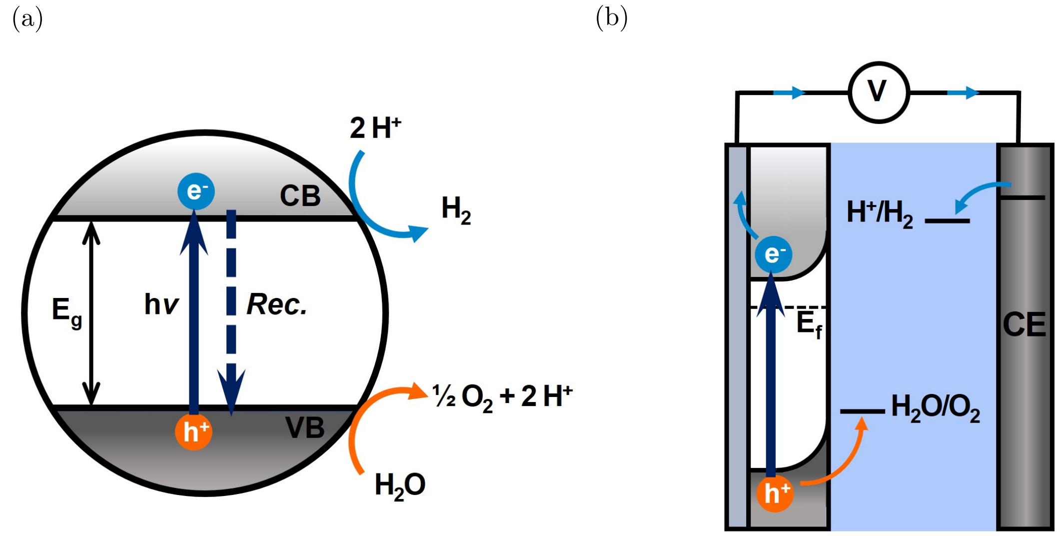

Figure 2.1: Schematic diagrams of key processes involved in semiconductor-based photocatalysis by (a) particulate suspension and (b) a photoelectrochemical cell (in which an n-type semiconductor functions as a photoanode). An ion-exchange membrane can be used to separate the two electrodes to allow for safer and more efficient systems.

to solar-driven water splitting which relaxes these conditions. Provided either the conduction or valence band energies can drive one of the half reactions (in this case, the valence band of the n-type photoanode can drive water oxidation), an external electrical bias can be applied between the photoanode and the counter electrode (CE). This provides the additional energy input required to drive the other redox reaction (proton reduction, here). As well as greatly expanding the number of earth-abundant, visible-light absorbing materials with appropriate energy levels, this approach has the advantage of spatially separating the reduction and oxidation reactions, which can facilitate safe and efficient product collection with the use of an ion-exchange membrane,[2] however this method requires energetic input in the form of an applied electrical bias.

The search for one material which satisfies all the requirements for an efficient, robust and affordable water splitting system is a complex one. Since the first demonstration of photoelectrochemical water splitting in the 1970s, no successful candidates have been identified which meet all three requirements.[3] Some satisfy one or two of the three requirements; TiO_2, for example, is low cost and very stable, but its wide bandgap means it absorbs little of the solar spectrum and therefore efficiencies are limited; III–nitrides (e.g. GaN, InN), on the other hand, have shown higher efficiencies and reasonable stabilities, but are hindered by high costs.[4, 5] An alternative strategy, inspired by the natural photosynthetic process, utilises two (or more) semiconductors in what is known as a ‘tandem’ or ‘z-scheme’ set-up. This allows for the selection of photocatalysts whose properties can be tailored to suit either the oxidation or reduction reactions, as well as more efficient utilisation of the solar spectrum, absorbing two photons per useful electron–hole pair. It is, however, a more complex approach than either the particulate or photoelectrochemical set-ups. A further option is to use a photovoltaic to provide the necessary voltage for electrolysis (PV + electrolysis), converting solar to chemical energy via electrical energy. This ‘brute force’ approach, although perhaps the most obvious, is limited by the price and availability of PV devices and electrolysers, and is currently not cost-competitive with traditional hydrogen production mechanisms.[6]

At present, it is not clear which — if any — of these strategies will ‘win’ the water splitting race. Each has advantages and disadvantages, and it may be the case that all will play their part in the changing energy infrastructure. It is therefore important that research efforts explore all potential possibilities to maximise the chance of finding the 'holy grail:' efficient, scalable, and sustainable solar-driven water splitting.

For the remainder of this thesis, the focus will be on particulate suspension and photoelectrochemical strategies, discussing how new materials and strategies might overcome some of their shortcomings and lead to improved efficiencies.

2.1.2 Metal oxides for solar water splitting

Metal oxides are considered some of the most promising materials to use as photoelectrodes for water splitting, particularly in the water oxidation half reaction.[7] Many exhibit desirable material properties such as high stability in water, resistance to photocorrosion and low toxicity. Their production methods are also generally low cost and up-scalable, so although higher efficiencies have been achieved using non-oxide materials (e.g. Si and III-V compound semiconductors), metal oxides continue to be the focus of much research.[8] Chemically, the four-electron process of the oxygen evolution reaction is the 'bottleneck' of overall water splitting due to its large overpotentials and slow reaction kinetics.[9, 10] As such, the designing of robust and photoactive photoanode materials is vital for developing this as a viable source of energy.

TiO_2, the first material reported to demonstrate photoelectrochemical oxidation of water,[3] remains one of the most extensively studied photoanode materials, despite being a wide bandgap semiconductor ($E_g = 3.0$–3.2 eV).[7, 11] α-Fe_2O_3 and $BiVO_4$, with narrower bandgaps of 2.2 and 2.4 eV, respectively, absorb considerably larger portions of the solar spectrum and have attracted much attention as photoanode materials.[12–15] Despite the large body of research, devices utilising these materials remain well below their theoretical maxima. The best reported $BiVO_4$ device reaches only ~ 58 % of it's maximum calculated photocurrent, whilst for α-Fe_2O_3 devices this is < 36 %.[16, 17] Photocurrents are limited by fast electron–hole recombination; hematite, in particular, suffers from high rates of recombination on ps–ns timescales.[12] TiO_2 devices tend to have fewer losses due to lower rates of recombination, with the most efficient attaining ~ 87 % of the maximum possible photocurrrent,[18] however its wide bandgap means that it can harvest < 5 % of the solar spectrum, limiting its usefulness.

2.1.3 Understanding charge carrier dynamics

Low absorption coefficients, poor electron conductivity and short hole diffusion lengths have all been identified as contributing factors to the high rates of electron–hole recombination which results in inadequate efficiencies of metal-oxide based devices.[13] Nanostructuring has been found to improve efficiencies (compared to using flat/dense materials) and indeed the most efficient devices using α-Fe_2O_3, TiO_2 and $BiVO_4$ are all nanostructured.[16–18] By reducing the distance between the point of charge generation and the surface of the material — where a driving force for charge separation exists in the form of band bending — electron–hole recombination rates should be reduced.[19] However, the remaining losses are large enough that no commercially viable system for solar fuels currently exists.

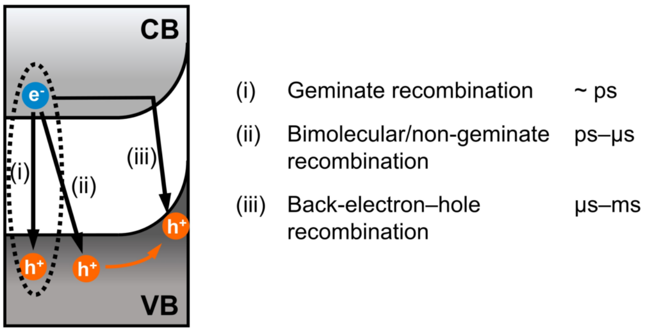

Figure 2.2: Schematic illustration of common electron–hole recombination pathways in metal oxides used for photoanodes, and the timescales on which they are generally observed to occur. (i) Some electron–hole pairs recombine before charge separation can occur. This is known as geminate recombination, and occurs on very fast (fs–ps) timescales. (ii) Bimolecular, or non-geminate, recombination usually occurs between free (charge separated) electrons and holes in the bulk. (iii) Photogenerated electrons which have initially been extracted from the material can come back into the material and recombine with holes accumulated at the surface. This process is often termed back electron–hole recombination, and is usually slower than bimolecular recombination (µs–ms).

To mitigate the losses, researchers must gain further understanding of photophysical and photochemical processes, and how they are affected by material properties and device architectures. To do this, we can continue to employ a range of time-resolved techniques to monitor photogenerated charge carrier dynamics. Photoelectrochemical techniques such as electrochemical impedance spectroscopy and transient photocurrent measurements, for example, have been used to study the kinetic behaviour of metal oxides including α-Fe_2O_3, TiO_2 and $BiVO_4$.[14, 20–23] Although these are useful techniques, obtained data correlates to electron dynamics, from which photogenerated hole dynamics must be inferred. Optical techniques such as time-correlated single photon counting (TCSPC), transient absorption spectroscopy (TAS) and photoinduced absorption spectroscopy (PIAS) can therefore be useful for investigating recombination in photoanode materials since both electron and hole dynamics can be directly — and independently — monitored.[12]

The main technique used throughout this thesis is TAS. This is a pump-probe spectroscopic technique which enables monitoring of recombination, trapping, charge transfer and reaction of both photogenerated electrons and holes. Unlike TCSPC, this technique can monitor non-radiative recombination, expected to be the more dominant decay pathway in metal oxides.[7] A further advantage of TAS is that it facilitates investigation of charge carrier dynamics over a range of timescales covering charge generation (femtoseconds) up to kinetically slow chemical reactions (typically milliseconds to seconds).[7] The use of chemical scavengers allows the spectral signatures of electrons and holes to be identified, facilitating the use of TAS to selectively monitor electrons or holes. This can be particularly useful for investigating the effects of external factors, such as applied bias, pH, and temperature, on the behaviour of charge carriers.

Our group, as well as others, has previously used TAS to study the charge carrier dynamics of a number of metal oxides, including TiO_2,[24–26] α-Fe_2O_3[12, 27] and $BiVO_4$.[14, 28] By using TAS on both ultrafast (fs–ns) and slow (µs–s) timescales, along with photoelectrochemical methods, three key loss processes have been identified in metal oxide photoanodes: (i) geminate recombination, occuring on $\sim$ ps timescales (ii) bulk electron/hole recombination, typically dominant from ps–µs and (iii) back electron–hole recombination (where holes accumulated in the space charge layer recombine with bulk electrons), usually observed µs–ms after photogeneration.[7] These recombination pathways are illustrated schematically in Figure 2.2.

The predominance and exact timescales of these processes can vary from material to material (and, indeed, between material polymorphs), however a common theme is that recombination is much faster than reaction rates. It has been demonstrated that rate constants of water oxidation on α-Fe_2O_3 surfaces are as low as 0.7 s^{-1}.[7] Poor charge separation and electron conductivity in this material means that significant electron–hole recombination occurs on the ps–µs timescale.[29–31] $BiVO_4$ and TiO_2 suffer from similarly sluggish reaction kinetics with typical rate constants on the order of $\sim 10^{-1}$–10^{1} s^{-1}, estimated by TAS studies.[7, 14, 32] The gross mismatch between reaction kinetics and electron–hole recombination rates indicates that enhancements in carrier lifetimes on the order of 10^3–10^9 are required to reach efficiencies which would enable commercialisation of solar-driven water splitting.[7] Applied biases on the order of a few hundred mV (often more) are currently required to achieve water splitting in α-Fe_2O_3, TiO_2 and $BiVO_4$ devices.[16–18] From a technological point of view, the requirement for an electrical energy *input* is clearly undesirable, and thus the end goal must be to identify a material and device architecture which facilitates unassisted water splitting.

Rather than applying an external electrical bias, device architectures — such as p–n junctions, heterojunctions and redox cascades — have been designed to produce a ‘built-in’ field to help drive electrons and holes in different directions. These approaches have resulted in devices which are more efficient than the sum of their parts, however can add challenges to the synthesis, processing and fabrication steps because of the more complex designs.[33, 34] An alternative, and potentially simpler, solution could be to take advantage of materials which have internal electric fields to drive electron–hole separation, thus enhancing carrier lifetimes. This was demonstrated spectroscopically by Shoaee et al. in 2014, where the internal electric field in a piezoelectric material (ZnO) was found to reduce bimolecular recombination in a hybrid organic–inorganic solar cell by a factor of three, which translated to an increase in conversion efficiency of up to 45 %.[35] Piezoelectrics, however, can only generate internal electric fields upon application of mechanical stress. Although useful for certain applications (e.g. where stray mechanical energy can be scavenged), a more straightforward option is to use a subset of piezoelectrics which have a permanent internal electric field — ferroelectrics.

2.2 Ferroelectric semiconductors

Ferroelectric materials are those which possess a permanent spontaneous polarisation, P_S, below a critical temperature known as the Curie temperature, T_C. A material is said to be ferroelectric when the polarisation has two or more stable states which can be switched upon application of a large enough external electric field (the coercive field, E_C).

2.2.1 Structure, dipole moments and the spontaneous polarisation

The existence of multiple stable polarisation states arises from an asymmetry in the crystal structure which is not present above the material’s Curie temperature. For example, $BaTiO_3$, a prototypical ferroelectric material, belongs to the cubic crystal system above its T_C of $\sim$ 120 °C (Figure 2.3(a)). This is a fully centrosymmetric structure in which all lattice elements are balanced, resulting in no net dipole moment in the unit cell. In this phase, $BaTiO_3$ is paraelectric (non-ferroelectric) — it can carry a *temporary* polarisation under application of

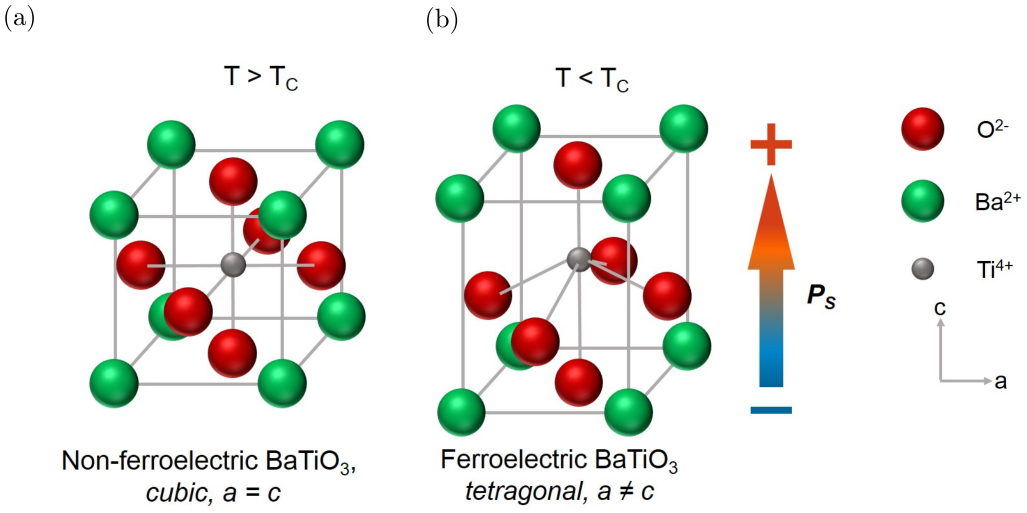

Figure 2.3: (a) Unit cell structure of $BaTiO_3$ above the Curie temperature, T_C. The arrangement of ions is fully centrosymmetric, belonging to the cubic crystal system, and thus is non-ferroelectric. (b) Unit cell structure of tetragonal $BaTiO_3$. The shift of the central Ti^{4+} with respect to the surrounding O^{2-} ions results in a net dipole within the structure, which can lead to macroscopic ferroelectricity.

an electric field, but this disappears upon its removal. On cooling below T_C, a phase transition occurs from cubic to tetragonal.* The dipole moment arises primarily due to the central Ti^{4+} ion shifting away from the centre with respect to the O^{2-} ions in the same plane. This elongates the c axis and lowers the symmetry of the unit cell. An inherent dipole moment is now present in the structure (Figure 2.3(b)). This results in a polarisation, defined as the total dipole moment (or charge) per unit volume.

$$P = \frac{\Sigma\mu}{V}$$

Depending on the direction of the ionic displacement, the polarisation direction will change (e.g. from 'up' to 'down') — applying a voltage $\geq E_C$ switches between these two states.

2.2.2 Depolarisation fields, domains and screening

The termination of P_S at the surface results in macroscopic charges at free ferroelectric surfaces (Figure 2.4). If left uncompensated, a depolarisation field, E_{dp}, will be generated in the opposing direction to P_S.[36] A material in which the polarisation is uniformly orientated across an entire single crystal is extremely rare, since this would generate a very large E_{dp}.[37] To minimise the electrostatic energy of the system, an unpoled ferroelectric will instead form multiple oppositely orientated 'domains' — areas of uniformly aligned polarisation direction. Domains in which the P_S is pointing towards the surface ('upwards') are known as $C+$ domains, whilst those with P_S pointing towards the bulk ('downwards') are termed $C-$ domains. Applying a potential greater than or equal to E_C will orient the polarisation vectors in a uniform direction, a process known as 'poling.'

---

* The tetragonal phase of $BaTiO_3$ is stable between 5 and ~ 120 °C. Below this, $BaTiO_3$ can exist in two further crystal phases (orthorhombic and rhombohedral), both of which are ferroelectric. Since all measurements throughout this thesis are conducted at temperatures above 5 °C, these low-temperature phases are not discussed further.

Further compensation of the surface charge can occur by internal and/or external 'screening' mechanisms. Movement of free charge carriers and defects in the bulk can internally neutralise the surface charge, whilst external screening occurs when ions or polar molecules are adsorbed onto the material surface, as demonstrated in Figure 2.4.

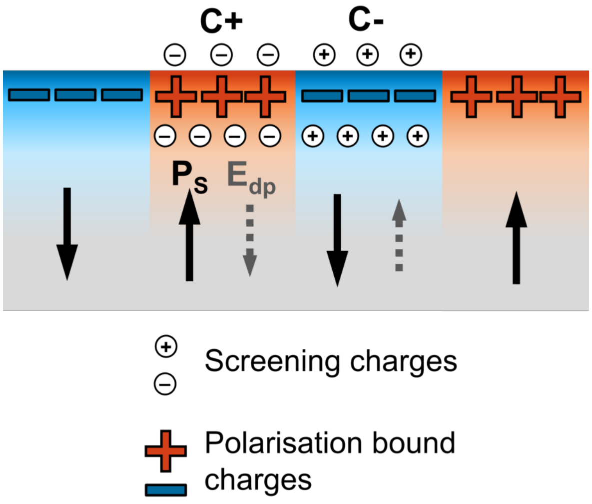

FIGURE 2.4: Schematic of polarisation directions and carrier movement in ferroelectric $BaTiO_3$. To minimise the surface charge caused by the spontaneous polarisation, P_S, any free carriers or mobile defects within the material will act to screen the surface charge (internal screening). Polar molecules and ions can also charge compensate by adsorbing to the surface (external screening).

2.2.3 Band bending in ferroelectrics

Ferroelectrics can be considered as wide bandgap semiconductors and thus analysis of their photo-physical and -chemical behaviour is often analogous to their conventional counterparts. However, the presence of an internal electric field introduces some fundamental differences, in particular in the behaviour of band bending at the surface of the material.

In conventional semiconductors, the conduction and valence band energy levels are flat throughout the entire material under inert atmospheres, i.e. they are equivalent in the bulk and at the surface.[†] When they are interfaced with another medium (e.g. an electrolyte), a redistribution of charge will occur until electronic equilibrium is reached. Electrons will initially flow across the junction until the Fermi energy, E_f, of the semiconductor equals the redox potential, E_{redox}, of the electrolyte. This movement of charge results in a region below the surface of the semiconductor known as the space charge layer (SCL), where the distribution of charge differs from the bulk of the material.[38] This deviation is known as 'band bending.' Figure 2.5 (a) and (b) demonstrates band bending in a conventional n-type semiconductor (where electrons are the majority carrier).

[†] This is true of ideal as well as intrinsic (undoped) semiconductors. For doped (intentionally or unintentionally) semiconductors, the Fermi level of any surface states can differ from that of the bulk, causing the appearance of band bending

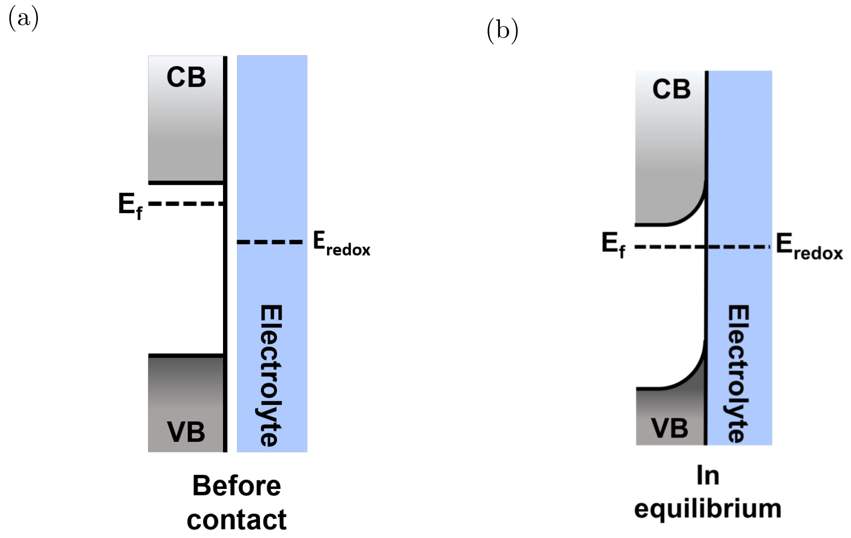

FIGURE 2.5: Energy band diagrams of an n-type semiconductor (a) before and (b) after contact with an electrolyte in the dark. Upon contact, electrons will flow from the semiconductor to the electrolyte until equilibrium is reached ($E_f = E_{redox}$). This leaves an electron-depleted region near the surface of the semiconductor and induces an electric field.

The band bending in ferroelectrics differs in that it exists even under inert atmospheres, and is the result of internal movement of charge carriers and defects from bulk to the surface of the material (internal screening), illustrated schematically in Figure 2.6. At $C+$ faces, the result of the positive polarisation and negative screening charges is downward band bending, whilst at $C-$ faces bands bend upwards relative to the bulk. Thus, the near-surface areas at free ferroelectric surfaces are comparable to the space-charge layers in conventional semiconductors, and can provide a driving force for photogenerated electron–hole separation. This kind of band bending is considered to dominate even when ferroelectrics are submerged in an electrolyte because of the need to screen the spontaneous polarisation.[36]

It has been demonstrated in the literature that the surface band bending associated with ferroelectric polarisation can have magnitudes of several hundred meV or greater, which is of similar scale to the bend bending at most p/n and semiconductor/electrolyte junctions.[39–41] Thus it can be expected that this band bending will act as an effective barrier to the recombination of electrons and holes generated near the surface, potentially eliminating the need for an additional driving force.

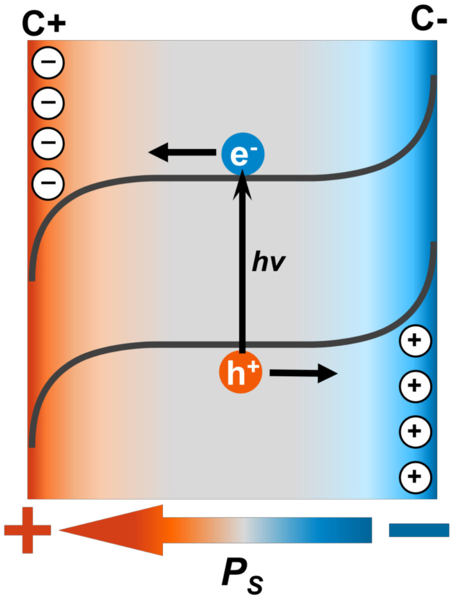

FIGURE 2.6: Depending on the direction of the polarisation vector, bending of the conduction and valence bands occurs at the material surface due to movement of internal free charges and defects. The band banding can provide a driving force for separation of photogenerated electrons and holes generated in generated close to the surface.

2.3 $BaTiO_3$ material properties

$BaTiO_3$, the first reported perovskite-type ferroelectric material, remains the most widely studied.[42] Its low-temperature ferroelectricity arises from structural frustration of the cubic structure, which occurs due to a misfit of B/A ions within the ABO_3 unit cell.[43] It has large P_S value of $26\,\mu C\,cm^{-2}$ which lies along the c-axis.[44] This material has a wide bandgap of $\sim$ 3.2 eV and is considered an n-type semiconductor largely due to the presence of oxygen vacancies.[45–47] Absorption of photons greater than or equal to this energy results in a charge transfer predominantly between the O $2p$ states at the VB maximum to the Ti $3d$ states at the conduction band minimum (some hybridisation of these states does occur). [45, 48] The extremely high relative permittivity (ϵ_r) of $BaTiO_3$ coupled with its ferroelectric nature has seen it being utilised in various fields of engineering, for example ceramic capacitors and ferroelectric memory devices.[49, 50] Although $BaTiO_3$ is a wide bandgap semiconductor, its low T_C of 120 °C makes it an excellent material for fundamental studies on the effect of internal electric fields on charge carrier dynamics — the non-ferroelectric phase is easily accessible, and thus information can be obtained from both ferro- and non-ferro-electric $BaTiO_3$ by conducting measurements below and above 120 °C. The valence band minimum and conduction band maximum of $BaTiO_3$ are reported to lie at approximately 2.9 and -0.3 V vs NHE, respectively.[11] To enable comparative studies with a non-ferroelectric metal oxide, we chose TiO_2, which has similar energetics and of which there is a myriad of studies in the literature.[11]

2.3.1 Ferroelectricity and size effects in $BaTiO_3$

The thermodynamically stable structure of bulk $BaTiO_3$ at room temperature is the ferroelectric tetragonal phase. However, it is well documented in the literature that by scaling ferroelectrics down to the nanometre scale, the dielectric properties will significantly deviate from the bulk. This size effect is a consequence of an instability in the polar (tetragonal) phase and results in suppression of ferroelectricity below a critical size. Thus, by nanostructuring, the cubic non-ferroelectric phase of $BaTiO_3$ can be accessed at room temperature. There is some uncertainty about the magnitude of this critical size, with some reports suggesting that ferroelectric polarisation will be suppressed in particles with diameters of less than $\sim$ 100 nm,[51–53] whilst others propose that ferroelectricity can persist in nanoparticles as small as a few nm.[54–56]

This uncertainty is perhaps unsurprising given that the reasons why a critical size exists, and what influences it, are not well understood. It is generally understood that there are both intrinsic and extrinsic factors which induce size effects.[57] Intrinsic factors are those relating to the nature of ultrafine particles. It has been suggested that in tiny particles, a huge depolarisation field is generated by the incomplete screening of P_S.[58] This induces a large free energy in the polar state, resulting in the non-polar (cubic, in the case of $BaTiO_3$) phase being thermodynamically more favourable. Extrinsic effects, such as surface stabilisation and disruption of long-range order caused by lattice defects and impurities, are also suggested to inhibit the formation of the ferroelectric phase at small dimensions.[53, 59] It has been shown that through careful control during synthesis, nanoparticles can be engineered to be either ferroelectric or non-ferroelectric at room temperature.[57]

Since the ferroelectric and non-ferroelectric forms of a material must belong to different crystal classes, structural determination can, to some extent, be used to determine the degree of ferroelectricity in a sample. It is, however, possible for cubic and tetragonal forms to coexist within a sample of $BaTiO_3$.[60] Notably, neither the bandgap nor the band positions are expected to differ between phases in $BaTiO_3$. This is in contrast to, e.g. TiO_2 polymorphs; anatase/rutile junctions are known have band energy offsets which can aid charge separation.[61] In mixed phase $BaTiO_3$, however, no enhancement in charge separation is expected at phase boundaries due to band alignments.[60, 62]

2.4 Ferroelectrics for solar energy conversion

The use of ferroelectrics for solar energy conversion has been explored for decades. The vast majority of studies have observed empirically that devices which incorporate ferroelectric materials behave differently from, and can in some cases outperform, their non-ferroelectric analogues. In almost all of these cases, the altered behaviour is attributed to spatial separation of photogenerated charge carriers, driven by the presence of spontaneous polarisation-induced band bending. Although there is an abundance of compelling evidence to support this theory, very little has been done in the way of spectroscopic analysis of charge carrier dynamics and recombination kinetics. The following subsections explore the empirical evidence indicating charge carrier separation in ferroelectrics in the contexts of photochemistry, photocatalysis, photoelectrochemistry and photovoltaics.

2.4.1 Ferroelectrics and surface photochemistry

Early studies utilising ferroelectric materials such as $Pb(Zr_xTi_{1-x})O_3$ (PZT) and $LiNbO_3$ for photochemical reactions were conducted which concluded that the polarisation within the material affected surface photochemistry.[63–65] The discussion was limited, however, until

2001 when Giocondi and Rohrer showed explicitly the influence of the internal polarisation of $BaTiO_3$ on the behaviour of photoinduced carriers.[66, 67] This work used photochemical redox reactions as 'local indicators' of the ferroelectric surface photochemical reactivity. When submerged in $AgNO_3$ and (separately) $Pb(ac)_2$ solutions and irradiated with super-bandgap light, solid deposits of Ag and PbO_2 occurred only on certain areas of the surface which coincided with $C+$ and $C-$ domains, respectively. This was attributed to the polarisation-induced band bending; upwards band bending at $C-$ surfaces promotes photogenerated hole accumulation (see Figure 2.6), and thus the oxidation of Pb^{2+} to Pb^{4+} was facilitated, whilst electrons and the associated reduction reaction were blocked. At $C+$ domain surfaces, the oxidation reaction is inhibited by the downwards band bending and instead the reduction reaction (Ag^+ to Ag) is promoted. These results were later echoed in the work of Kalinin et al. who manipulated the ferroelectric domains of both $BaTiO_3$ and PZT to induce alternating $C+/C-$ patterns on the surface on nm length scales.[68] Analogous experiments carried out on non-ferroelectric photoactive metal oxides (TiO_2 and $SrTiO_3$) did not show area-specific deposition, and provided compelling evidence that the domain specificity is associated with fundamental ferroelectric behaviour. Spatial separation of redox products has been observed in many ferroelectric materials, including PZT,[69–72] $LiNbO_3$[73, 74] and $BiFeO_3$.[75]

2.4.2 Ferroelectrics-enhanced performance

Photocatalytic dye degradation

Despite the earlier studies showing evidence of spatial separation of redox products on ferroelectric surfaces, examples of single phase ferroelectric-enhanced photocatalytic reactions are very few in the literature. A study conducted in 2013 by Cui et al. probed the influence of ferroelectricity on the photocatalytic decolourisation of Rhodamine B (RhB) dye molecules using $BaTiO_3$.[60] The rate of decolourisation was first obtained using a predominantly cubic sample of $BaTiO_3$ nanopowder. When this sample was annealed at high temperature, the tetragonal content increased because of particle size increase and stabilisation of the ferroelectric phase at room temperature. A three-fold increase in decolourisation rate was observed, despite the annealed sample having a much lower surface area, which was attributed to charge separation driven by ferroelectric polarisation.[60] The annealing process could, however, have altered the crystallinity and number of defects in the sample, which may also have affected the reaction rate. Su et al. later compared the photodecolourisation rates of RhB on $BaTiO_3$ nanopowders as small as 7.5 nm (and loaded with Ag) at 30 and 80 °C. The rate at 30 °C was observed to be faster than at 80 °C, consistent with a P_S close to zero due to a reduced T_C in very small nanoparticles. No such reduction in rate was observed at 80 °C in large nanoparticles (500 nm diameter), in which only a small reduction in P_S would be expected until reaching the Curie temperature of 120 °C, thus the reduced rate was attributed to poorer charge separation in the absence of an internal electric field. These particles are at the lower limit of the expected critical size for supporting a permanent polarisation, however characterisation techniques (P–E loops and Raman spectra) indicated the presence of the ferroelectric tetragonal phase.

Water splitting

$BaTiO_3$, with conduction and valence bands at very similar energies to those in TiO_2 (-0.5 and 2.7 V vs NHE, respectively), is thermodynamically suited for water oxidation as well as proton reduction, making it a possible candidate for overall water splitting.[11] Interestingly, photoelectrochemical water splitting was first investigated on $BaTiO_3$ single crystals by Nasby and Quinn in 1976,[76] shortly after Fujishima and Honda's seminal work using TiO_2.[3] They found that photoinduced currents of around 10^1 µA (for a device area of 0.18 cm^2) were produced under UV light, and that the $BaTiO_3$ electrode was stable under applied bias. Although the effect of ferroelectricity was not directly explored in this work (e.g. no poling was conducted), it was found that $BaTiO_3$ photoanodes could also produce very small photocurrents without an applied bias, unlike the TiO_2 single crystal photoanodes.[76] Few studies were conducted in the years following this on ferroelectric surfaces.[42] More recently, $BiFeO_3$, a visible light absorber, has been explored as a water splitting material.[77–79] Generally, it is accepted that its valence band is suited for water oxidation and has a bandgap of ~ 2.2 eV.[80, 81] In one study, however, epitaxially grown thin (~ 200 nm) films of ferroelectric $BiFeO_3$ were investigated with the aim of achieving unassisted water splitting under simulated solar light.[77] By poling the film, the authors found that they could slightly shift the onset potential by 0.016 V, and that the oxidation or reduction reaction could be promoted depending on the direction of polarisation.[77] Although photocurrents were on the order of just 10 $\mu A\,cm^{-2}$, this work demonstrates that, with careful domain engineering and/or polarisation, a single ferroelectric material could be used to achieve overall water splitting in which redox products are spatially separated on the material surface.

Ferroelectric/non-ferroelectric heterostructures

While these few studies have shown that ferroelectrics could potentially be useful as photoactive material in a device, much work has been conducted into devices which incorporate ferroelectrics as a functional layer alongside another photoactive semiconductor. Using local indicator reactions and photocatalytic studies, it has been found that the influence of P_S can extend beyond the ferroelectric surface through a very thin (10^1 nm) non-ferroelectric coating.[82–84] Very few (known) ferroelectrics are visible light absorbers, so the benefit of such a heterostructure is the opportunity to exploit the desirable properties of both the ferroelectric (enhanced spatial charge separation) and a suitable non-ferroelectric semiconductor (absorption of visible light, charge mobility, photoconductivity etc.).

A lot of the work has investigated $BaTiO_3/TiO_2$ heterostructures, possibly due to the band energy matching which does not inhibit (or, in fact, aid) charge transfer. Several studies have found that a thin film of TiO_2 on top of a ferroelectric exhibits modified reactivity depending on the polarisation of the ferroelectric, and in some cases improved photocatalytic activity compared to the bare TiO_2.[82–86] For example, Ag-loaded $BaTiO_3/TiO_2$ nanotubes showed higher photocurrents and photocatalytic reactivity for dye degradation than their components.[87] Photoelectrochemical water splitting on $BaTiO_3/TiO_2$ core/shell nanowire photoanodes was recently found to achieve a 67 % photocurrent density enhancement compared to pristine TiO_2 nanowires.[85] This again was attributed to improved charge separation by the internal electric field, but no monitoring of charge carrier dynamics was presented. Performance enhancements have been found using other ferroelectrics as substrates ($LiNbO_3$[88] and $PbTiO_3$[89]) and a wide range of morphologies (e.g. thin films,[82, 88] core/shell nanoparticles[86, 89] and nanotubes[87]).

While the studies of $BaTiO_3/TiO_2$ heterostuctures are valuable as a proof of principle, the wide bandgap of these materials (UV-absorbers) means that the benefits of such heterostructures in solar energy conversion are, of course, limited. $BiFeO_3$, one of the few visible light absorbing ferroelectrics ($E_g \sim 2.5$ eV[90]), has also been investigated in ferroelectric/non-ferroelectric heterostructures. Spatially selective deposits of Ag were again observed on surfaces of thin films of TiO_2 on $BiFeO_3$ substrates,[90] and $BiFeO_3/TiO_2$ core/shell nanopowders were found to exhibit fast photodegradation of an organic dye under visible light than pristine TiO_2 or $BiFeO_3$ nanoparticles, attributed to the presence of spontaneous polarisation in the ferroelectric core.[91] $BaTiO_3/\alpha$-Fe_2O_3 core/shell structures have also been investigated, which were found to decolourise RhB 2.5 times better than bare $BaTiO_3$ nanoparticles and 500 times faster than bare α-Fe_2O_3.[92] Interestingly, the enhanced performance was found not to be due to increased light absorption by α-Fe_2O_3; the heterostructured catalyst showed negligible performance under visible light, but superior performance under UV-light. The authors attributed the improved performance to efficient charge-carrier separation at the interface due to favourable band alignment and ferroelectric polarisation, and proposed that a junction between a ferroelectric substrate and non-ferroelectric photocatalyst could allow advantageous manipulation of charge transport.

2.4.3 Ferroelectrics and photovoltaics

A far larger body of work exists which explores the influence of ferroelectricity materials in solar photovoltaics (FE-PV), including in organic, organic–inorganic and inorganic solar cells.[35, 93, 94] The lack of centrosymmetry in ferroelectric materials leads to some interesting phenomena which can be useful in PV devices. Unlike with conventional semiconductors, a photovoltage can be generated in a uniform ferroelectric crystal under homogeneous light. In other words, the photovoltaic effect in these materials is not associated with separation of charge carriers at crystal inhomogeneities or p–n junctions, nor is it caused by diffusion of non-equilibrium carriers under non-uniform light.[95, 96] This is often termed the ‘bulk photovoltaic effect’ (BPVE) as it is thought the photovoltage is generated in the bulk of the material, without requiring an interface or junction for charge separation. Also of great interest is the ‘anomalous photovoltaic effect.’ This is the observation of ‘giant’ above-bandgap photovoltages in ferroelectric photovoltaic solar cells, which poses the possibility of exceeding the Schockley–Queisser limit for a single material.[97, 98] Exactly why ferroelectrics exhibit these phenomena is not well understood, however, with a number of models being proposed, and is beyond the scope of this thesis.

Several studies have reported increased solar–electric conversion efficiencies attributed to enhanced charge separation by the induced polarisation.[99–101] However, the evidence is again mostly empirical and based on device measurements (e.g. changes in open-circuit voltage and short circuit current values). The literature is lacking spectroscopic evidence of the extent to which the internal field can influence charge separation and/or recombination rates in these devices. Shoaee et al. investigated hybrid organic–inorganic solar cells which incorporated ZnO, which exhibits piezoelectricity, i.e. a voltage is generated when the material is put under mechanical stress.[35] Although several studies had previously utilised piezoelectrics in solar cells, the additional energy output of these was attributed to energy scavenging from the device surroundings.[102–104] That is, the devices converted both solar energy and stray mechanical energy (e.g. vibrations) to electrical energy, and the total efficiency was proposed to be simply the sum of the individual conversions. Shoaee et al. were the first to demonstrate a synergistic effect between the piezoelectric-induced polarisation and solar-to-electrical energy conversion efficiency, attributed to a decrease in bimolecular (non-geminate) recombination. Using transient absorption coupled with current–voltage measurements, an enhancement in conversion efficiency of up to 45 % was attributed to a three-fold increase in carrier lifetime, which was caused by polarisation-driven separation of photogenerated electrons and holes.[35] Since piezoelectrics only generate a polarisation under mechanical stress, expanding these studies to ferroelectrics will yield valuable information about how advantageous a permanent polarisation might be for solar energy conversion.

2.5 In this thesis

Although the use of ferroelectrics in solar energy conversion devices has been increasing in recent years, an understanding of how the internal electric field can inhibit electron–hole recombination is lacking. In order to use these materials to increase conversion efficiencies, it is vital to develop this knowledge. This thesis aims to investigate the photophysical and photocatalytic properties of a prototypical ferroelectric material, $BaTiO_3$, and determine to what extent they are influenced by the presence of ferroelectric polarisation. Transient absorption spectroscopy is used to gain an understanding of charge carrier dynamics in both ferroelectric and non-ferroelectric $BaTiO_3$. Observations are then compared to measurements of photocatalytic performance to determine the impact of ferroelectricity on activity.

This objective can be broken down into a series of aims:

1. **Understanding of charge carrier dynamics in ferroelectric $BaTiO_3$.** The photogenerated carrier dynamics of $BaTiO_3$ are not well understood. To understand how they are affected by internal electric fields, they must first be characterised. Since it is known that electron–hole recombination processes take place over a wide range of timescales, from fs to s, it is valuable to monitor decay kinetics on both ultrafast (fs–ps) and slower (µs–s) timescales.

2. **Identification of the transient absorption signals associated with photogenerated electrons and holes.** Few reports of time-resolved optical signals in $BaTiO_3$ exist, and none have identified the signatures of photogenerated electrons or holes. It is advantageous to identify the spectral 'fingerprints' particularly of photogenerated holes, so that an appropriate probe wavelength can be chosen when monitoring photocatalytic reactions such as water oxidation. Chemical electron and hole scavengers are used to allow the monitoring electron and hole decay kinetics on µs–s timescales (as these are the timescales on which water oxidation is expected to take place).

3. **Elucidation of the influence of internal electric fields on charge carrier dynamics.** Since the spontaneous polarisation in $BaTiO_3$ can be manipulated by temperature and nanostructuring, a comparison between decay kinetics in ferroelectric and non-ferroelectric $BaTiO_3$ can be made. Thus, information about the extent to which the ferroelectric polarisation affects electron–hole recombination kinetics can be gathered.

4. **Investigation of the effect of spontaneous polarisation on photocatalytic activity.** Dye degradation and water oxidation rates by ferroelectric and non-ferroelectric $BaTiO_3$ samples are compared. Correlating observational rates with spectroscopic studies gives valuable information about the potential rate enhancement caused by ferroelectric polarisation.

5. **Investigation of ferroelectric/non-ferroelectric heterostructures.** Thin films of α-Fe_2O_3 are deposited on ferroelectric $BaTiO_3$. Transient absorption measurements are taken to determine whether the substrate can influence charge carrier dynamics in the

non-ferroelectric thin film.

Impact

The research in this thesis is centred upon $BaTiO_3$, a wide-bandgap semiconductor. They are not intended to assess the potential for $BaTiO_3$ itself to be used in solar energy conversion devices. Rather, they are designed as fundamental studies to gain a better understanding of how ferroelectric materials in general could be implemented into devices where fast electron–hole recombination is a major loss pathway. Thus, it is expected that the results will be applicable to other ferroelectric materials. Further, the principles covered are expected to be applicable not only for the solar fuels field, on which these studies are centred, but also for solar photovoltaics in which fast electron–hole recombination is a major issue.

References

[1] A. J. Cowan, and J. R. Durrant, "Long-lived charge separated states in nanostructured semiconductor photoelectrodes for the production of solar fuels.", *Chemical Society reviews* 42, 2281–2893 **2013**.

[2] N. S. Lewis, "Developing a scalable artificial photosynthesis technology through nanomaterials by design", *Nature Nanotechnology* 11, 1010–1019 **2016**.

[3] A. Fujishima, and K. Honda, "Electrochemical photolysis of water at a semiconductor electrode", *Nature* 238, 37–38 **1972**.

[4] R. Pool, *Solar hydrogen: big ideas, small solutions*, http://spie.org/newsroom/09-2014-solar-hydrogen?highlight=x2358ArticleID%3Dx110173&SSO=1, 2014.

[5] Y. Hou, X. Yu, Z. A. Syed, S. Shen, J. Bai, and T. Wang, "GaN nano-pyramid arrays as an efficient photoelectrode for solar water splitting", *Nanotechnology* 27 **2016**.

[6] M. S. Prévot, and K. Sivula, "Photoelectrochemical Tandem Cells for Solar Water Splitting", *The Journal of Physical Chemistry C* 117, 17879–17893 **2013**.

[7] A. Kafizas, R. Godin, and J. R. Durrant, "Charge Carrier Dynamics in Metal Oxide Photoelectrodes for Water Oxidation", in *Semiconductors for photocatalysis*, 97 (2017), 3–46.

[8] J. W. Ager, M. R. Shaner, K. A. Walczak, I. D. Sharp, and S. Ardo, "Experimental demonstrations of spontaneous, solar-driven photoelectrochemical water splitting", *Energy Environ. Sci.* 8, 2811–2824 **2015**.

[9] A. J. Cowan, "Water oxidation: Intermediate identification", *Nature Chemistry* 8, 740–741 **2016**.

[10] Y.-f. Li, Z.-p. Liu, L. Liu, and W. Gao, "Mechanism and Activity of Photocatalytic Oxygen Evolution on Titania Anatase in Aqueous Surroundings Implementation of Parallel Periodic Continuum Solvation Model", 1–5 **2010**.

[11] J.-i. Fujisawa, T. Eda, and M. Hanaya, "Comparative study of conduction-band and valence-band edges of TiO 2 , SrTiO 3 , and BaTiO 3 by ionization potential measurements", *Chemical Physics Letters* 685, 23–26 **2017**.

[12] M. Barroso, S. R. Pendlebury, A. J. Cowan, and J. R. Durrant, "Charge carrier trapping, recombination and transfer in hematite (α-Fe2O3) water splitting photoanodes", *Chemical Science* 4, 2724–2734 **2013**.

[13] K. Sivula, F. Le Formal, and M. Grätzel, "Solar Water Splitting: Progress Using Hematite (α-Fe2O3) Photoelectrodes", *ChemSusChem* 4, 432–449 **2011**.

[14] Y. Ma, S. R. Pendlebury, A. Reynal, F. Le Formal, and J. R. Durrant, "Dynamics of photogenerated holes in undoped BiVO4 photoanodes for solar water oxidation", *Chemical Science* 5, 2964 **2014**.

[15] M. de Respinis, K. S. Joya, H. J. M. De Groot, F. D'Souza, W. A. Smith, R. van de Krol, and B. Dam, "Solar Water Splitting Combining a BiVO 4 Light Absorber with a Ru-Based Molecular Cocatalyst", *The Journal of Physical Chemistry C* 119, 7275–7281 **2015**.

[16] T. W. Kim, and K.-S. Choi, "Nanoporous BiVO4 Photoanodes with Dual-Layer Oxygen Evolution Catalysts for Solar Water Splitting", *Science* 343, 990–994 **2014**.

[17] J. Y. Kim, G. Magesh, D. H. Youn, J. W. Jang, J. Kubota, K. Domen, and J. S. Lee, "Single-crystalline, wormlike hematite photoanodes for efficient solar water splitting", *Scientific Reports* 3, 1–8 **2013**.

[18] M. Liu, N. de Leon Snapp, and H. Park, “Water photolysis with a cross-linked titanium dioxide nanowire anode”, *Chemical Science* 2, 80–87 **2011**.

[19] T. M. Gür, S. F. Bent, and F. B. Prinz, “Nanostructuring Materials for Solar-to-Hydrogen Conversion”, *The Journal of Physical Chemistry C* 118, 21301–21315 **2014**.

[20] F. Le Formal, S. R. Pendlebury, M. Cornuz, S. D. Tilley, M. Grätzel, and J. R. Durrant, “Back electron-hole recombination in hematite photoanodes for water splitting.”, *Journal of the American Chemical Society* 136, 2564–74 **2014**.

[21] B. Klahr, S. Gimenez, F. Fabregat-Santiago, J. Bisquert, and T. W. Hamann, “Electrochemical and photoelectrochemical investigation of water oxidation with hematite electrodes”, *Energy & Environmental Science* 5, 7626 **2012**.

[22] H. Cachet, and E. M. M. Sutter, “Kinetics of Water Oxidation at TiO 2 Nanotube Arrays at Different pH Domains Investigated by Electrochemical and Light-Modulated Impedance Spectroscopy”, *The Journal of Physical Chemistry C* 119, 25548–25558 **2015**.

[23] K. P. S. Parmar, H. J. Kang, A. Bist, P. Dua, J. S. Jang, and J. S. Lee, “Photocatalytic and photoelectrochemical water oxidation over metal-doped monoclinic BiVO4photoanodes”, *ChemSusChem* 5, 1926–1934 **2012**.

[24] J. Tang, J. R. Durrant, and D. R. Klug, “Mechanism of Photocatalytic Water Splitting in TiO 2 . Reaction of Water with Photoholes, Importance of Charge Carrier Dynamics, and Evidence for Four-Hole Chemistry”, *Journal of the American Chemical Society* 130, 13885–13891 **2008**.

[25] M. Sachs, E. Pastor, A. Kafizas, and J. R. Durrant, “Evaluation of Surface State Mediated Charge Recombination in Anatase and Rutile TiO 2”, *The Journal of Physical Chemistry Letters* 7, 3742–3746 **2016**.

[26] T. Yoshihara, R. Katoh, A. Furube, Y. Tamaki, M. Murai, K. Hara, S. Murata, H. Arakawa, and M. Tachiya, “Identification of Reactive Species in Photoexcited Nanocrystalline TiO 2 Films by Wide-Wavelength-Range (400-2500 nm) Transient Absorption Spectroscopy”, *The Journal of Physical Chemistry B* 108, 3817–3823 **2004**.

[27] S. R. Pendlebury, M. Barroso, A. J. Cowan, K. Sivula, J. Tang, M. Grätzel, D. Klug, and J. R. Durrant, “Dynamics of photogenerated holes in nanocrystalline α-Fe 2 O 3 electrodes for water oxidation probed by transient absorption spectroscopy”, *Chem. Commun.* 47, 716–718 **2011**.

[28] N. Aiga, Q. Jia, K. Watanabe, A. Kudo, T. Sugimoto, and Y. Matsumoto, “Electron-phonon coupling dynamics at oxygen evolution sites of visible-light-driven photocatalyst: Bismuth vanadate”, *Journal of Physical Chemistry C* 117, 9881–9886 **2013**.

[29] S. R. Pendlebury, A. J. Cowan, M. Barroso, K. Sivula, J. Ye, M. Grätzel, D. R. Klug, J. Tang, and J. R. Durrant, “Correlating long-lived photogenerated hole populations with photocurrent densities in hematite water oxidation photoanodes”, *Energy Environ. Sci.* 5, 6304–6312 **2012**.

[30] S. R. Pendlebury, X. Wang, F. Le Formal, M. Cornuz, A. Kafizas, S. D. Tilley, M. Grätzel, and J. R. Durrant, “Ultrafast charge carrier recombination and trapping in hematite photoanodes under applied bias.”, *Journal of the American Chemical Society* 136, 9854–7 **2014**.

[31] R. Milan, S. Cattarin, N. Comisso, C. Baratto, K. Kaunisto, N. V. Tkachenko, and I. Concina, “Compact hematite buffer layer as a promoter of nanorod photoanode performances”, *Scientific Reports* 6, 1–10 **2016**.

[32] A. J. Cowan, J. Tang, W. Leng, J. R. Durrant, and D. R. Klug, “Water Splitting by Nanocrystalline TiO 2 in a Complete Photoelectrochemical Cell Exhibits Efficiencies Limited by Charge Recombination”, *The Journal of Physical Chemistry C* 114, 4208–4214 **2010**.

[33] S. J. Hong, S. Lee, J. S. Jang, and J. S. Lee, “Heterojunction BiVO4/WO3 electrodes for enhanced photoactivity of water oxidation”, *Energy & Environmental Science* 4, 1781 **2011**.

[34] Y. Tachibana, L. Vayssieres, and J. R. Durrant, “Artificial photosynthesis for solar water-splitting”, *Nature Photonics* 6, 511–518 **2012**.

[35] S. Shoaee, J. Briscoe, J. R. Durrant, and S. Dunn, “Acoustic enhancement of polymer/ZnO nanorod photovoltaic device performance”, *Advanced Materials* 26, 263–268 **2014**.

[36] D. Tiwari, and S. Dunn, “Photochemistry on a polarisable semi-conductor: what do we understand today?”, *Journal of Materials Science* 44, 5063–5079 **2009**.

[37] L. M. Eng, “Nanoscale domain engineering and characterization of ferroelectric domains”, *Nanotechnology* 10, 405–411 **1999**.

[38] M. Grätzel, “Photoelectrochemical cells”, *Nature* 414, 338–344 **2001**.

[39] S. Dunn, and D. Tiwari, “Influence of ferroelectricity on the photoelectric effect of LiNbO3”, *Applied Physics Letters* 93, 092905–1 **2008**.

[40] A. Höfer, M. Fechner, K. Duncker, M. Hölzer, I. Mertig, and W. Widdra, “Persistence of Surface Domain Structures for a Bulk Ferroelectric above TC”, *Physical Review Letters* 108, 087602 **2012**.

[41] N. G. Apostol, L. E. Stoflea, G. A. Lungu, C. A. Tache, D. G. Popescu, L. Pintilie, and C. M. Teodorescu, “Band bending at free Pb(Zr,Ti)O3 surfaces analyzed by X-ray photoelectron spectroscopy”, *Materials Science and Engineering B: Solid-State Materials for Advanced Technology* 178, 1317–1322 **2013**.

[42] M. A. Khan, M. A. Nadeem, and H. Idriss, “Ferroelectric polarization effect on surface chemistry and photo-catalytic activity: A review”, *Surface Science Reports* 71, 1–31 **2016**.

[43] R. E. Cohen, “Origin of ferroelectricity in perovskite oxides”, *Nature* 358, 136–138 **1992**.

[44] W. J. Merz, “Double hysteresis loop of BaTiO3 at the curie point”, *Physical Review* 91, 513–517 **1953**.

[45] I. Grinberg, D. V. West, M. Torres, G. Gou, D. M. Stein, L. Wu, G. Chen, E. M. Gallo, A. R. Akbashev, P. K. Davies, J. E. Spanier, and A. M. Rappe, “Perovskite oxides for visible-light-absorbing ferroelectric and photovoltaic materials.”, *Nature* 503, 509–12 **2013**.

[46] G. Lewis, and C. Catlow, “Defect studies of doped and undoped barium titanate using computer simulation techniques”, *Journal of Physics and Chemistry of Solids* 47, 89–97 **1986**.

[47] C. N. Berglund, and H. J. Braun, “Optical Absorption in Single-Domain Ferroelectric Barium Titanate”, *Physical Review* 164, 790–799 **1967**.

[48] H. Salehi, N. Shahtahmasebi, and S. Hosseini, “Band structure of tetragonal BaTiO3”, *The European Physical Journal B - Condensed Matter* 32, 177–180 **2003**.

[49] J. F. Scott, and C. A. Paz de Araujo, “Ferroelectric Memories”, *Science* 246, 1400–1405 **1989**.

[50] J. F. Scott, “REVIEW Applications of Modern Ferroelectrics”, *Science* 315, 954–959 **2007**.

[51] F. Yen, H. Hsiang, and Y. Chang, “Cubic to tetragonal phase transformation of ultrafine BaTiO3 crystallites at room temperature”, *Japanese Journal of Applied Physics* 34, 6149–6155 **1995**.

[52] B. Begg, E. Vance, and J. Nowotny, “Effect of Particle Size on the Room Temperature Crystal Structure of Barium Titanate”, *Journal of the American Ceramic Society* 77, 3186–3192 **1994**.

[53] M. H. Frey, and D. A. Payne, “Grain-size effect on structure and phase transformations for barium titanate.”, *Physical review. B, Condensed matter* 54, 3158–3168 **1996**.

[54] J. Mangeri, Y. Espinal, A. Jokisaari, S. Pamir Alpay, S. Nakhmanson, and O. Heinonen, “Topological phase transformations and intrinsic size effects in ferroelectric nanoparticles”, *Nanoscale* 9, 1616–1624 **2017**.

[55] A. Grünebohm, M. E. Gruner, and P. Entel, “Domain Structure in the Tetragonal Phase of BaTiO 3 – from Bulk to Nanoparticles”, *Ferroelectrics* 426, 21–30 **2012**.

[56] A. N. Morozovska, and M. D. Glinchuk, “Flexo-chemo effect in nanoferroics as a source of critical size disappearance at size-induced phase transitions”, *Journal of Applied Physics* 119 **2016**.

[57] N. Nuraje, and K. Su, “Perovskite ferroelectric nanomaterials”, *Nanoscale* 5, 8752 **2013**.

[58] W. Y. Shih, W. H. Shih, and I. A. Aksay, “Size dependence of the ferroelectric transition of small BaTiO3 particles: Effect of depolarization”, *Physical Review B* 50, 15575–15585 **1994**.

[59] A. Gruverman, and A. Kholkin, “Nanoscale ferroelectrics: Processing, characterization and future trends”, *Reports on Progress in Physics* 69, 2443–2474 **2006**.

[60] Y. Cui, J. Briscoe, and S. Dunn, “Effect of Ferroelectricity on Solar-Light-Driven Photocatalytic Activity of BaTiO3 - Influence on the Carrier Separation and Stern Layer Formation”, *Chemistry of Materials* 25, 4215–4223 **2013**.

[61] A. Li, Z. Wang, H. Yin, S. Wang, P. Yan, B. Huang, X. Wang, R. Li, Z. Zong, H. Han, and C. Li, “Understanding the anatase–rutile phase junction in charge separation and transfer in a TiO2 electrode for photoelectrochemical water splitting”, *Chemical Science* 7, 6076–6082 **2016**.

[62] A. Koleżyński, and K. Tkacz-Śmiech, “From the Molecular Picture to the Band Structure of Cubic and Tetragonal Barium Titanate”, *Ferroelectrics* 314, 123–134 **2005**.

[63] Y. Inoue, I. Yoshioka, and K. Sato, “Polarization effects upon adsorptive and catalytic properties. 1. CO oxidation over Pd deposited on LiNbO3 ferroelectrics”, *J. Phys. Chem.* 209, 1148–1151 **1984**.

[64] Y. Inoue, K. Sato, and H. Miyama, “A device type photocatalyst using oppositely polarized ferroelectric substrates”, *Chemical physics letters* 129, 79–81 **1986**.

[65] Y. Inoue, J. Matsuo, and K. Sato, “Polarization effects of poled ferroelectric substrates upon surface conductivity changes in phthalocyanine and SnO2 films following gas adsorption”, *J. Chem. Soc., Faraday Trans.* 86, 2611–2615 **1990**.

[66] J. Giocondi, and G. S. Rohrer, “Spatially Selective Photochemical Reduction of Silver on the Surface of Ferroelectric Barium Titanate”, *Chemistry of Materials* 13, 241–242 **2001**.

[67] J. Giocondi, and G. S. Rohrer, “Spatial separation of photochemical oxidation and reduction reactions on the surface of ferroelectric BaTiO3”, *The Journal of Physical Chemistry B* 105, 2–4 **2001**.

[68] S. V. Kalinin, D. A. Bonnell, T. Alvarez, X. Lei, Z. Hu, J. H. Ferris, Q. Zhang, and S. Dunn, “Atomic Polarization and Local Reactivity on Ferroelectric Surfaces: A New Route toward Complex Nanostructures”, *Nano Letters* 2, 589–593 **2002**.

[69] P. M. Jones, D. E. Gallardo, and S. Dunn, “Photochemical Investigation of a Polarizable Semiconductor, Lead-Zirconate-Titanate”, *Chemistry of Materials* 20, 5901–5906 **2008**.

[70] P. M. Jones, and S. Dunn, “Interaction of Stern layer and domain structure on photochemistry of lead-zirconate-titanate”, *Journal of Physics D: Applied Physics* 42, 065408 **2009**.

[71] S. Dunn, P. M. Jones, and D. E. Gallardo, “Photochemical growth of silver nanoparticles on c(-) and c(+) domains on lead zirconate titanate thin films.”, *Journal of the American Chemical Society* 129, 8724–8728 **2007**.

[72] D. Tiwari, S. Dunn, and Q. Zhang, “Impact of Zr/Ti ratio in the PZT on the photoreduction of silver nanoparticles”, *Materials Research Bulletin* 44, 1219–1224 **2009**.

[73] X. Liu, K. Kitamura, K. Terabe, H. Hatano, and N. Ohashi, “Photocatalytic nanoparticle deposition on LiNbO3 nanodomain patterns via photovoltaic effect”, *Applied Physics Letters* 91, 044101 **2007**.

[74] Y. Sun, and R. J. Nemanich, “Photoinduced Ag deposition on periodically poled lithium niobate: Wavelength and polarization screening dependence”, *Journal of Applied Physics* 109 **2011**.

[75] A. M. Schultz, Y. Zhang, P. A. Salvador, and G. S. Rohrer, “Effect of crystal and domain orientation on the visible-light photochemical reduction of Ag on BiFeO3”, *ACS Applied Materials and Interfaces* 3, 1562–1567 **2011**.

[76] R. Nasby, and R. Quinn, “Photoassisted electrolysis of water using a BaTiO 3 electrode”, *Materials Research Bulletin* 11, 985–992 **1976**.

[77] W. Ji, K. Yao, Y.-F. Lim, Y. C. Liang, and A. Suwardi, “Epitaxial ferroelectric BiFeO3 thin films for unassisted photocatalytic water splitting”, *Applied Physics Letters* 103, 062901 **2013**.

[78] N. Rong, M. Chu, Y. Tang, C. Zhang, X. Cui, H. He, Y. Zhang, and P. Xiao, “Improved photoelectrocatalytic properties of Ti-doped BiFeO3 films for water oxidation”, *Journal of Materials Science* 51, 5712–5723 **2016**.

[79] J. Song, T. L. Kim, J. Lee, S. Y. Cho, J. Cha, S. Y. Jeong, H. An, W. S. Kim, Y.-S. Jung, J. Park, G. Y. Jung, D.-Y. Kim, J. Y. Jo, S. D. Bu, H. W. Jang, and S. Lee, “Domain-engineered BiFeO3 thin-film photoanodes for highly enhanced ferroelectric solar water splitting”, *Nano Research* 11, 642–655 **2017**.

[80] F. Gao, X. Y. Chen, K. B. Yin, S. Dong, Z. F. Ren, F. Yuan, T. Yu, Z. G. Zou, and J.-M. Liu, “Visible-Light Photocatalytic Properties of Weak Magnetic BiFeO3 Nanoparticles”, *Advanced Materials* 19, 2889–2892 **2007**.

[81] U. A. Joshi, J. S. Jang, P. H. Borse, and J. S. Lee, “Microwave synthesis of single-crystalline perovskite BiFeO3 nanocubes for photoelectrode and photocatalytic applications”, *Applied Physics Letters* 92, 242106 **2008**.

[82] Y. Inoue, M. Okamura, and K. Sato, “A thin-film semiconducting titanium dioxide combined with ferroelectrics for photoassisted water decomposition”, *The Journal of Physical Chemistry* 89, 5184–5187 **1985**.

[83] N. V. Burbure, P. A. Salvador, and G. S. Rohrer, “Photochemical Reactivity of Titania Films on BaTiO 3 Substrates: Origin of Spatial Selectivity”, *Chemistry of Materials* 22, 5831–5837 **2010**.

[84] N. V. Burbure, P. A. Salvador, and G. S. Rohrer, “Influence of Dipolar Fields on the Photochemical Reactivity of Thin Titania Films on BaTiO3 Substrates”, *Journal of the American Ceramic Society* 89, 2943–2945 **2006**.

[85] W. Yang, Y. Yu, M. B. Starr, X. Yin, Z. Li, A. Kvit, S. Wang, P. Zhao, and X. Wang, “Ferroelectric Polarization-Enhanced Photoelectrochemical Water Splitting in TiO 2 –BaTiO 3 Core–Shell Nanowire Photoanodes ”, *Nano Letters* 15, 7574–7580 **2015**.

[86] L. Li, G. S. Rohrer, and P. A. Salvador, “Heterostructured Ceramic Powders for Photocatalytic Hydrogen Production: Nanostructured TiO2 Shells Surrounding Microcrystalline (Ba,Sr)TiO3 Cores”, *Journal of the American Ceramic Society* 95, edited by E. Dickey, 1414–1420 **2012**.

[87] Q. Li, R. Li, L. Zong, J. He, X. Wang, and J. Yang, “Photoelectrochemical and photocatalytic properties of Ag-loaded BaTiO3/TiO2heterostructure nanotube arrays”, *International Journal of Hydrogen Energy* 38, 12977–12983 **2013**.

[88] Y. Inoue, K. Sato, and S. Suzuki, “Polarization Effects upon Adsorptive and Catalytic Properties. 2. Surface Electrical Conductivity of NiO Deposited on LiNbO3, and Its Changes upon Gas Adsorption”, *J. Phys. Chem.* 89, 2827–2831 **1985**.

[89] L. Li, Y. Zhang, A. M. Schultz, X. Liu, P. A. Salvador, and G. S. Rohrer, “Visible light photochemical activity of heterostructured PbTiO3–TiO2 core–shell particles”, *Catalysis Science & Technology* 2, 1945 **2012**.

[90] Y. Zhang, A. M. Schultz, P. a. Salvador, and G. S. Rohrer, “Spatially selective visible light photocatalytic activity of TiO2/BiFeO3 heterostructures”, *Journal of Materials Chemistry* 21, 4168 **2011**.

[91] S. Li, Y. H. Lin, B. P. Zhang, J. F. Li, and C. W. Nan, “BiFeO3 / TiO2 core-shell structured nanocomposites as visible-active photocatalysts and their optical response mechanism”, *Journal of Applied Physics* 105 **2009**.

[92] Y. Cui, J. Briscoe, Y. Wang, N. V. Tarakina, and S. Dunn, “Enhanced Photocatalytic Activity of Heterostructured Ferroelectric BaTiO3/α-Fe2O3 and the Significance of Interface Morphology Control”, *ACS Applied Materials & Interfaces* 9, 24518–24526 **2017**.

[93] Y. Yuan, T. J. Reece, P. Sharma, S. Poddar, S. Ducharme, A. Gruverman, Y. Yang, and J. Huang, “Efficiency enhancement in organic solar cells with ferroelectric polymers.”, *Nature Materials* 10, 296–302 **2011**.

[94] M. Qin, K. Yao, and Y. C. Liang, “High efficient photovoltaics in nanoscaled ferroelectric thin films”, *Applied Physics Letters* 93, 1–4 **2008**.

[95] V. M. Fridkin, "Bulk photovoltaic effect in noncentrosymmetric crystals", *Crystallography Reports* 46, 654–658 **2001**.

[96] K. T. Butler, J. M. Frost, and A. Walsh, "Ferroelectric materials for solar energy conversion: photoferroics revisited", *Energy Environ. Sci.* 8, 838–848 **2015**.

[97] J. E. Spanier, V. M. Fridkin, A. M. Rappe, A. R. Akbashev, A. Polemi, Y. Qi, S. M. Young, Z. Gu, C. J. Hawley, D. Imbrenda, G. Xiao, and C. L. Johnson, "Power conversion efficiency exceeding the Shockley-Queisser limit in a ferroelectric insulator", *Nature Photonics* 10, under review **2016**.

[98] S. Y. Yang, J. Seidel, S. J. Byrnes, P. Shafer, C.-H. C.-H. Yang, M. D. Rossell, P. Yu, Y.-H. Y.-H. Chu, J. F. Scott, J. W. Ager, L. W. Martin, and R. Ramesh, "Above-bandgap voltages from ferroelectric photovoltaic devices.", *Nature nanotechnology* 5, 143–7 **2010**.

[99] K. Asadi, P. de Bruyn, P. W. M. Blom, and D. M. de Leeuw, "Origin of the efficiency enhancement in ferroelectric functionalized organic solar cells", *Applied Physics Letters* 98, 183301 **2011**.

[100] K. S. Nalwa, J. A. Carr, R. C. Mahadevapuram, H. K. Kodali, S. Bose, Y. Chen, J. W. Petrich, B. Ganapathysubramanian, and S. Chaudhary, "Enhanced charge separation in organic photovoltaic films doped with ferroelectric dipoles", *Energy & Environmental Science* 5, 7042 **2012**.

[101] S. Liu, F. Zheng, N. Z. Koocher, H. Takenaka, F. Wang, and A. M. Rappe, "Ferroelectric Domain Wall Induced Band Gap Reduction and Charge Separation in Organometal Halide Perovskites", *The Journal of Physical Chemistry Letters* 6, 693–699 **2015**.

[102] C. Xu, X. X. Wang, Z. Z. L. Z. L. Wang, Y. Zhang, Y. Yang, W. Guo, and Y. Ding, "Nanowire Structured Hybrid Cell for Concurrently Scavenging Solar and Mechanical Energies", *Journal of the American Chemical Society* 131, 5866–5872 **2009**.

[103] C. Xu, and Z. Wang, "Compact hybrid cell based on a convoluted nanowire structure for harvesting solar and mechanical energy", *Advanced Materials* 23, 873–877 **2011**.

[104] Y. Yang, H. Zhang, G. Zhu, S. Lee, Z.-H. Lin, and Z. L. Wang, "Flexible hybrid energy cell for simultaneously harvesting thermal, mechanical, and solar energies.", *ACS nano* 7, 785–790 **2013**.

Chapter 3

Materials and methods

> *"Nothing in life is to be feared, it is only to be understood. Now is the time to understand more, so that we may fear less."*
>
> MARIE SKŁODOWSKA-CURIE

This chapter outlines the materials used throughout this thesis, as well as the main experimental and characterisation techniques employed.

3.1 Materials

3.1.1 Barium titanate

Barium titanate ($BaTiO_3$) was investigated in the form of bulk single crystals, nanopowders and thick films on fluorine-doped tin oxide (FTO) glass. Substrate grade single crystal slides of $BaTiO_3$ in (100) and (111) orientation were supplied by MTI Corporation. Other than where explicitly stated, the (100) oriented crystal was used for measurements. The slides were stored under ambient conditions and measured as received. Polycrystalline $BaTiO_3$ powders (99.9%) of diameters stated as 50 and 500 nm were supplied by US Nanoresearch Materials Inc. The powders were stored under ambient conditions and used as provided. Thick ($\sim$ 4 µm) films of $BaTiO_3$ nanopowders deposited on FTO coated glass were supplied by Jongin Hong of the Noncentrosymmetric Materials Bank (NCS Bank), South Korea. Nanoparticles were synthesised using a solvothermal process based on a method described elsewhere, and made into a paste using a paste-blending method.[1] The paste was screen-printed onto FTO coated glass and calcined at 550 ℃ for 1 hr. Films were stored in ambient conditions and used as received.

3.1.2 MOx

TiO_2

Titanium dioxide (TiO_2), strontium titanate ($SrTiO_3$) and hematite (iron oxide, α-Fe_2O_3) were used as comparison materials throughout this thesis. Substrate grade bulk single crystals of TiO_2 (rutile) and $SrTiO_3$ were by supplied by MTI Corporation, stored under ambient conditions and used as received. Nanopowders of TiO_2 (diameter 100 and 500 nm) were supplied by US Nanoresearch Materials Inc. Powders were stored under ambient conditions and used as received.

A mesoporous TiO_2 film was prepared by Dr Xiaoe Li using a method described elsewhere.[2] Briefly, a colloidal paste of anatase nanoparticles (10 nm to 15 nm) was synthesised from the aqueous hydrolysis of titanium isopropoxide. Pastes were stirred overnight to ensure homogeneity, before being deposited onto glass microscope slides by the doctor blade method. The 4 µm thick films were then allowed to air dry for 30 min before calcination at 450 °C.

α-Fe_2O_3

Nanostructured Si-doped α-Fe_2O_3 films were supplied by Michael Grätzel's research group (École Polytechnique Fédérale de Lausanne) using a method described elsewhere.[3] These samples were used for variable temperature TAS measurements in Chapter 5. Briefly, Precursor solutions of $Fe(CO)_5$ and tetraethoxysilane were each bubbled with Ar gas and then mixed with air and directed vertically onto the glass substrated heated to 450 ℃. The concentration of Si is $\sim$ 1.5 %. Thin (12 and 50 nm) films of α-Fe_2O_3 deposited on $BaTiO_3$ and TiO_2 single crystal substrates were supplied by Ludmilla Steier and investigated in Chapter 7. The films were deposited by ultrasonic spray pyrolysis using a method reported previously.[4] Briefly, 1 mL of a $Fe(acac)_3$ solution (10 mM $Fe(acac)_3$ (99.9 %, Sigma Aldrich) in ethanol) was sprayed every 30 s at a rate of 12 mL/ min on the substrates which were held at 450 ℃. The growth rate was measured with an F20 interferometer (Filmetrics) on Si substrate and was determined to be 1.1–1.3 nm mL^{-1}.

3.1.3 Sample notation

To distinguish between the different samples in the following chapters, abbreviations are shown in Table 3.1 below.

Table 3.1: List of samples used in this thesis with their assigned abbreviation/label.

Material	Sample	Description
$BaTiO_3$	SC-BTO	Bulk single crystal
	BTO500	Nanopowder, diameter ~500 nm
	BTO50	Nanopowder, diameter ~50 nm
	tTF-BTO	4 µm tetragonal thick film
	cTF-BTO	4 µm cubic thick film
TiO_2	SC-TiO_2	Bulk single crystal
	$TiO_2$500	Nanopowder, diameter ~500 nm
	$TiO_2$100	Nanopowder, diameter ~100 nm
$SrTiO_3$	SC-STO	Bulk single crystal

3.2 Materials Characterisation

3.2.1 XRD, NMR and SEM

Phase composition of $BaTiO_3$ powder photocatalysts were analysed by X-ray diffraction (XRD) (X'Pert PRO, PANalytical Inc.) with a Cu K–α (1.5406 Å) radiation source by Dr Rory Wilson at Queen Mary University of London. To further investigate the phase compositions of $BaTiO_3$ powders, solid state ^{137}Ba MAS NMR was performed by Dr Harold Toms at Queen Mary University of London using a Bruker AV600 NMR spectrometer with a 7 mm probe and a rotary speed of 7 kHz. Morphologies of $BaTiO_3$ and TiO_2 powder photocatalysts were analysed by Dr Ludmilla Steier using a scanning electron microscope (SEM) (Zeiss LEO Gemini 1525) equipped with an in-lens secondary electron detector.

3.2.2 P-E hysteresis

Ferroelectric materials must, by definition, exhibit characteristic hysteresis in polarisation vs electric field (P–E) measurements, shown schematically in Figure 3.1(a). These 'loops' are obtained by applying a triangular voltage waveform (Figure 3.1(b)) and measuring the current across, for example, a ferroelectric crystal. As the applied voltage is increased (positively) the dipoles within the ferroelectric will align with the electric field, leading to a macroscopic (positive) saturated polarisation, P_s (position 1 in Figure 3.1(a)). At this point, the crystal can be considered to have a single ferroelectric domain. Decreasing the voltage results in some dipole reorienting and the polarisation decreases. At zero applied voltage (position 2), ferroelectrics can sustain a remnant polarisation, P_r, unlike standard dielectrics. At a critical applied electric field, E_c, the proportion of opposing domains is exactly equal and thus zero net polarisation is measured (position 3). A larger (negative) applied voltage again leads to a saturated (negative) polarisation (position 4). Sweeping the voltage back to zero completes the hysteresis loop.

Measurement of the P–E loop is conducted using a Sawyer–Tower circuit, demonstrated schematically in Figure 3.1(c). Polarisation, P, is defined as $P = Q/A$, where Q = charge developed on the plates of a capacitor (e.g. a ferroelectric) and A = area of the plates, and has SI units of $\mathrm{C\,m^{-2}}$ (more commonly expressed as $\mathrm{\mu C\,cm^{-2}}$). The charge on a ferroelectric can therefore be measured by connecting it in series with a reference capacitor (of known capacitance which is much greater than the capacitance of the ferroelectric) and cycling the voltage using a signal generator. The direction of the voltage is reversed at high frequency, and the voltage across the capacitor is measured. Since $Q = CV$, and the capacitance of the ferroelectric and reference must be equal when connected in series, the charge on the ferroelectric can be measured. This method of cycling voltage (and thus polarisation) can be used to deduce absolute value of P, which cannot be measured instantaneously.

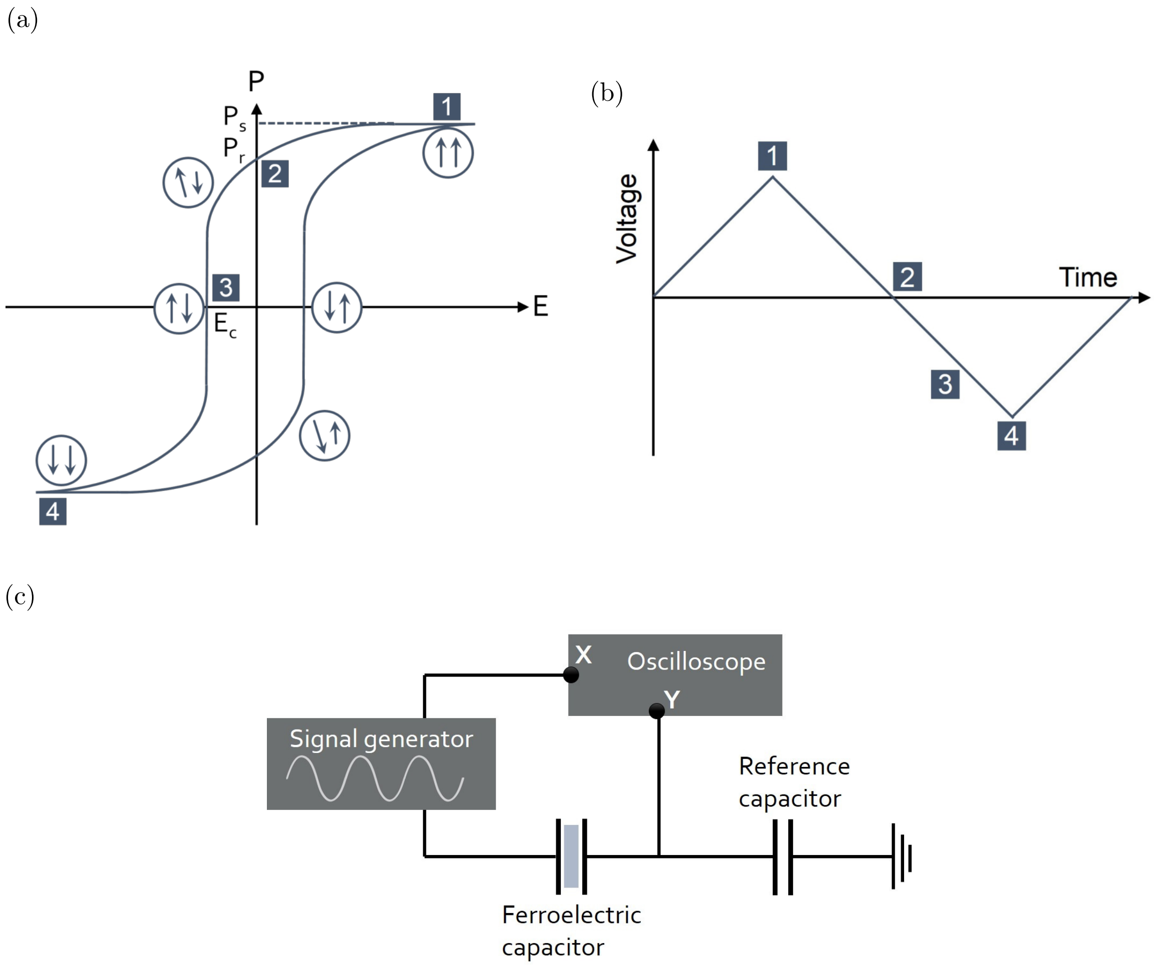

Figure 3.1: (a) The shape of a typical polarisation-electric field loop of a ferroelectric and (b) the corresponding triangular waveform of applied voltage which induces the change in polarisation. (c) Simplified schematic diagram of a Sawyer-Tower circuit for measurement of the polarisation-electric field dependence of a ferroelectric.

3.2.3 Steady-state optical absorption (UV–vis)

Transmission was measured with a UV–vis spectrometer (Perkin-Elmer Lamda-25). Measurement of diffuse-reflectance of powders and nanostructured films was made possible using an attached integrating sphere (Shimadzu). To enable understanding of transient absorption spectroscopy (covered in Section 3.3.1), a brief discussion of how light interacts with matter is outlined here.

The extent to which a beam of light propagating though a material is reduced in intensity is determined by three processes:

1. *Absorption* in which specific frequencies cause an electronic transition to an excited state, transforming the radiant energy into another form (e.g. heat)

2. *Reflection* (diffuse or specular)

3. *Scattering*, where a unidirectional beam is deflected in many directions.

Light which does not undergo any of these processes is transmitted through the material.

While the absorption of light by a material cannot be directly measured, it can be calculated by measuring the transmission ($T = I_{tr}/I_i$), where I_{tr} is the transmitted light and I_i is the incident light, and reflectance ($R = I_r/I_i$), where I_r is the reflected light, of light upon a material and employing the Beer-Lambert law:

$$I_{tr} = I_i e^{-\alpha l} \tag{3.1}$$

where α is the absorption coefficient (the reciprocal of which gives the penetration depth) and l is the thickness of the sample. The optical density, OD (also termed absorbance[*]), at a given wavelength, λ, is defined as the logarithm of the ratio between the intensity of the incident to transmitted light:

$$OD(\lambda) = -\log \frac{I_{tr}(\lambda)}{I_i(\lambda)} \tag{3.2}$$

Notably, the Beer–Lambert Law was formed empirically, and thus has limitations; Equation 3.1 does not account for reflection or scattering. For samples in which these interactions are significant, absorption, A, can be calculated by measuring the reflectance (diffuse and/or specular) relative to a reference sample and using the relation:

$$A = 1 - T - R \tag{3.3}$$

3.3 Methods

3.3.1 Transient absorption spectroscopy (TAS)

Transient absorption spectroscopy is a pump–probe technique in which short-lived (transient) species, i.e. photogenerated charge carriers, are monitored by their optical absorption. Put simply, the equilibrium of a system is perturbed by a very short (fs–ns) flash of light and the time required for the system to return to equilibrium is measured. A typical TAS setup operating in the µs–s timescale is shown in Figure 3.2 demonstrating both transmission and reflectance modes of acquisition. In both modes, a semiconducting sample is irradiated with a short, relatively intense pulse of light (the 'excitation' or 'pump' beam), usually of super-bandgap energy, exciting electrons to the conduction band. The transient states (e.g. photogenerated electrons and holes) can, themselves, absorb light of specific wavelengths, and thus will modulate the transmission of a second, less intense 'probe' beam (typically a tungsten or xenon lamp). The transmission/reflectance of this probe beam is monitored by a photodiode detector linked via an oscilloscope and/or data acquisition (DAQ) card to a computer. The measured change in absorption (ΔOD or $\%A$ in transmission or reflectance modes, respectively) between excited and ground states facilitates kinetic analysis of charge

---

[*] Strictly speaking, these two terms are subtly different. OD is the degree of attenuation which occurs when light propagates through a medium, which can be caused by absorption and/or scattering of light, and is mathematically described as Equation 3.1. *Absorbance* is concerned only with the amount of absorption of light by a material. For instances in which scattering is negligible these two terms are interchangeable. Throughout this thesis, where TAS measurements are conducted in transmission mode, optical density and absorbance are considered mathematically equivalent. ΔOD is used in these cases, whilst $\%A$ is used for data collected in reflectance mode.

generation, relaxation, trapping, recombination and reaction of photogenerated charge carriers. The time resolution is limited by the pulse width of the pump and probe beams, with ‘ultrafast’ systems capable of resolutions on the order of 100 fs.

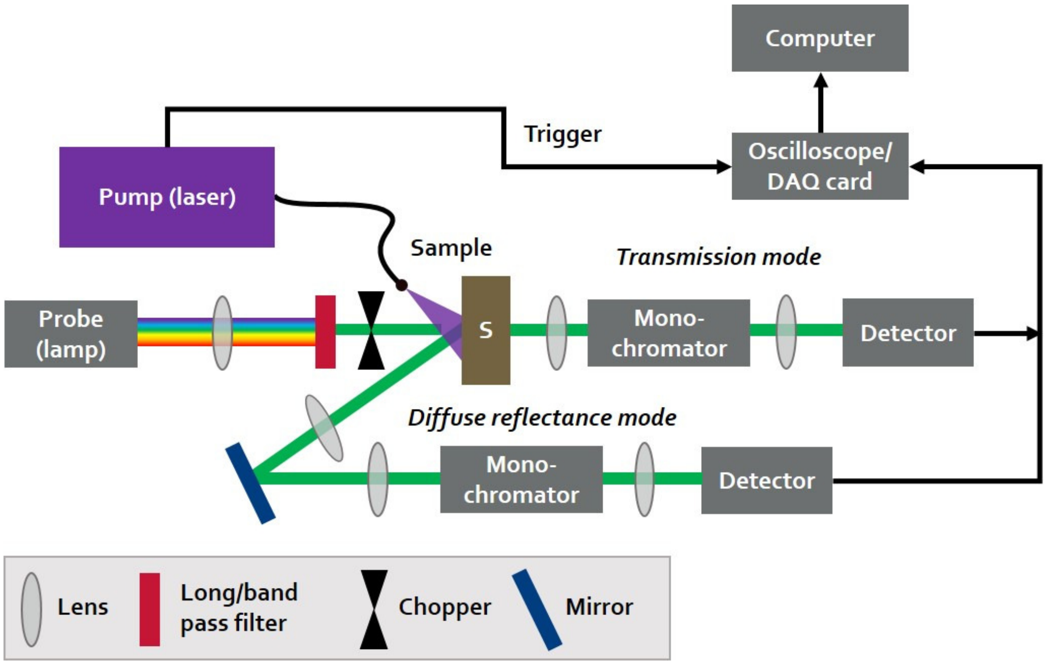

FIGURE 3.2: Schematic representation of a transient absorption spectroscopy setup operating in either transmission or diffuse reflectance measurement modes at µs–s timescales.

Calculating transient absorption

Equation 3.2 can be used to calculate the *change* in absorbance (ΔOD) induced by the excitation pulse as a function of time (t):

$$\begin{aligned}\Delta OD(t) &= OD_1(t) - OD_0 \\ &= \log_{10}\frac{I_i}{I_{tr_1}(t)} - \log_{10}\frac{I_i}{I_{tr_0}} \\ &= \log_{10}\frac{I_{tr_0}}{I_{tr_1}(t)} \end{aligned} \tag{3.4}$$

where OD_0 and I_{tr_0} are the optical density and transmitted intensity before photoexcitation (i.e. in the ground state) and $OD_1(t)$ and $I_{tr_1}(t)$ are the optical density and transmitted intensity at a time, t, after photoexcitation.

In the TAS setup, the change in light intensity at a given λ and t, $\Delta I_{tr}(t,\lambda)$, is detected by a photodiode and is proportional to a change in voltage $\Delta V(t)$. Since Equation 3.2 can be rearranged to give

$$10^{OD(\lambda)} = \frac{I_i(\lambda)}{I_{tr}(\lambda)} \tag{3.5}$$

then

$$\begin{aligned}\Delta OD(t) &= \frac{\Delta I_{tr}(t,\lambda)}{I_0(\lambda)}\\ &= \frac{10^{-OD(t)} - 10^{-OD(0)}}{10^{-OD(0)}}\\ &= 10^{-OD(t)+OD(0)} - 1\\ &= \frac{\Delta V(t)}{V_0} \end{aligned} \tag{3.6}$$

Where V_0 is the voltage detected by the photodiode before photoexcitation. For small values of x, $10^{-x} \approx 1 - x\ln 10$. Since the change in absorption between the ground and excited states will be very small, a Taylor series can be used to approximate Equation 3.6 as

$$\begin{aligned}\frac{\Delta V(t)}{V_0} &= 1 - \Delta OD\ln 10 - 1\\ &= \Delta OD\ln 10 \end{aligned} \tag{3.7}$$

thus

$$\Delta OD = \frac{1}{2.303}\frac{\Delta V(t)}{V_0} \tag{3.8}$$

This linear relationship between the change in voltage and ΔOD is true for small changes in OD.

Lifetimes of excited state species

A useful figure of merit often used to compare rates of recombination between materials is the 'carrier lifetime' — the average time taken for the photogenerated carriers to recombine (radiatively or non-radiatively). If the recombination follows a single exponential decay, such that $\Delta OD(t) \propto e^{-t/\tau}$, the lifetime is defined as τ. In many materials, however, recombination rates follow non-exponential or multi-exponential decays. In these cases, where the mathematical definition may not be known, it is useful to estimate the lifetime as the average time for the TA amplitude (which is proportional to the photogenerated charge carrier population) to reduce by 50%. Throughout this thesis, this latter definition of 'carrier lifetime' is used, and denoted as $t_{50\%}$, for decays which follow non-exponential or multi-exponential decays.

Microsecond TAS setup

The TAS systems used in the studies reported herein to measure charge carrier dynamics on timescales of microseconds to seconds are based on the setup shown schematically in Figure 3.2. The home-built systems consisted of a Nd:YAG laser (Big Sky Laser Technologies, Ultra CRF) as the excitation source with a pulse width of $<$ 10 ns at a range of excitation frequencies. The third harmonic of the Nd:YAG crystal provided excitation at 355 nm while the use of an optical parametric oscillator (Opotek Inc. Tuneable Laser Systems, Opolette

355 II) allowed wavelength tunability from 410–2100 nm. A liquid light guide was used to transmit the excitation beam to the sample. The excitation intensity was controlled either using neutral density (ND) filters (Comar Instruments) or adjusting the delay between the flash lamp and Q switch. A tungsten lamp (Bentham IL, 100 W) was used as the probe source. Wavelength selection was made using long pass filters or a monochromator (OBB-2001, Photon Technology International) in front of the sample. A monochromator placed after the sample was used to minimise laser scatter or emission reaching the photodiode. A silicon photodiode (Hamatsu S3071) detected the change in transmission of the monochromatic probe beam. The signal output of this photodiode was electronically amplified (Costronics) and data collected and recorded using an oscilloscope (Tektronics TDS 2012c) for µs–ms timescales and a data acquisition (DAQ) card (National Instruments, NI USB-6211) for ms–s timescales. All data were processed using homebuilt software based on LabVIEW. TA decays are displayed in ΔOD for those obtained in transmission mode, or $\%A$ if obtained in diffuse-reflectance mode.

Femtosecond TAS setup

Ultrafast (fs–ns) transient absorption data was collected using a commercially available system, shown schematically in Figure 3.3. This setup is comprised of a regeneratively amplified Ti:sapphire system (Solstice, Spectra-Physics) and broadband pump-probe transient absorption spectrometer (HELIOS, Ultrafast Systems). The output of the Solstice (92 fs at 800 nm, 1 kHz repetition rate) is used to generate both the pump pulse and probe beam. A fraction of the 800 nm beam is routed, using Ag/Al mirrors, to a transient optical parametric amplifier (TOPAS Prime, Spectra-Physics) to generate the pump pulse. A frequency mixer (NirUVis, Light Conversion) is used to select the final pump wavelength, the intensity of which was modulated using neutral density filters. A further fraction of the 800 nm beam is routed to the HELIOS spectrometer via a motorised translational stage (7 ns), which facilitates the delay of the probe with respect to the pump pulse. The white light continuum (WLC) is generated using a Ti:sapphire crystal. A reference spectrometer monitors a fraction of the WLC, allowing for noise reduction in the signal, whilst the remainder passes through the sample and to the signal detector. Spectra mapping was achieved using a synchronised chopper (500 Hz) to block alternate pulses to obtain the difference in absorption between excited and unexcited samples. The final difference spectra were an average of a number of scans (chosen according to the quality of the signal, typically 4–8). Due to the group velocity dispersion, or ‘chirp,’ of white light, the temporal overlap between pump and probe (i.e. time zero, t_0) is wavelength-dependent, and thus needs to be corrected post-measurement. This was done using Surface Xplorer software (Ultrafast Systems), so that t_0 occurs at the half-amplitude of the spectrum rise.

Variable-temperature TAS

To investigate the effect of temperature on charge carrier dynamics, TAS measurements were conducted with the sample at elevated temperatures using a self-designed and homebuilt heating device shown schematically in Figure 3.4. The sample was placed in a sealed quartz cuvette which was inserted into the cavity of an aluminium (Al) casing insulated with 6 mm of calcium silicate (Duratec 750). Two windows through the Al block and insulating layer allowed transmission or reflectance of the probe beam incident on the sample. The temperature was controlled using two resistive heaters (50 W, RS Components 7241781) and a K-type thermocouple in the Al casing which were linked to a proportional-integral-derivative

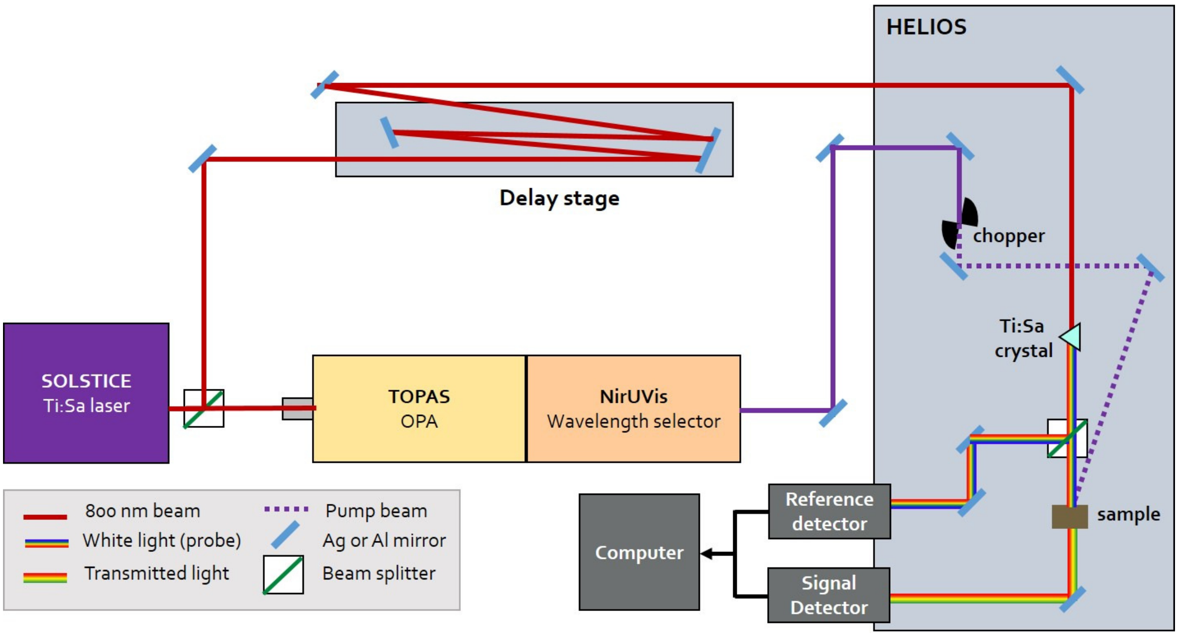

FIGURE 3.3: Schematic representation of the system used to collect ultrafast (fs-ns) transient absorption data.

(PID) controller. Samples were left to equilibrate for 20 minutes after each temperature change before TA measurements were performed to ensure uniform temperature across the sample.

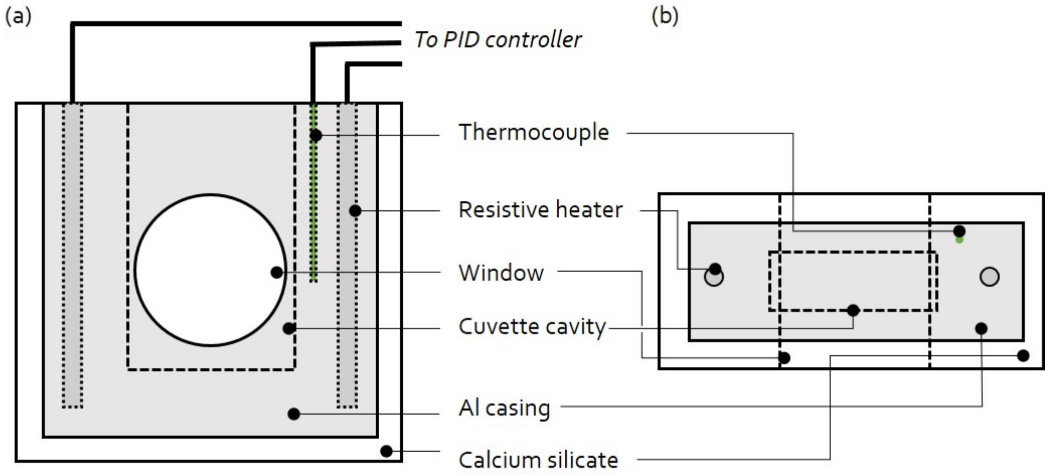

FIGURE 3.4: Schematic diagram of (a) front view and (b) top view of the heating device used to vary the temperature of the TAS samples between 25 and 152 °C.

3.3.2 Photoinduced absorption spectroscopy (PIAS)

A simple modification of the TAS setup allows tracking of the change in absorption during and after continuous illumination of a sample. This enables monitoring of charge carrier dynamics under steady-state conditions comparable to working conditions (e.g. water splitting or dye degradation conditions) and is therefore a powerful tool for investigating the accumulation and reaction of excited state species on long (tens of seconds). This technique is herein referred to as photoinduced absorption spectroscopy (PIAS).

Typically, a PIAS signal at a given probe wavelength will follow an evolution as described in Figure 3.5. When the LED light is switched on (t_{on}), photoinduced species (e.g. holes or electrons) are generated and accumulate at the surface of the material, leading to increased absorption of the probe beam and thus the observed rise in the optical signal. Once these species are generated they will either undergo recombination (with each other or with trap/defect states within the material) or react with the redox electrolyte, both processes being described as 'consumption' here. If an equilibrium between generation and consumption is reached the signal will arrive at a steady state at t_{ss}. At t_{off}, the illumination source, and thus the generation of photoinduced species, is interrupted and the signal decays as the monitored species are consumed. The amplitude at t_{ss} can be considered a measure of the population of the photogenerated species under steady state conditions using a given photon flux.

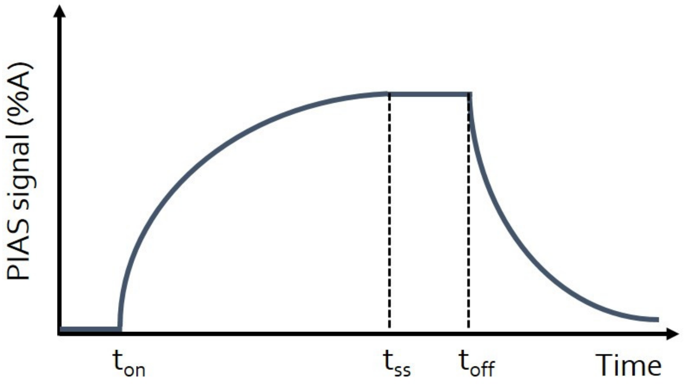

FIGURE 3.5: Typical evolution of a photo-induced absorption signal obtained after illumination between t_{on} and t_{off}. The signal reaches a steady state at t_{ss}, and decays after illuminate is halted.

PIAS setup

The probe setup is identical to the microsecond TAS setup (described earlier, Figure 3.2), but the entire optical signal recording is performed by the DAQ card. The fundamental difference between TAS and PIAS is the length of the excitation pulse, which, instead of a short-pulsed laser beam is a continuous wave beam. In this case the pump is a UV (365 nm) light-emitting diode (LED) (LZ1-10U600, LedEngin Inc.) which can deliver a photon flux of 1–40 $\mathrm{mW\,cm^{-2}}$, measured by a Si photodiode (FDS100-CAL, Thorlabs). The photon flux was regulated by altering the current passing through the LED between 0.05 and 0.6 A. A function generator (TG300, Thurlby Thandar Instruments) was used to control the long light pulses by delivering a square wave, of a set frequency and symmetry to a MOSFET (STF8NM50N, STMicroelectronics), which was used to turn the LED power supply (QL564P, Thurlby Thandar Instruments) on and off. The function generator also triggered the DAQ card used to record the optical signal. Data reported in this thesis corresponds to the average of 1-3 LED pulses.

All PIAS data reported herein were collected in reflectance mode. $BaTiO_3$ nanoparticles were affixed to glass microscope slides using an epoxy resin and submerged in a redox electrolyte (water or a chemical electron scavenger).

3.3.3 Photocatalytic activity measurements

Photocatalytic dye decolourisation

Rhodamine B (RhB) solutions (10 ppm) were prepared by dissolving RhB (analytical standard, Sigma-Aldrich) in deionised water. Photocatalytic decolourisation rates were investigated by loading 0.15 g $BaTiO_3$ powder into 50 mL of dye solution. The mixture was stirred in the dark for 30 minutes to obtain adsorption–desorption equilibrium before exposure to 365 nm light by an LED source (LZ1–10U600, LedEngin Inc., 1–40 $\mathrm{mW\,cm^{-2}}$) at a distance of $\sim$ 2 cm. Aliquots of solution 0.5–2 mL were taken for sampling at fixed intervals. Catalyst powders were removed by centrifugation (10,000 rpm, 10 min) to ensure no further reactions occurred. The optical absorption of the obtained dye solutions was measured using a UV–vis spectrometer (Perkin Elmer Lamda-25), using deionised water as a reference.

Photocatalytic water oxidation

$BaTiO_3$ powders (2.5 $\mathrm{g\,L^{-1}}$) were suspended in aqueous $Na_2S_2O_8$ solution (0.1 M) in a vial sealed with a septum and parafilm. A Clark oxygen sensor (Unisense OX-NP) was inserted through the septum into the headspace above the water level, and the mixture stirred in the dark to achieve a stable baseline oxygen level. The mixture was then irradiated with 365 nm LED light (LZ1–10U600, LedEngin Inc., 1–40 $\mathrm{mW\,cm^{-2}}$). Calibration was achieved by injecting known quantities of oxygen into the cell following measurements.

References

[1] H. W. Lee, S. Moon, C. H. Choi, and D. K. Kim, "Synthesis and size control of tetragonal barium titanate nanopowders by facile solvothermal method", *Journal of the American Ceramic Society* 95, 2429–2434 **2012**.

[2] L. Xiao-e, A. N. Green, S. A. Haque, A. Mills, and J. R. Durrant, "Light-driven oxygen scavenging by titania/polymer nanocomposite films", *Journal of Photochemistry and Photobiology A: Chemistry* 162, 253–259 **2004**.

[3] A. Kay, I. Cesar, and M. Grätzel, "New benchmark for water photooxidation by nanostructured alpha-Fe2O3 films.", *Journal of the American Chemical Society* 128, 15714–21 **2006**.

[4] L. Steier, I. Herraiz-Cardona, S. Gimenez, F. Fabregat-Santiago, J. Bisquert, S. D. Tilley, and M. Grätzel, "Understanding the role of underlayers and overlayers in thin film hematite photoanodes", *Advanced Functional Materials* 24, 7681–7688 **2014**.

Chapter 4

Photophysics of $BaTiO_3$

> *"The best that most of us can hope to achieve in physics is simply to misunderstand at a deeper level."*
>
> Wolfgang Pauli

4.1 Introduction

As previously discussed in Chapter 2, metal oxides are considered some of the most promising materials for water oxidation. However, conversion efficiencies of devices using these materials are largely limited by fast recombination, making water splitting unfeasible in the absence of applied bias.[1–4] Designing devices which have an internal bias due to intentially induced energy offsets — e.g. p–n junctions, heterojunctions and redox cascades — have proven successful in enhancing charge separation and device performance in some cases, but generally still require an additional electrical input to drive the reaction.[2–6] The utilisation of the internal electric field present in piezo- and ferro-electric metal oxides is gaining interest, due to the potential for the polarisation-induced band bending in these materials to reduce electron–hole recombination. Despite the growing body of literature, few spectroscopic studies have been done on ferroelectric metal oxides and thus there are still large gaps in the understanding of how the presence of an internal electric field can influence charge carrier dynamics. To determine if ferroelectricity can indeed slow down recombination, the charge carrier dynamics in a ferroelectric material must first be characterised. Gaining an insight into the photophysical processes occurring in these materials following absorption of a photon is essential for understanding how ferroelectrics could lead to the design of more efficient devices.

This chapter describes the photophysical processes occurring in $BaTiO_3$ — an archetypal ferroelectric — upon bandgap excitation, observed by transient absorption spectroscopy on timescales of ps–ns and µs–s. This allows for monitoring of key processes such as geminate and bulk recombination (ps–µs), as well as trapping/detrapping limited recombination (usually µs–s), which are currently not well understood in this material. Early reports of photoinduced absorption in $BaTiO_3$, investigating the role of impurities on a phenomenon known as the photorefractive effect, used sub-bandgap pump energies to directly excite trap states, showing recombination of trap states is important on timescales spanning ps to ms.[7, 8] These studies, however, neglected to investigate the impact of interband transitions and free electrons and holes, which dominate carrier dynamics under 'working' solar energy conversion conditions in metal oxides (i.e. super-bandgap illumination). A later study on the photoinduced absorption of $BaTiO_3$ employed a UV pump beam and visible probe beam, finding that trapping of electrons from the conduction band into mid-bandgap states occurred within a few ms.[9]. Recently, the ultrafast carrier dynamics of a thin film of $BaTiO_3$ were investigated using super-bandgap femtosecond laser excitation.[10] Under high ($2\,\mathrm{mJ\,cm^{-2}}$ to $10\,\mathrm{mJ\,cm^{-2}}$) laser intensities, carriers were found to trap with time constants of $\sim 10\,\mathrm{ps}$. Notably, no measurable photoinduced absorption occurred using a sub-bandgap pump beam, in contrast to earlier studies. This indicates that impurity levels can significantly affect carrier dynamics, and that even defect levels too low to cause photoinduced absorption can dictate carrier dynamics. None of these studies considered the influence of ferroelectricity on the behaviour of excited state species. To the best of my knowledge, the first study on the effect of internal fields on carrier dynamics in ferroelectric $BaTiO_3$ is presented in this thesis.

This chapter lays the foundations for understanding the effect of the internal electric field on charge carrier dynamics in ferroelectric $BaTiO_3$. By characterising the photophysical processes which occur upon absorption of a photon in the presence of an internal field, we can investigate how manipulation — and even removal — of this field will change recombination rates (Chapter 5). Following this, the effect of ferroelectricity on photocatalytic activity can be investigated using ferro- and non-ferro-electric $BaTiO_3$ samples, as is investigated in Chapter 6.

Here, excitation intensity studies indicate that bulk recombination occurs on timescales comparable to previously reported metal oxides, whilst geminate recombination is not detected on these timescales. Hole and electron absorption signatures are identified, using chemical scavengers, to be in the visible and near-IR regions, respectively. Excited state absorption due to photogenerated electrons and holes have not, to my knowledge, been identified in $BaTiO_3$ before. This work is the first reported characterisation of the transient absorption spectrum where spectral signatures of both electrons and holes are identified.

With the exception of scavenger studies, TAS measurements presented in this chapter were conducted on bulk single crystals of $BaTiO_3$, which are known to be ferroelectric. Although charge carrier dynamics in semiconductors are becoming increasingly well-studied and -understood, much is still unclear about the effect of morphology and the role of surface states on recombination pathways and kinetics. On one hand, nanostructuring should aid charge separation by reducing the distance that photogenerated charges must travel to reach the surface of the material; most studies of charge carriers in metal oxides in the literature are conducted on nanostructured materials, since these have generally resulted in highest performances in photoelectrochemical and photocatalytic devices.[2–4, 11] However, it can also introduce surface recombination sites, which have been suggested to cause an increase in recombination in some cases e.g. in metal chalcogenides, where non-radiative decay pathways are mediated by surface-induced energy states.[12, 13] The study of bulk single crystals here acts to simplify the analysis of charge carrier dynamics, as it allows the effect of differences in kinetics due to surface-induced states to be considered negligible.

Throughout this chapter, comparisons are drawn between TA characteristics of $BaTiO_3$, TiO_2 and $SrTiO_3$, which are all n-doped metal oxides. Electronically, $BaTiO_3$ and TiO_2 are similar in that, as well as sharing comparable bandgaps, their conduction and valence bands have been found to lie within ~ 0.2 eV of each other (at approximately -0.5 and $2.7\,\mathrm{V}$ vs NHE, respectively).[14] Whilst the energy levels of the non-ferroelectric material $SrTiO_3$ lie at slightly more reductive potentials,[15] it is isostructural with $BaTiO_3$; both are perovskite-type (ABO_3) with face-centred oxygens (Figure 4.1). Further, both belong to the cubic crystal system (Figure 4.1(b)) when $BaTiO_3$ is above its Curie temperature, i.e. $a = b = c$. At room temperature, the only structural difference lies in the elongation of lattice parameter c due to a shift in central Ti^{4+} in $BaTiO_3$ inducing a switch to the tetragonal crystal system (4.1(a)).

It is this small shift in ionic position which results in ferroelectricity in $BaTiO_3$, but not $SrTiO_3$. Thus, a comparative study between these materials could be useful for revealing the influence of ferroelectricity in tetragonal $BaTiO_3$ on charge carrier dynamics, by minimising variables such as differences in structure and band energies. Characterising the similarities and differences in charge carrier dynamics across different metal oxides will help to form a detailed understanding of structure-performance relationships in these materials.

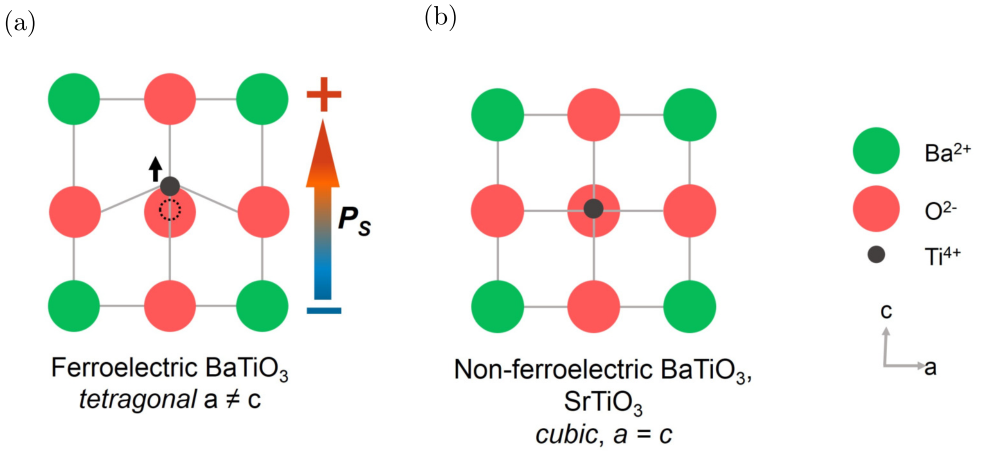

FIGURE 4.1: Unit cell structures of (a) tetragonal, ferroelectric $BaTiO_3$, in which asymmetry induces a spontaneous polarisation, P_S, and (b) cubic $BaTiO_3$ and $SrTiO_3$, which are both fully centrosymmetric and thus non-ferroelectric.

4.2 Experimental

Most results obtained in this chapter were done so using commercially bought substrate grade single crystals of $BaTiO_3$ (SC-BTO), TiO_2 (rutile, SC-TiO_2) and $SrTiO_3$ (SC-STO). For studies with chemical scavengers, ∼ 4 µm thick films of tetragonal $BaTiO_3$ (tTF-BTO) screen-printed onto FTO-glass were used. [*]

Transient absorption measurements were obtained using bandgap excitation at 355 nm for both µs–s and fs–ns timescales. Full details of the instrument set up is given in Chapter 3. On the µs–s timescale, a pulse rate of 0.33 Hz was chosen to allow samples to return to ground state before the next laser pulse. Each measurement was obtained using a monochromatic probe beam, as described in Section 3.3.1, over the range of 450–1000 nm. A probe wavelength range of ∼400–800 nm was used at ultrafast (fs–ns) timescales. Transmission mode TAS was used for all single crystal samples, whilst TA data of tTF-BTO were collected in reflectance mode.

Inert atmospheres were achieved by placing single crystal samples into a sealed quartz cuvette and purging with Ar or N_2. A 1:1 mixture of MeOH and water was used as a hole scavenger. Sodium persulfate ($Na_2S_2O_8$, 0.1 M) was used as an electron scavenger. Both reagents were degassed to remove oxygen prior to measurements.

---

[*] Where observations and discussions related to measurements conducted on these particular samples are made, they are referred to by their sample names (SC-BTO, SC-STO etc.). Where discussion relates to the more general material properties not measured here, chemical formulae are used ($BaTiO_3$, $SrTiO_3$ etc.)

4.3 Results

4.3.1 Steady-state absorption

To understand features of photoinduced absorption, it is important to first understand the steady- (or ground-) state absorption of the investigated samples. UV–vis absorption spectra of SC-BTO, SC-STO and SC-TiO_2 are shown in Figure 4.2, showing typical characteristics of these materials. Absorption onsets are at ~ 415, 400 and 390 nm for SC-TiO_2, SC-BTO and SC-STO, respectively. These correspond to bandgaps of ~ 3.0, 3.1 and 3.2 eV which are within the ranges commonly reported in the literature.[16–18] The shift in baseline at wavelengths longer than the bandgap are likely due to some specular reflectance (all three materials are polished single crystals, and thus levels of diffuse reflectance are expected to be low). The sharp absorption onsets in SC-TiO_2 and SC-STO suggest low levels of defects in the crystals (and therefore few mid-bandgap/tail states to facilitate lower energy absorption). On the other hand, the gradual absorption onset seen in SC-BTO suggests a higher level of defects resulting in the presence of mid-bandgap/tail states. Thus, transitions at energies below the bandgap are seen. For all TAS measurements discussed in this chapter, the excitation wavelength, λ_{ex}, used is 355 nm. This is of a higher energy than the bandgap for all three metal oxides, at which strong absorption is observed. Thus it is assumed that all photons are absorbed.[†]

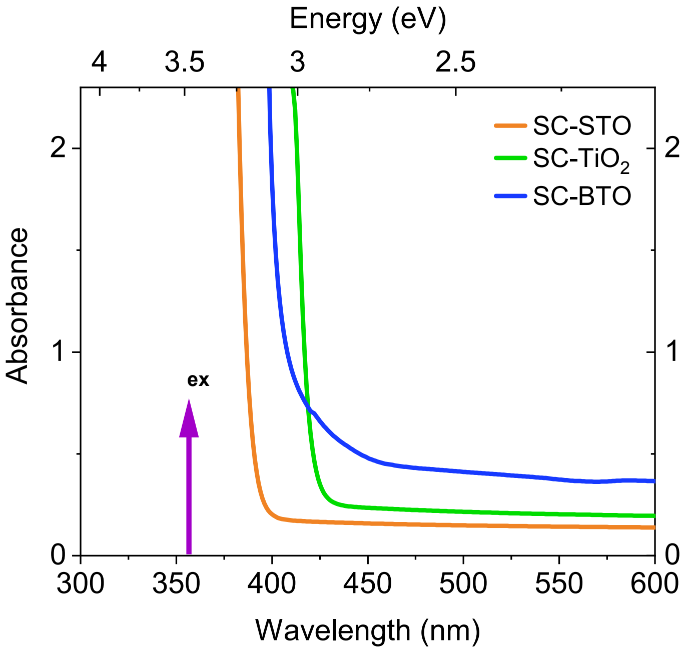

FIGURE 4.2: UV–vis spectra of bulk single crystal metal oxides, $BaTiO_3$ (SC-BTO), TiO_2 (SC-TiO_2) and $SrTiO_3$ (SC-STO). The purple arrow at 355 nm indicates the excitation wavelength used in TAS measurements. No correction has been made for reflection.

[†] No literature value for the absorption coefficient, α, has been found for $BaTiO_3$ at 355 nm. Further, since the transmission of light through the 1 mm thick crystal is so low, α at 355 nm cannot be obtained from the absorption spectrum. Thus, the penetration depth ($1/\alpha$), cannot be calculated for this material.

4.3.2 Charge carrier dynamics on fs–ns timescales

Charge carrier dynamics of $BaTiO_3$ are investigated at ultrafast (fs–ns) timescales, and compared to those of TiO_2 and $SrTiO_3$. On these timescales, it is likely that the dominant recombination pathway will be the bimolecular recombination of photogenerated electrons and holes, as has been reported for α-Fe_2O_3 and TiO_2.[19, 20]

$BaTiO_3$

Figure 4.3 summarises the transient absorption spectrum and corresponding decay kinetics of SC-BTO in the visible range from tens of fs to ∼ 6 ns after after bandgap excitation. The spectrum is characterised by broad positive absorption between 480 and 780 nm, with absorption increasing towards longer wavelengths. TA signals are initially approximately constant, and decay at $t > 300$ ps–ns. Similar decay kinetics are observed for all probe wavelengths studied and fit well to a single exponential decay, such that $\Delta OD = Ae^{t/\tau}$ (dashed black line in Figure 4.3(b)), where A is the initial amplitude and τ, the time constant, is approximately 7.3 ns.

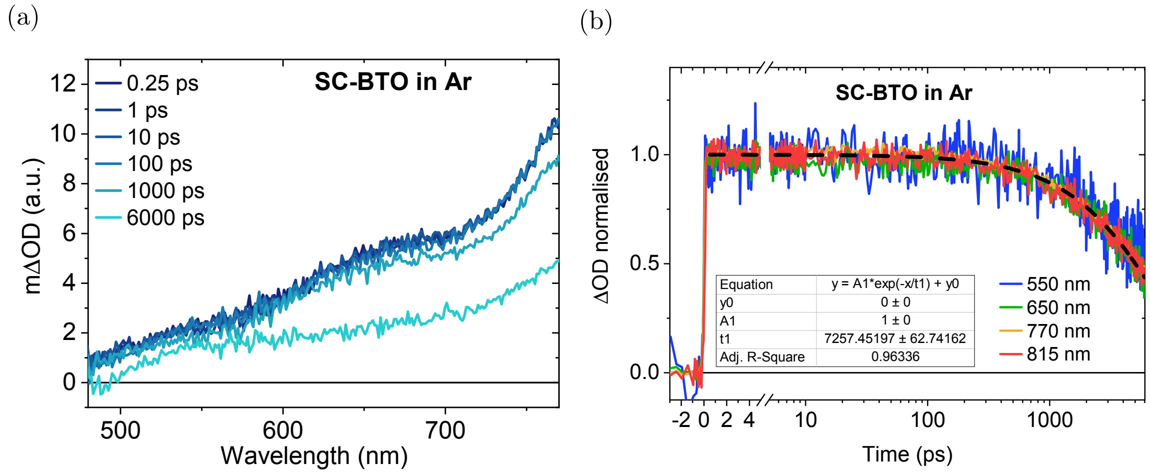

FIGURE 4.3: (a) Time evolution of the TA spectrum and (b) TA decay kinetics normalised at 2 ps of SC-BTO under Ar in the visible region following super-bandgap excitation (355 nm, 0.8 mJ cm^{-2}). The dashed black line is a single exponential decay fit, $\Delta OD = Ae^{t/\tau}$., with $\tau = 7.3$ ns

To investigate the nature of this recombination, TAS measurements were performed at varying excitation intensities. Figure 4.4(a) shows transient absorption decays at a representative probe wavelength (λ_{pr}) of 770 nm as a function of pump intensity from 0.13 to 0.80 mJ cm^{-2}, with normalised decays plotted in Figure 4.3(b). Amplitudes, A, and lifetimes as a function of excitation intensity were extracted from single exponential fits and are graphically shown in Figure 4.4(c) and (d). It is apparent that as the pump intensity increases, the signal amplitude gets larger due to increased charge carrier generation. The lifetime decreases with increasing excitation intensity (12.6 ns at 0.13 mJ cm^{-2}, 7.3 ns at 0.80 mJ cm^{-2}), which is qualitatively typical of bimolecular recombination of separated charges;[21] the larger the number of electrons and holes photogenerated, the higher the likelihood that they will recombine. Signals observed on these timescales are thus assigned to bimolecular recombination of bulk electrons and holes.

Geminate recombination (between a Coulombically bound electron and hole) has previously been suggested to be observed in TiO_2 at these timescales, appearing as an early feature with a short (< 1 ps) lifetime.[20] No such feature is observed here, which is consistent with the extremely high (> 2000 [22–24], cf. ~ 170 for TiO_2 [25]) dielectric constant facilitating fast and efficient separation of electron–hole pairs into free charges. This further supports the assignment of these decays to bimolecular recombination of charge-separated electrons and holes.

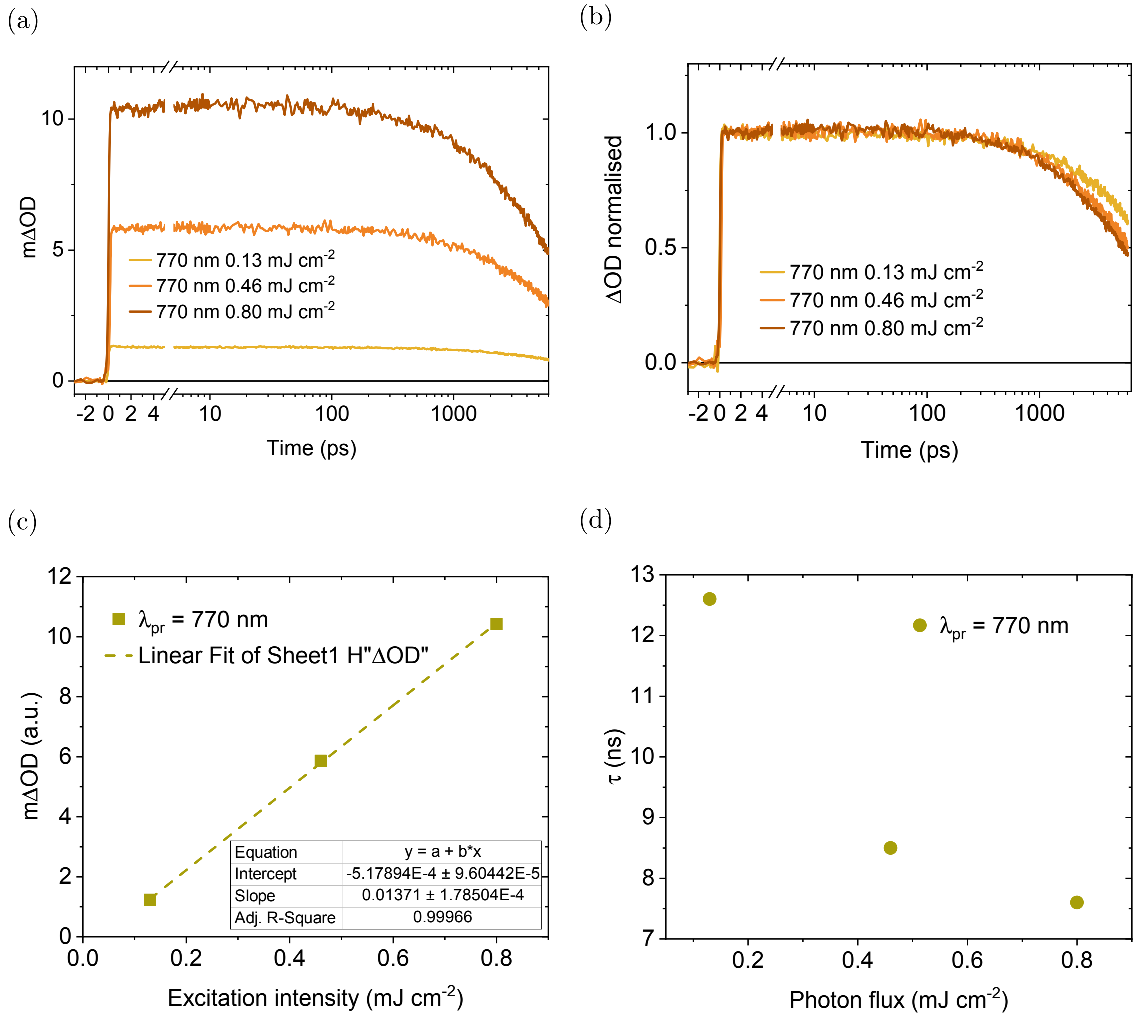

FIGURE 4.4: (a) Transient absorption decays of SC-BTO as a function of excitation intensity ranging from 0.13 to 0.80 mJ cm^{-2} and (inset) normalised at 2 ps. Signal amplitudes (b) and lifetimes (c) as a function of excitation intensity.

TiO_2 and $SrTiO_3$

The TA spectra of SC-TiO_2 and SC-STO are shown in Figure 4.5(a) and (b). Both are very similar to that of SC-BTO (Figure 4.3(a)); broad positive absorption is observed between $\sim$ 450 and 750 nm, increasing towards longer wavelengths. Decay kinetics of the three metal oxides are compared at the maximum ΔOD and comparable excitation intensity in Figure 4.5(c) and (d). Recombination rates in SC-BTO and SC-TiO_2 are almost identical ($t_{50\%} \sim$ 7.3 ns), whilst the lifetime of the species observed in SC-STO is extremely long; the signal has barely started to decay by 6 ns. Signal amplitudes, on the other hand, vary greatly between the three samples for comparable excitation intensities. Since all exhibit strong absorption

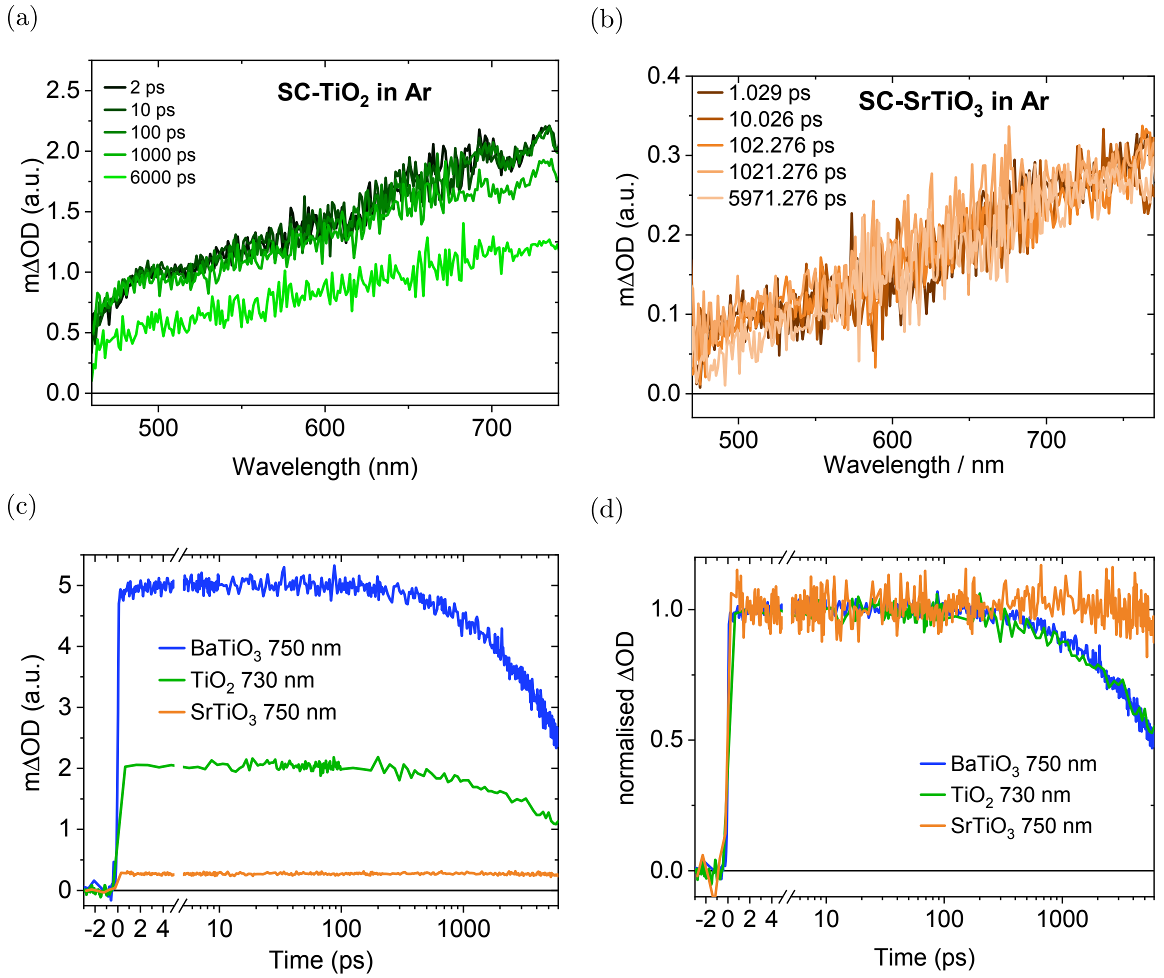

FIGURE 4.5: Time evolution of TA spectra of single crystals of (a) TiO_2 and (b) $SrTiO_3$ following laser excitation (355 nm, ~ 0.4–0.5 $mJ\,cm^{-2}$, 500 Hz). Comparison of unnormalised (c) and normalised (d) decay kinetics at $\lambda_{pr} \sim 730$ nm between single crystal $BaTiO_3$ (blue), TiO_2 (green) and $SrTiO_3$ (orange).

at 355 nm (Figure 4.2), it is assumed that the same number of photons is absorbed by each metal oxide.

4.3.3 Charge carrier dynamics on µs–s timescales

Now presented are charge carrier dynamics of SC-BTO, SC-STO and SC-TiO_2 at longer (µs–s) timescales. According to previous reports, these are the timescales on which water oxidation is expected to occur.[26, 27] It is thus vital to understand the photophysical processes occurring on these timescales in order to improve materials and device design for solar fuels.

$BaTiO_3$

The evolution of the TA spectrum as a function of time elapsed after laser excitation is shown in Figure 4.6(a) for SC-BTO in an inert atmosphere. Corresponding decay kinetics, plotted on a linear–log scale, are shown in Figure 4.6(b), with normalised data in Figure 4.6(c). The spectrum is characterised by long-lived and broad positive absorption over the range 460–950 nm. In contrast to the spectrum obtained from fs to ps, absorption at long timescales is greatest in the blue region, decreasing with increasing wavelength. This difference suggests that different species dominate absorption on the two timescales. Also striking is the dependence of decay dynamics on probe wavelength, particularly evident in the normalised decays in 4.6(c). At shorter wavelengths ($\lambda_{pr} \sim$ 460–600 nm) signals are very long-lived, and of stretched exponential-type decay ($\Delta OD \propto e^{(-(t/\tau)^{\beta})}$, β = stretching component). Shorter lifetimes are observed at longer wavelengths, and decays are approximately linear on a linear-log scale. $t_{50\%}$ values range from ∼1–100 ms at a consistent excitation intensity, depending on probe wavelength. Stretched exponential decays have previously been associated with a distribution of energetic states, resulting in electron–hole recombination deviating from monoexponential to dispersive decay kinetics.[28–30]

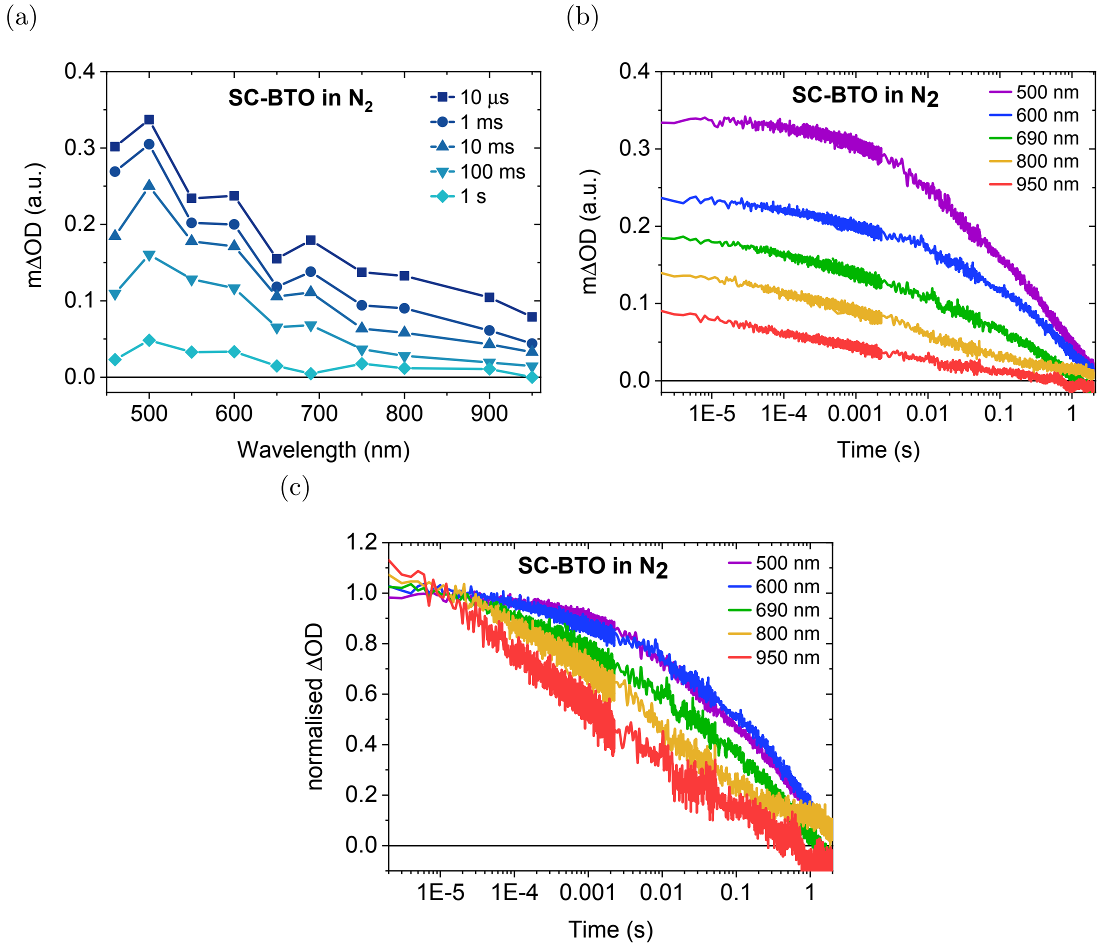
(a) (b) (c)

FIGURE 4.6: (a) Transient absorption spectrum of SC-BTO as a function time after laser excitation (355 nm, laser intensity 200 µJ cm^{-2}). (b) Decay kinetics plotted as a function of probe wavelength and (c) decays normalised at 20 µs.

The intensity dependence at long timescales is summarised in Figure 4.7 for probe wavelengths of 550 and 750 nm. As seen at ultrafast timescales, signal amplitudes scale linearly with pump intensity, due to increased charge generation and thus increased absorption of the probe beam. However, at these timescales, it is apparent that $t_{50\%}$ values are independent of pump intensity. This is typical of pseudo-first order recombination, in which one carrier is in excess.[31] This disparity in behaviour between ultrafast and 'slow' timescales further suggests that different species are being observed, or that a shift in dominant species occurs between the two timescales, discussed further below.

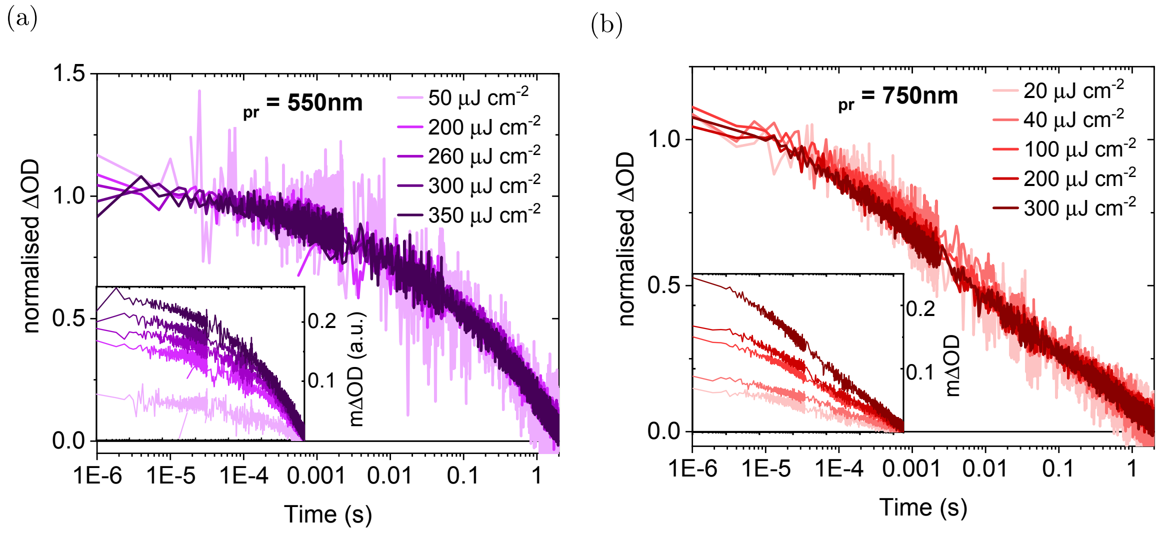

FIGURE 4.7: Normalised (main) and unnormalised (inset) transient absorption decay kinetics of SC-BTO at a probe wavelength of (a) 550 nm and (b) 750 nm as a function of excitation intensity ($\lambda_{ex} = 355$ nm).

$SrTiO_3$ and TiO_2

TA spectra and decay kinetics of SC-STO are shown in Figure 4.8. Similarly to SC-BTO, broad positive absorption is observed in the visible range. Also similar is the difference in absorption maximum between ultrafast and slow timescales; from $\sim$ 100 fs to $\sim$ 6 ns the absorption maximum appears at the red end of the spectrum, whilst from µs onwards, absorption is stronger towards the blue, generally decreasing with increasing wavelength. This indicates that, as with SC-BTO, a different species dominates the absorption at each timescale. Similar decay kinetics are observed at all probe wavelengths. Notably, recombination at these timescales is faster than for SC-BTO by an order of magnitude, with a $t_{50\%}$ value of $\sim$ 20 ms (cf. 100 ms for SC-BTO).

Attempts to obtain transient absorption measurements on SC-TiO_2 were unsuccessful, since no signal was found even at high ($\sim$ 2.5 mJ cm^{-2}) excitation intensities. This lack of signal is consistent with previous reports[32, 33] that TA signals obtained on µs–s timescales in TiO_2 are due to trap-limited recombination; a bulk single crystal with a sharp absorption onset is likely to contain fewer defects than a nanostructured film. Thus, it is possible that all electron–hole recombination takes place in the bulk before the µs timescale. However, the prevalence of a TA signal at long timescales in both SC-BTO and SC-STO (the latter of which has a similarly sharp absorption onset) may suggest that a TA signal should be observable. This is explored further in Section 4.4

4.3.4 Identification of $BaTiO_3$ electron and hole absorption

Chemical scavengers have previously been used to successfully characterise TA spectra of TiO_2,[32, 34] α-Fe_2O_3,[35], $BiVO_4$[36, 37] and WO_3.[27] Herein, methanol and sodium persulfate ($Na_2S_2O_8$) are used as hole and electron scavengers, respectively. Both reagents have previously been shown to react with metal oxides on sub-microsecond timescales, modulating the concentrations and lifetimes of photogenerated species, which facilitates characterisation of the optical signals[32, 38].

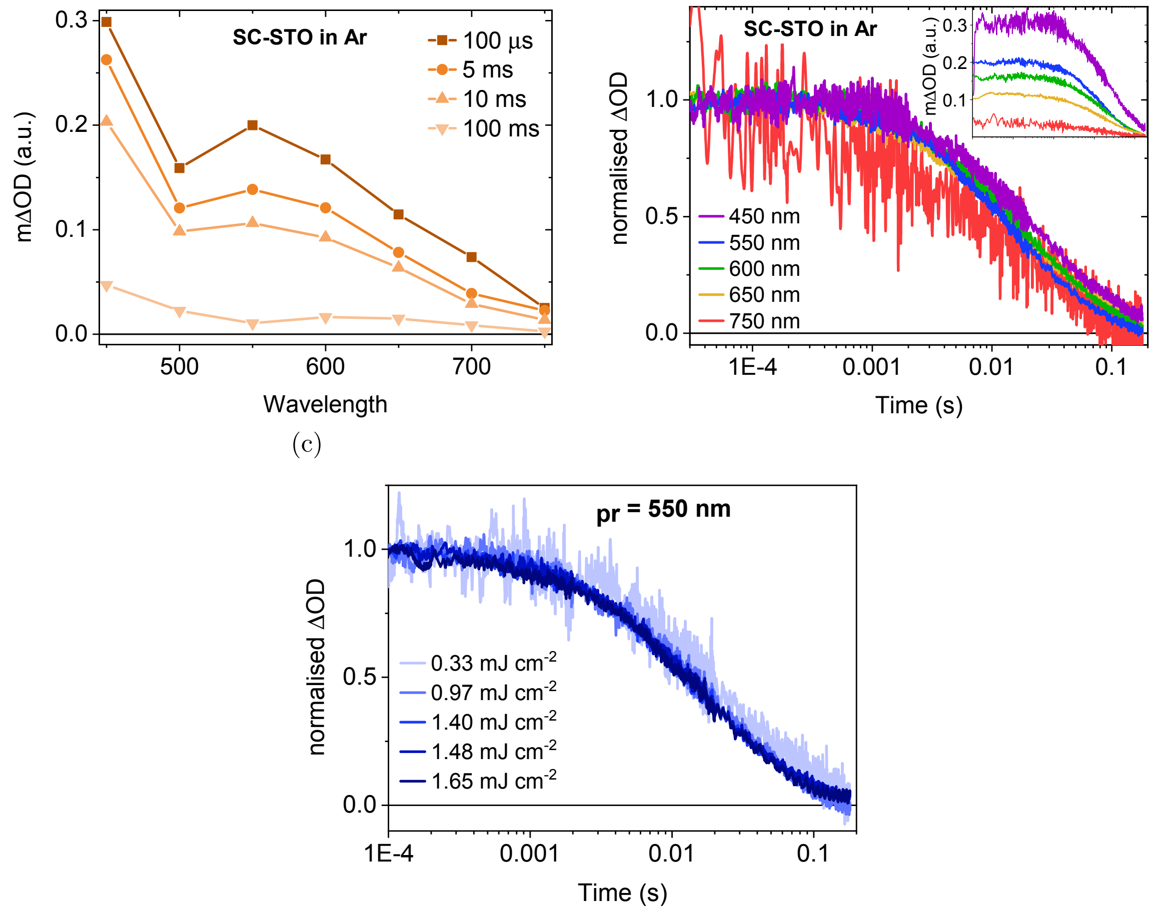
(a)

(b)

(c)

FIGURE 4.8: (a) Transient absorption spectrum of single crystal $SrTiO_3$ as a function of time after laser excitation (355 nm, 1.65 mJ cm^{-2}, 2 Hz). (b) Unnormalised and normalised (inset) decay kinetics as a function of probe wavelength. (c) $\lambda_{pr} = 550$ nm decay kinetics as a function of excitation intensity, normalised at 10 ms.

So that surface reactions can be monitored, the sample used for these measurements is a thick, tetragonal (ferroelectric) film of $BaTiO_3$ nanoparticles (tTF-BT). Figure 4.9 summarises the difference in charge carrier dynamics in tTF-BTO observed by TAS in reflectance mode on µs–s timescales.[‡] The spectrum under Ar is comparable to that of SC-BTO (Figure 4.6(a)). An enhancement in amplitude (Figure 4.9(a) and increase in lifetime (Figure 4.9(b)) observed at $\lambda_{pr} \sim 550$ nm when the sample is placed in electron scavenger $Na_2S_2O_8$, suggesting that photogenerated holes are probed in this spectral region. This is supported by the significant drop in amplitude of this signal when measurements are conducted with the sample in methanol, a hole scavenger. Also observed in a methanol environment is the increase in signal amplitude at longer wavelengths. From Figure 4.9(a) it is clear that absorption in the region 700–1000 nm increases, suggesting that this broad 'peak' can be assigned to photogenerated electrons. In the presence of scavengers, photogenerated holes have considerably longer lifetimes ($t_{50\%} \sim$ 5 ms) than photogenerated electrons ($t_{50\%} \sim$ 5 µs). This may be due to the efficiency and rate of scavenging of electrons and holes by the different chemical reagents. Both, however, are shorter lived in thick films of nanostructured $BaTiO_3$ than in bulk single crystals ($t_{50\%}$ $\sim$ 100 ms), possibly due to the magnitude of the spontaneous polarisation, discussed in detail later.

[‡] The ultrafast TAS system used was not capable of measuring diffuse-reflectance

Measurements conducted using scavengers also confirm that both the electrons and holes in $BaTiO_3$ are able to participate in surface chemistry. Often, species with observed lifetimes on the order of ms–s are deeply trapped, and thus cannot interact with the surrounding electrolyte. The dependence of charge carrier dynamics on environment here, however, is indicative of reactive charges. This reactivity is explored in Chapter 6.

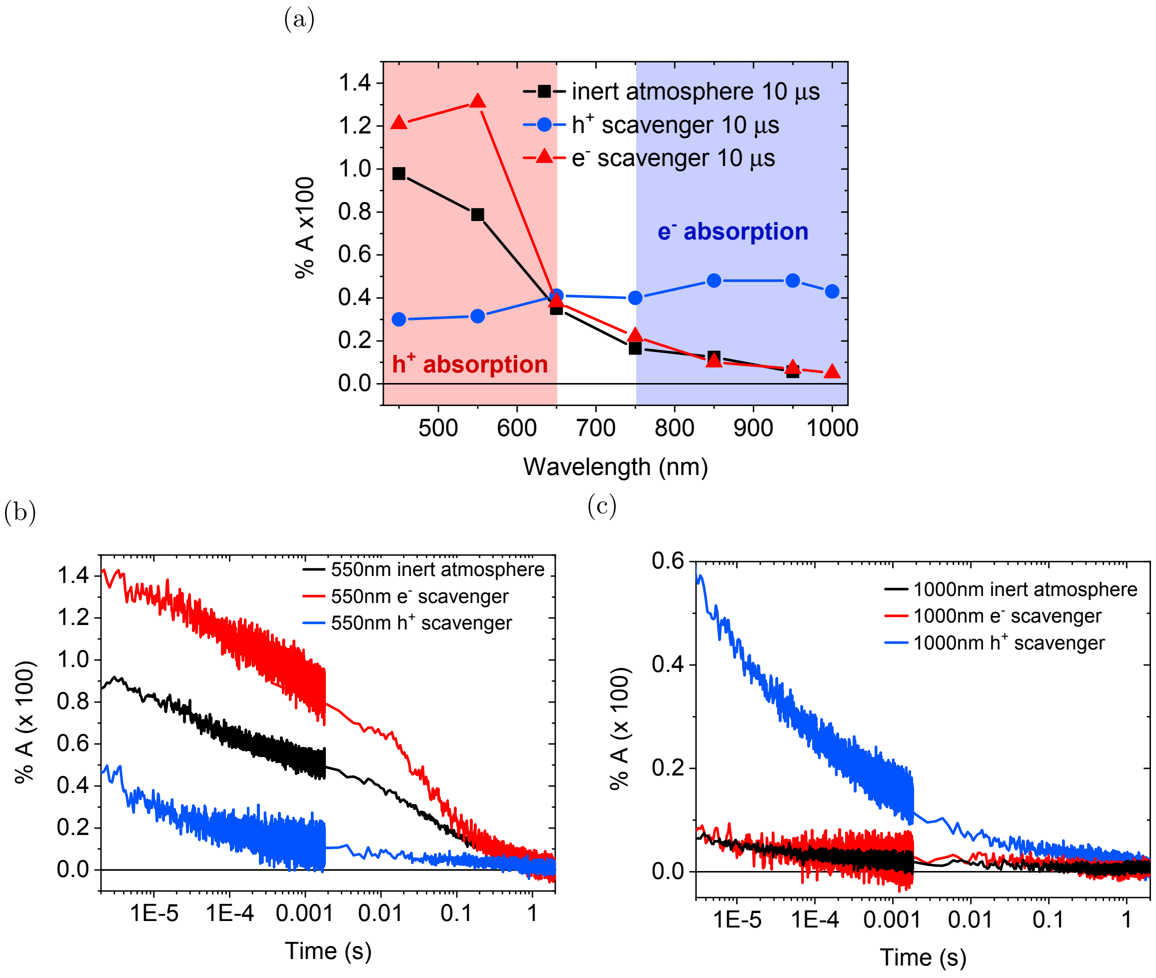

Figure 4.9: (a) Transient absorption spectra of tTF-BTO at 10 µs after 355 nm laser excitation, in an inert atmosphere (argon, black squares), hole scavenger (50% methanol, blue circles) and electron scavenger (0.1 M $Na_2S_2O_8$, red triangles). Corresponding decay kinetics at λ_{pr} of (b) 550 nm and (c) 1000 nm.

4.3.5 Summary of charge carrier dynamics

A summary of the photophysical properties acquired through this study is presented in Table 4.1, for comparable illumination conditions.

Table 4.1: Summary of photophysical properties learned from this study for single crystals of $BaTiO_3$, $SrTiO_3$ and TiO_2.

	$BaTiO_3$	**TiO_2**	**$SrTiO_3$**
fs–ns timescale			
Charge carrier lifetime	7 ns	7 ns	$\gg$7 ns
Intensity dependence	τ, amplitude	—	—
μs–s timescale			
Charge carrier lifetime	100 ms (λ_{pr}=550 nm)	—	10 ms
Intensity dependence	amplitude only	—	amplitude only
e^- absorption	550 nm	—	—
h^+ absorption	850–950 nm (peak)	—	—

4.4 Discussion

The results in this chapter, gathered using transient absorption spectroscopy (TAS), provide the first reported insight into the nature of charge carrier dynamics in $BaTiO_3$ including identification of spectral signatures of photogenerated electrons and holes. Since very little is understood about charge carrier dynamics in ferroelectric metal oxides, the observed kinetic behaviour is first discussed as a ‘conventional’ semiconductor. Comparisons with electronically similar TiO_2, of which there are several studies already reported in the literature, and structurally similar but non-ferroelectric $SrTiO_3$ aid in the understanding of the photophysical processes in $BaTiO_3$. Given the differences in behaviour observed between the two timescales, photophysical processes occurring in $BaTiO_3$ on the fs–ns will first be discussed, followed by consideration of charge carrier dynamics on the µs–ns timescale. Comparisons are made with TiO_2 and $SrTiO_3$ at ultrafast (fs–ns) timescales, however it was only possible to obtain measurements for $SrTiO_3$ at slow (µs–s) timescales. The role of the internal electric field in $BaTiO_3$ on recombination rates is briefly discussed here, and is explored more fully in Chapter 5.

Ultrafast timescales

From a few hundred fs to $\sim$ 6 ns after super-bandgap excitation, all three materials exhibit similar TA spectra and decay kinetics under comparable illumination conditions. The signals observed at these timescales are attributed to charge separated electrons and holes which recombine, causing a decay in the absorption. This is supported by excitation intensity studies of SC-BTO, which reveal that recombination rates increase with increasing intensity, and is consistent with the extremely high dielectric constant facilitating sub-fs charge separation. Following this free charge generation, the signals in SC-BTO and SC-TiO_2 remain approximately constant before beginning to decay from $\sim$ 300 ps, described by single exponential decay with a lifetime component of around 8 ns (at a intensity of 0.8 mJ cm^{-2}). This lifetime is notably longer than those observed for photogenerated electrons in dense films of TiO_2 under similar illumination levels, in a study which investigated differences in charge carrier dynamics between dense and mesoporous films of TiO_2.[20] The results of that study suggested that nanostructuring does not accelerate recombination rates on these timescales, and thus the low specific surface area in the single crystal studied here is not expected to explain the difference in lifetime.

The recombination in SC-STO is remarkably slow, with the signal amplitude staying constant until several ns. A previous transient absorption study of non-doped $SrTiO_3$ bulk single crystals under similar conditions ($\lambda_{ex} = 355\,\text{nm}$, $\lambda_{pr} = 800\,\text{nm}$, $0.5\,\text{mJ}\,\text{cm}^{-2}$) also reported long-lived TA signals.[39] At comparable excitation intensities to those used here, signals did not decay within the timescale of the measurement (2 ns). Lifetimes were reported to decrease at higher photon fluxes, however high excitation intensities ($> 4\,\text{mJ}\,\text{cm}^{-2}$) were required for significant recombination to be seen on timescales of a few ns.

Also notable in ultrafast TA measurements is the significant difference in ΔOD values between the three materials, despite similar excitation intensities being used. Differences in signal amplitudes can be caused by a number of factors:

(i) *Variation in ground state absorption (i.e. different number of absorbed photons)* – The amplitude of the TA signal can be thought of as a measure of the concentration of photogenerated species. Therefore, it might be expected that the very low apparent concentration in SC-STO could explain the slower recombination than SC-BTO and SC-TiO_2. However, UV–vis absorption data (Figure 4.2) confirms that all three materials absorb strongly beyond the bandgap. For every photon absorbed (i.e. electron promoted from the valence to the conduction band), an electron–hole pair is generated. Therefore, it is reasonable to assume that the vast majority of photons of the excitation beam are absorbed, and thus the number of electron–hole pairs should be comparable between the samples.

(ii) *Recombination faster than measurement time resolution* – Fast, geminate recombination at sub-100 fs is also unlikely to explain the discrepancy in TA amplitudes. Each of the materials has a relatively high dielectric constant which should facilitate fast and efficient charge separation to form free electrons and holes, which are likely to be the species monitored here. Although geminate recombination has been reported previously in nanostructured TiO_2 anatase films (identified by intensity-independent decay kinetics), no such recombination was observed in TiO_2 rutile films. This difference was rationalised by the fact that the larger bandgap of the anatase polymorph resulted in formation of electron–hole pairs with little excess energy, and thus insufficient driving force to facilitate their separation. The single crystal of TiO_2 used here is of rutile structure, and thus would not be expected to exhibit geminate recombination. Although SC-STO, which has the largest bandgap, shows the smallest ΔOD value, it is unlikely that this would explain the 10-fold difference between SC-BTO and SC-STO. Further, $SrTiO_3$ has a dielectric constant approximately twice that of TiO_2, and so it might be expected that if sub-ps geminate recombination was a dominant factor in signal amplitude, this would be more of an issue in SC-TiO_2.[25, 40]

(iii) *Difference in extinction coefficient of excited species* – It therefore seems most likely that the extinction coefficient of the photogenerated species differs greatly between the three metal oxides, resulting in different TA signal amplitudes. This is, however, surprising, since for each material, the valence and conduction bands should be similar in character (O 2p and Ti 3d, respectively).[16, 41, 42]

Slow timescales

Considering now the results obtained on timescales from µs to s, it is immediately apparent that the TA spectrum changes in character. The peak in photoinduced absorption in both SC-BTO and SC-STO is towards the blue, now decreasing with increasing probe wavelength. This suggests that the dominant excited state species observed at this timescale differ from those observed at ultrafast timescales. Further support to this argument comes from the intensity dependency studies. Unlike at ultrafast timescales, it is apparent from Figures 4.7 and 4.8(b) that lifetimes are not dependent on pump intensity, whilst TA amplitudes in SC-BTO and SC-BTO increase with increasing laser intensity. This is typical of pseudo-first-order kinetics, in which one carrier is in excess (expected to be electrons for these n-type semiconductors). Further, TA amplitudes of SC-BTO and SC-STO are comparable at longer timescales, no longer exhibiting a factor of 10 difference as observed in ultrafast measurements. This is consistent with different species dominating transient absorption on the two timescales. Since bimolecular recombination is observable on ultrafast timescales, it is likely that the early-time spectrum is due in equal parts to free electrons and holes. By the µs timescale, it is possible that electrons could have become trapped in states below the conduction band, leaving free hole absorption (in the blue) to dominate the spectrum.

A difference in dominant absorbing species could also explain the observation of the probe-wavelength dependency shown by slow timescale kinetics of SC-BTO, which is otherwise unexpected given the inert environment under which measurements were conducted. At longer wavelengths (assigned to photogenerated electrons), decays are approximately linear on a semi-log plot. This kind of decay has previously been associated with a tunnelling recombination process between trapped electrons and holes.[43, 44] Decays at shorter wavelengths (photogenerated holes), on the other hand, can be described by stretched exponentials with β (stretching component) of ~ 0.6. This decay shape is consistent with a distribution of energetic states which carriers decay to/from, resulting in dispersive, rather than monoexponential, decay functions (a stretching component of 1 is equivalent to a single exponential function).[28–30] A possible explanation is the presence of crystal impurities causing mid-bandgap/tail states (evident from the shallow absorption onset (Figure 4.2) and yellowish tint of SC-BTO), consistent with previous literature reports that trap states are important in recombination kinetics.[7, 8] These impurities could be reduced by photogenerated electrons before being re-oxidised by holes, causing differences between electron and hole decay kinetics. Decay kinetics in SC-STO can also be described by stretched exponential functions, and do not show probe wavelength-dependency. The absorption onset is much sharper for this sample and it is completely colourless, suggesting high purity and low defect levels. This is consistent with the hypothesis that crystal impurities in are responsible for the discrepancy between hole and electron absorption decays in SC-BTO.

Rather than internal impurities, an alternative explanation is chemical reactions occurring between surface-accumulated electrons and surface-adsorbed species. For example, oxygen is known to act as an electron scavenger on long timescales and thus faster electron decays can sometimes be caused by insufficient purging of the TAS cuvette prior to measurements. In these measurements cuvettes were thoroughly purged using Ar or N_2, and all results were highly reproducible even after heating and cooling of the sample. Further, as with the unsuccessful scavenging tests on SC-BTO, it is unlikely that enough photogenerated electrons will react with any remaining oxygen due to the very low surface area.

As mentioned previously, TA measurements on SC-TiO_2 at these timescales were unsuccessful, even under relatively high ($\sim 2.5\,\mathrm{mJ\,cm^{-2}}$) laser intensities. Previous µs-timescale TA studies of rutile films have attributed decays to recombination of trapped electrons and holes,[33, 43] and thus it could follow that single crystals of TiO_2 with sharp absorption onsets would have significantly lower levels of trap states. All recombination would, in that case, proceed bimolecularly on sub-µs timescales. However, by this logic, the same should be true of SC-STO, yet this material yields good TA signals on µs–s timescales. Performing TAS measurements of SC-TiO_2 on ns–µs timescales could elucidate whether excited state species live to these timescales.

Using thick films of nanoparticulate $BaTiO_3$, photoinduced absorption signatures of holes and electrons were identified at slow timescales. The hole scavenger (methanol) can react with photogenerated electrons in the conduction band, leaving holes in the valence band to be probed. Conversely, the electron scavenger ($Na_2S_2O_8$) allows the probing of photogenerated electrons in the conduction band by reacting with holes in the valence band. For tTF-BTO, $Na_2S_2O_8$ caused a pronounced change in the spectrum, quenching absorption towards the blue and enhancing it in the NIR region, whilst methanol caused an increase in absorption between 450 and 550 nm. This indicates that transient absorption signals from 450–550 nm can be attributed to photogenerated holes, and absorption at longer wavelengths (most prominently $\sim$ 900 nm) is due to photogenerated electrons. It is expected that the reaction of photogenerated species with chemical scavengers will occur on timescales longer than 6 ns, leaving charges at shorter timescales unperturbed. Spectral signatures could therefore not be identified at ultrafast timescales. Changes in TA spectra were not observed using single crystal samples, presumably due to the low surface area; not enough photogenerated carriers could react with the chemical reagents to induce a change in absorption.

Finally, the lifetimes observed at these timescales are considered. The $t_{50\%}$ of SC-STO is $\sim$ 10 ms, which is comparable to that of rutile TiO_2 (dense and mesoporous) reported elsewhere under similar conditions.[43] Strikingly, the $t_{50\%}$ of SC-BTO is of the order of 100 ms (for holes). This is the first known metal oxide to exhibit such a long lifetime in the absence of chemical scavengers or an applied bias.[32, 35, 45] Structurally, $SrTiO_3$ and $BaTiO_3$ are very similar; both are perovskite-type oxides (ABO_3). Crucially, however, the lower symmetry of $BaTiO_3$ induces ferroelectricity in this material. As discussed earlier, this results in significant band bending at the material surface, even under inert atmospheres. This band bending has been shown to spatially separate photogenerated electrons and holes.[46–48] It is therefore reasonable to suggest that the presence of polarisation-induced band bending causes slower recombination in $BaTiO_3$ than in $SrTiO_3$ and accounts for the order of magnitude difference in $t_{50\%}$ values. In Chapter 5, the effect of the internal field on carrier lifetimes will be investigated. It is worth noting here that the $t_{50\%}$ of tTF-BTO is $\sim$ 10 ms, an order of magnitude shorter than SC-BTO. This can perhaps be attributed to the nanostructuring in tTF-BTO causing a difference in macroscopic polarisation. Domain sizes in SC-BTO are expected to be large (on the order of µm), and thus the majority of photogenerated electrons and holes will 'feel' only one domain and one direction of band bending ('up' or 'down'). In polycrystalline nanoparticles, domain sizes are more likely to be on the same length scale as carrier diffusion lengths (1–10 nm), and thus electrons and holes may be in close proximity to both upwards and downwards band bending. In this case, the spatial separation of carriers would be less efficient than in the bulk single crystal, and could result in faster recombination. This is explored further in Chapter 5. Changes in TA spectra caused by electron and hole scavengers confirm that the photogenerated charges generated in $BaTiO_3$ are not so deeply trapped that they are chemically inactive. Their reactivity is investigated in Chapter 6.

4.5 Conclusions

Transient absorption measurements were used to identify and monitor photogenerated electrons and holes in $BaTiO_3$ over two timescales (fs–ns and µs–s). Using electron and hole scavengers, spectral signals were assigned to photogenerated holes ($\lambda_{pr} = 550\,\mathrm{nm}$) and electrons ($\lambda_{pr} \sim 950\,\mathrm{nm}$), respectively. Charge carrier dynamics were compared to those observed in chemically similar $SrTiO_3$ and electronically similar TiO_2. Similarities in spectra between the three metal oxides were observed at ultrafast and slow timescales. Interestingly, different spectra observed at each timescale suggest that two different species were monitored. Decays on ultrafast timescales were identified as bulk electron–hole recombination by excitation intensity dependence measurements, whereas long-lived species exhibit pseudo-first-order decay kinetics and are likely to arise from trapped charges. $BaTiO_3$ single crystals were found to exhibit remarkably long-lived excited state species ($t_{50\%} = 100\,\mathrm{ms}$ on slow timescales), an order of magnitude longer than single crystal $SrTiO_3$ and thick films of $BaTiO_3$, which were attributed to the polarisation-induced band bending present in ferroelectric $BaTiO_3$. Wavelength dependent decay kinetics in SC-BTO under inert atmosphere were attributed to the presence of crystal impurities. These results provide information on the signature and dynamics of charge carriers in $BaTiO_3$, and show that they are chemically active. This allows further study of the photocatalytic activity of $BaTiO_3$, as well as the effect of internal electric fields on electron–hole recombination rates.

References

[1] A. Kafizas, R. Godin, and J. R. Durrant, “Charge Carrier Dynamics in Metal Oxide Photoelectrodes for Water Oxidation”, in *Semiconductors for photocatalysis*, 97 (2017), 3–46.

[2] T. W. Kim, and K.-S. Choi, “Nanoporous BiVO4 Photoanodes with Dual-Layer Oxygen Evolution Catalysts for Solar Water Splitting”, *Science* 343, 990–994 **2014**.

[3] J. Y. Kim, G. Magesh, D. H. Youn, J. W. Jang, J. Kubota, K. Domen, and J. S. Lee, “Single-crystalline, wormlike hematite photoanodes for efficient solar water splitting”, *Scientific Reports* 3, 1–8 **2013**.

[4] Q. Liu, I. Khatri, R. Ishikawa, a. Fujimori, K. Ueno, K. Manabe, H. Nishino, and H. Shirai, “Improved photovoltaic performance of crystalline-Si/organic Schottky junction solar cells using ferroelectric polymers”, *Applied Physics Letters* 103, 163503 **2013**.

[5] Y. Tachibana, L. Vayssieres, and J. R. Durrant, “Artificial photosynthesis for solar water-splitting”, *Nature Photonics* 6, 511–518 **2012**.

[6] S. J. Hong, S. Lee, J. S. Jang, and J. S. Lee, “Heterojunction BiVO4/WO3 electrodes for enhanced photoactivity of water oxidation”, *Energy & Environmental Science* 4, 1781 **2011**.

[7] P. Ye, X. Wu, A. Blouin, C. Demers, and M.-m. D. Roberge, “Picosecond photoinduced absorption in photorefractive BaTiO3”, *Optics Letters* 16, 980 **1991**.

[8] G. a. Brost, and R. a. Motes, “Photoinduced absorption in photorefractive barium titanate.”, *Optics letters* 15, 538–40 **1990**.

[9] G. Ross, G. Montemezzani, P. Bernasconi, M. Zgonik, and P. Günter, “Strong ultraviolet induced absorption and absorption gratings in BaTiO3”, *Journal of Applied Physics* 79, 3665 **1996**.

[10] S. Acharya, S. Chouthe, H. Graener, T. Böntgen, C. Sturm, M. Grundmann, and G. Seifert, “Ultrafast dynamics of the dielectric functions of ZnO and BaTiO3 thin films after intense femtosecond laser excitation Ultrafast dynamics of the dielectric functions of ZnO and BaTiO 3 thin films after intense femtosecond laser excitation”, 053508 **2016**.

[11] T. M. Gür, S. F. Bent, and F. B. Prinz, “Nanostructuring Materials for Solar-to-Hydrogen Conversion”, *The Journal of Physical Chemistry C* 118, 21301–21315 **2014**.

[12] T. X. Ding, J. H. Olshansky, S. R. Leone, and A. P. Alivisatos, “Efficiency of hole transfer from photoexcited quantum dots to covalently linked molecular species”, *Journal of the American Chemical Society* 137, 2021–2029 **2015**.

[13] J. H. Olshansky, T. X. Ding, Y. V. Lee, S. R. Leone, and A. P. Alivisatos, “Hole Transfer from Photoexcited Quantum Dots: The Relationship between Driving Force and Rate”, *Journal of the American Chemical Society* 137, 15567–15575 **2015**.

[14] J.-i. Fujisawa, T. Eda, and M. Hanaya, “Comparative study of conduction-band and valence-band edges of TiO 2 , SrTiO 3 , and BaTiO 3 by ionization potential measurements”, *Chemical Physics Letters* 685, 23–26 **2017**.

[15] B. Modak, and S. K. Ghosh, “Origin of enhanced visible light driven water splitting by (Rh, Sb)-SrTiO 3”, *Physical Chemistry Chemical Physics* 17, 15274–15283 **2015**.

[16] D. O. Scanlon, C. W. Dunnill, J. Buckeridge, S. A. Shevlin, A. J. Logsdail, S. M. Woodley, C. R. A. Catlow, M. J. Powell, R. G. Palgrave, I. P. Parkin, G. W. Watson, T. W. Keal, P. Sherwood, A. Walsh, and A. A. Sokol, “Band alignment of rutile and anatase TiO2”, *Nature Materials* 12, 798–801 **2013**.

[17] K. Suzuki, and K. Kijima, “Optical Band Gap of Barium Titanate Nanoparticles Prepared by RF-plasma Chemical Vapor Deposition”, *Japanese Journal of Applied Physics* 44, 2081–2082 **2005**.

[18] K. Van Benthem, C. Elsässer, and R. H. French, “Bulk electronic structure of SrTiO3: Experiment and theory”, *Journal of Applied Physics* 90, 6156–6164 **2001**.

[19] S. R. Pendlebury, X. Wang, F. Le Formal, M. Cornuz, A. Kafizas, S. D. Tilley, M. Grätzel, and J. R. Durrant, “Ultrafast charge carrier recombination and trapping in hematite photoanodes under applied bias.”, *Journal of the American Chemical Society* 136, 9854–7 **2014**.

[20] M. Sachs, E. Pastor, A. Kafizas, and J. R. Durrant, “Evaluation of Surface State Mediated Charge Recombination in Anatase and Rutile TiO 2”, *The Journal of Physical Chemistry Letters* 7, 3742–3746 **2016**.

[21] T. M. Clarke, and J. R. Durrant, “Charge Photogeneration in Organic Solar Cells”, *Chemical Reviews* 110, 6736–6767 **2010**.

[22] W. J. Merz, “The Electric and Optical Behavior of BaTiO3 Single-Domain Crystals”, *Physical Review* 76, 1221–1225 **1949**.

[23] W. J. Merz, “The Dielectric Behavior of BaTiO3 Single-Domain Crystals”, *Physical Review* 75, 687–687 **1949**.

[24] C. J. Johnson, “Some Dielectric and Electro-Optic Properties of BaTiO 3 Single Crystals”, *Applied Physics Letters* 7, 221–223 **1965**.

[25] R. A. Parker, “Static Dielectric Constant of Rutile (TiO2), 1.6-1060°K”, *Physical Review* 124, 1719–1722 **1961**.

[26] A. J. Cowan, C. J. Barnett, S. R. Pendlebury, M. Barroso, K. Sivula, M. Grätzel, J. R. Durrant, and D. R. Klug, “Activation Energies for the Rate-Limiting Step in Water Photooxidation by Nanostructured α-Fe2O3 and TiO2”, *Journal of the American Chemical Society* 133, 10134–10140 **2011**.

[27] F. M. Pesci, A. J. Cowan, B. D. Alexander, J. R. Durrant, and D. R. Klug, “Charge Carrier Dynamics on Mesoporous WO 3 during Water Splitting”, *The Journal of Physical Chemistry Letters* 2, 1900–1903 **2011**.

[28] J. Nelson, and R. E. Chandler, “Random walk models of charge transfer and transport in dye sensitized systems”, *Coordination Chemistry Reviews* 248, 1181–1194 **2004**.

[29] J. N. Clifford, E. Palomares, M. K. Nazeeruddin, M. Grätzel, J. Nelson, X. Li, N. J. Long, and J. R. Durrant, “Molecular Control of Recombination Dynamics in Dye-Sensitized Nanocrystalline TiO2 Films: Free Energy vs Distance Dependence”, *Journal of the American Chemical Society* 126, 5225–5233 **2004**.

[30] S. A. Haque, Y. Tachibana, R. L. Willis, J. E. Moser, M. Grätzel, D. R. Klug, and J. R. Durrant, “Parameters Influencing Charge Recombination Kinetics in Dye-Sensitized Nanocrystalline Titanium Dioxide Films”, *The Journal of Physical Chemistry B* 104, 538–547 **2000**.

[31] S. R. Pendlebury, A. J. Cowan, M. Barroso, K. Sivula, J. Ye, M. Grätzel, D. R. Klug, J. Tang, and J. R. Durrant, “Correlating long-lived photogenerated hole populations with photocurrent densities in hematite water oxidation photoanodes”, *Energy Environ. Sci.* 5, 6304–6312 **2012**.

[32] J. Tang, J. R. Durrant, and D. R. Klug, “Mechanism of Photocatalytic Water Splitting in TiO 2 . Reaction of Water with Photoholes, Importance of Charge Carrier Dynamics, and Evidence for Four-Hole Chemistry”, *Journal of the American Chemical Society* 130, 13885–13891 **2008**.

[33] J. Nelson, S. Haque, D. Klug, and J. R. Durrant, “Trap-limited recombination in dye-sensitized nanocrystalline metal oxide electrodes”, *Physical Review B* 63, 205321 **2001**.

[34] T. Yoshihara, R. Katoh, A. Furube, Y. Tamaki, M. Murai, K. Hara, S. Murata, H. Arakawa, and M. Tachiya, “Identification of Reactive Species in Photoexcited Nanocrystalline TiO 2 Films by Wide-Wavelength-Range (400-2500 nm) Transient Absorption Spectroscopy”, *The Journal of Physical Chemistry B* 108, 3817–3823 **2004**.

[35] S. R. Pendlebury, M. Barroso, A. J. Cowan, K. Sivula, J. Tang, M. Grätzel, D. Klug, and J. R. Durrant, “Dynamics of photogenerated holes in nanocrystalline α-Fe 2 O 3 electrodes for water oxidation probed by transient absorption spectroscopy”, *Chem. Commun.* 47, 716–718 **2011**.

[36] Y. Ma, S. R. Pendlebury, A. Reynal, F. Le Formal, and J. R. Durrant, “Dynamics of photogenerated holes in undoped BiVO4 photoanodes for solar water oxidation”, *Chemical Science* 5, 2964 **2014**.

[37] N. Aiga, Q. Jia, K. Watanabe, A. Kudo, T. Sugimoto, and Y. Matsumoto, “Electron-phonon coupling dynamics at oxygen evolution sites of visible-light-driven photocatalyst: Bismuth vanadate”, *Journal of Physical Chemistry C* 117, 9881–9886 **2013**.

[38] A. Mills, and M. A. Valenzuela, “The photo-oxidation of water by sodium persulfate, and other electron acceptors, sensitised by TiO2”, *Journal of Photochemistry and Photobiology A: Chemistry* 165, 25–34 **2004**.

[39] Y. Yamada, H. Yasuda, T. Tayagaki, and Y. Kanemitsu, “Photocarrier recombination dynamics in highly excited SrTiO3 studied by transient absorption and photoluminescence spectroscopy”, *Applied Physics Letters* 95, 2–5 **2009**.

[40] H. E. Weaver, “Dielectric properties of single crystals of SrTiO3 at low temperatures”, *J. Phys. Chem. Solids* 11, 274–277 **1959**.

[41] S. Sanna, C. Thierfelder, S. Wippermann, T. P. Sinha, and W. G. Schmidt, “Barium titanate ground- and excited-state properties from first-principles calculations”, *Physical Review B* 83, 054112 **2011**.

[42] A. Dejneka, M. Tyunina, J. Narkilahti, J. Levoska, D. Chvostova, L. Jastrabik, and V. A. Trepakov, “Tensile strain induced changes in the optical spectra of SrTiO3 epitaxial thin films”, *Physics of the Solid State* 52, 2082–2089 **2010**.

[43] X. Wang, A. Kafizas, X. Li, S. J. Moniz, P. J. Reardon, J. Tang, I. P. Parkin, and J. R. Durrant, “Transient absorption spectroscopy of anatase and rutile: The impact of morphology and phase on photocatalytic activity”, *Journal of Physical Chemistry C* 119, 10439–10447 **2015**.

[44] B. Moss, K. K. Lim, A. Beltram, S. Moniz, J. Tang, P. Fornasiero, P. Barnes, J. R. Durrant, and A. Kafizas, “Comparing photoelectrochemical water oxidation, recombination kinetics and charge trapping in the three polymorphs of TiO2”, *Scientific Reports* 7, 1–7 **2017**.

[45] M. R. Morris, S. R. Pendlebury, J. Hong, S. Dunn, and J. R. Durrant, “Effect of Internal Electric Fields on Charge Carrier Dynamics in a Ferroelectric Material for Solar Energy Conversion”, *Advanced Materials* 28, 7123–7128 **2016**.

[46] J. Giocondi, and G. S. Rohrer, “Spatial separation of photochemical oxidation and reduction reactions on the surface of ferroelectric BaTiO3”, *The Journal of Physical Chemistry B* 105, 2–4 **2001**.

[47] S. V. Kalinin, and D. A. Bonnell, “Local potential and polarization screening on ferroelectric surfaces”, *Physical Review B* 63, 125411 **2001**.

[48] P. M. Jones, D. E. Gallardo, and S. Dunn, “Photochemical Investigation of a Polarizable Semiconductor, Lead-Zirconate-Titanate”, *Chemistry of Materials* 20, 5901–5906 **2008**.

Chapter 5

Ferroelectric effects on recombination rates in $BaTiO_3$

> *"There are sadistic scientists who hurry to hunt down errors instead of establishing the truth."*
>
> Marie Skłodowska-Curie

5.1 Introduction

Electron–hole recombination remains one of the key challenges in photovoltaics, artificial photosynthesis and photocatalysis.[1–3] Following light absorption, it is essential to separate photogenerated electrons and holes, and their lifetimes must match (or exceed) subsequent key energetic processes (such as charge extraction into an external circuit, or participation in surface chemistry) to ensure high device efficiencies. For water splitting devices using metal oxides, fast electron–hole recombination is particularly problematic due to slow reaction kinetics.[4, 5] The use of ferroelectrics in these devices could lead to enhanced efficiencies thanks to their ability to reduce recombination of photogenerated electrons and holes. As discussed in Chapter 2, much of the evidence to support this hypothesis lies in empirical observations of spatial separation of redox products on ferroelectric surfaces, attributed to polarisation-induced band bending which can drive electrons and holes in opposite directions.[6, 7] Spectroscopic studies, however, are lacking. In Chapter 4, the first transient absorption study of $BaTiO_3$ single crystals was presented which showed that this archetypal ferroelectric has remarkably slow electron–hole recombination at both ultrafast (ps–ns) and slow (µs–s) timescales. Strikingly, the $t_{50\%}$ value of a bulk single crystal was found to be $\sim$ 100 ms under inert atmosphere, of the same order of magnitude as timescales of photoelectrochemical water oxidation observed on some metal oxides.[4, 5] Usually, carrier lifetimes of this magnitude are only achievable in metal oxides under applied bias or in a chemical scavenger.[4, 8] In contrast, the $t_{50\%}$ value of single crystal $SrTiO_3$, a non-ferroelectric material of similar structure and bandgap, was an order of magnitude shorter than that of $BaTiO_3$. Therefore, it seems likely that the ferroelectric polarisation in $BaTiO_3$, which has been shown to drive electron–hole separation,[6, 7] could be responsible for the very low recombination rate. This chapter aims to determine the extent to which the internal electric field is responsible for the long carrier lifetimes.

The spontaneous polarisation within $BaTiO_3$ can be modulated in two ways, which allows comparison of the same material with and without an internal electric field. Firstly, like all ferroelectrics, $BaTiO_3$ can only sustain a permanent polarisation below its Curie temperature, T_C. It undergoes a 1^{st} order ferroelectric to paraelectric phase transition, meaning that below T_C, P_S decreases continuously with temperature, and drops abruptly to zero upon reaching T_C as the material switches to the non-ferroelectric cubic phase. This phase transition is fully reversible — once cooled below T_C, the tetragonal crystal structure and resultant polarisation are recovered. For bulk $BaTiO_3$, T_C is $\sim$ 120 ℃, and thus the cubic, non-ferroelectric phase is easily accessible in the single crystal investigated in Chapter 4 (SC-BTO). $BaTiO_3$ can therefore be investigated in ferroelectric and non-ferroelectric forms by performing transient absorption measurements below and above T_C. Secondly, it is well documented in the literature that reducing the particle size of $BaTiO_3$ can suppress P_S below the bulk T_C (this was discussed in more detail in Chapter 2). This facilitates the comparison of charge carrier dynamics in both the ferro- and non-ferro-electric forms of $BaTiO_3$ at room temperature.[9–13] By employing these two methods of "switching off" the polarisation in $BaTiO_3$, valuable information about how this polarisation affects charge carrier dynamics can be gained.

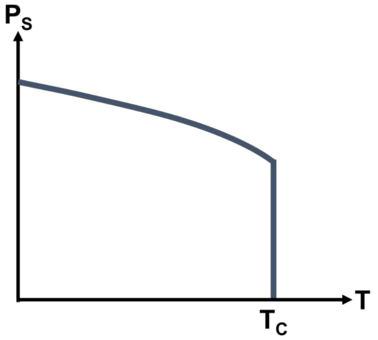

FIGURE 5.1: Relationship between P_S and T for a $BaTiO_3$, which exhibits a first order phase transition. Below T_C (120 ℃), the strength of the polarisation in the ferroelectric phase varies continuously. At T_C, $BaTiO_3$ switches between a ferroelectric tetragonal structure and a non-ferroelectric cubic one. Above T_C, P_S collapses to zero.

Variable-temperature transient absorption spectroscopy (TAS) is the main experimental method used in this chapter. To assess whether charge carrier dynamics in $BaTiO_3$ alter with temperature because of a change in polarisation strength and/or thermally activated processes inherent to metal oxides, comparisons are made throughout this chapter with analogous measurements on non-ferroelectric metal oxide films: α-Fe_2O_3, TiO_2 and $BiVO_4$, in which no phase changes are expected in the temperature range explored. As discussed in Chapter 2, these materials are popular as photoanodes for water oxidation, and as such their charge carrier dynamics at room temperature are reasonably well studied.[4, 14–19] Although the effects of temperature on charge carrier dynamics in these particular materials are not well characterised, it is generally understood that electron–hole recombination on µs–s timescales can be described by a trapping–detrapping model.[4, 20–23] In this model, bimolecular recombination deviates from 'ideal' kinetics because of some degree of disorder in the material. In the case of metal oxides, this is generally in the form of an energetic and/or spatial distribution of shallow trap states.[24] Carriers which become trapped must be thermally excited ('detrapped') to the band-edge multiple times before recombining.[25] The result of this is that the decay kinetics of transient optical signals deviate from ideal rates, and thus can often be described by power-law decays with an exponent of < 1 (an exponent of 1 corresponds to ideal bimolecular recombination).[14, 17, 18, 24] For materials exhibiting trap-limited recombination — including α-Fe_2O_3, TiO_2 and $BiVO_4$ — it is therefore expected that recombination rates will increase with increasing temperature; the more thermal energy available, the more charges will be detrapped and recombine.[22] In a ferroelectric metal oxide containing trap states, a similar trend might also be expected. However, since the strength of P_S is also dependent on T (Figure 5.1), the polarisation-driven spatial separation of electrons and holes is likely to become less effective with increasing temperature. The temperature dependence of electron–hole recombination rates in $BaTiO_3$ is therefore somewhat more complex. Characterising the temperature dependence in non-ferroelectric metal oxides allows the effect of changing the strength of P_S on charge carrier dynamics to be isolated from any other thermally activated processes (e.g. thermally activated detrapping).

Also investigated in this chapter is the effect of crystallographic orientation on charge carrier dynamics. It is known that piezo- and ferro-electric properties are dependent on crystal orientation relative to the polarisation direction, and thus it is expected that deviation of the crystal orientation from the polar c axis of tetragonal $BaTiO_3$ will result in a decreased polarisation.[26–28] The (100) oriented crystal has been shown both experimentally and computationally to exhibit the maximum value of P_S, whilst the (111) oriented crystal has a P_S expected to be around 70 % lower.[28] Variable temperature TAS studies are performed on both (100) and (111) oriented crystals to investigate the effect on charge carrier dynamics.

This study focuses on charge carriers on longer (µs–s) timescales, since these correspond to the lifetimes necessary to drive most photocatalytic or photoelectrochemical processes (e.g. water splitting).[4, 5] By comparing transient absorption (TA) decay dynamics of ferroelectric single crystals of $BaTiO_3$ (investigated in Chapter 4) to those of non-ferroelectric nanostructured films, the effect to which the internal electric field can slow electron–hole recombination is examined. By applying a simple model to the variable-temperature TAS results, the magnitude of polarisation-induced band bending at the ferroelectric $BaTiO_3$ surface is estimated.

5.2 Experimental

The $BaTiO_3$ single crystal (SC-BTO) purchased from MTI Corporation, investigated in Chapter 4, was also used in this study. In addition to this (100) oriented single crystal, a (111) oriented single crystal was purchased to investigate any effect of orientation on charge carrier dynamics. A cubic thick film of $BaTiO_3$ (cTF-BTO) prepared by screen-printing was used as the non-ferroelectric study of $BaTiO_3$ at room temperature.

The following metal oxide films were used for comparisons:

- *α-Fe_2O_3* — Nanostructured Si-doped films deposited on FTO by atmospheric pressure chemical vapour deposition (supplied by Prof Michael Grätzel's research group, EPFL).
- *$BiVO_4$* — Dense, flat films doctor-bladed onto glass (supplied by Dr Yimeng Ma, Durrant group, Imperial College London).
- *TiO_2* — Mesoporous films doctor-bladed onto glass (supplied by Dr Ernest Pastor, Durrant Group, Imperial College London).

See Chapter 3 for more details of these materials.

Ferroelectric hysteresis (P–E) loops were obtained by Chuying Yu (Queen Mary University of London) at room temperature using a triangular waveform with a maximum applied voltage of 1 kHz at a switching frequency of 5 Hz.

Variable temperature TAS measurements were conducted in transmission mode between room temperature and 152 °C using the set-up described in Section 3.3.1. Measurements were taken in ascending temperature steps. The excitation wavelength (λ_{ex}) was 355 nm for all materials, which is of greater energy than their bandgaps, whilst the probe wavelength (λ_{pr}) was tuned for each material according to its TA spectrum. $BaTiO_3$ and $BiVO_4$ were both probed at 550 nm, the peak of the hole absorption as reported in Chapter 4 and ref.[18] For α-Fe_2O_3, 690 nm was chosen as a probe wavelength as this is reported to correspond to free hole absorption and does not overlap with optical signals from holes trapped in localised intraband states.[29] Finally, transient absorption in TiO_2 was probed at both 460 and 900 nm, which correspond to hole and electron absorption, respectively.[14] The electron absorption signals of $BiVO_4$ and α-Fe_2O_3 are not well characterised, and thus only one probe wavelength is monitored.[4, 18] Laser pulse rates varied between 0.33 and 2 Hz, depending on the lifetime of the signal (samples were allowed to return to ground state between laser pulses). Excitation densities were between 150 and 300 µJ cm^{-2}. TAS cuvettes were degassed using Ar prior to measurements.

5.3 Materials characterisation

Nanoparticles used to make a thick film of $BaTiO_3$ were confirmed to be of cubic crystal phase at room temperature by powder XRD (Figure 5.2(a)), carried out by Prof Jongin Hong's research group in Chung-Ang University, Republic of Korea. The nanoparticles retained their cubic nature after screen printing onto FTO glass and calcination and subsequent cooling to room temperature (Figure 5.2(b)), demonstrated by the lack of peak splitting which is characteristic of the tetragonal phase of $BaTiO_3$. As discussed in Chapter 2, the internal field in $BaTiO_3$ can be suppressed in small nanoparticles.[11, 13]

Figure 5.2(c) indicates that the single crystal sample SC-BTO is tetragonal at 20 °C, evidenced by peak splitting at $2\theta = 45°$ (JCPDS 05-0626). At 160 °C, this peak splitting is lost, consistent with a phase transition, and resultant loss of ferroelectricity, above a T_C of 120 °C. Further evidence of room temperature ferroelectricity in SC-BTO is given by the P–E loop shown in Figure 5.2(d). The polarisation reaches saturation at approximately 22 µC cm^{-2}, in close agreement with literature values,[30] and the loop displays hysteresis characteristic of ferroelectrics (see Chapter 3 for more detail). The P–E loop of $BaTiO_3$ at temperatures > 120 °C is well documented and show that single crystal $BaTiO_3$ transitions to a paraelectric phase above T_C (it was not possible to obtain this data experimentally).[31]

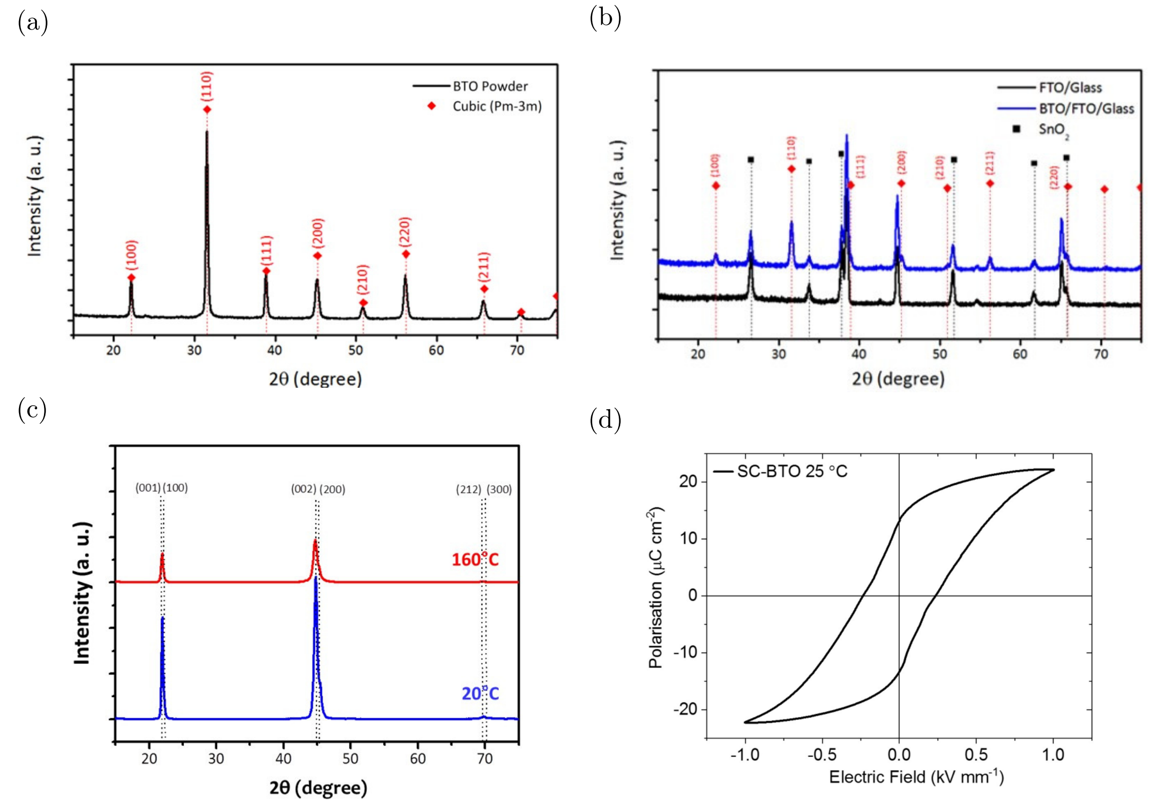

Figure 5.2: X-ray diffraction patterns of $BaTiO_3$ (a) powders and (b) thick films showing the retention of cubic phase after sintering at high temperature. (c) X-ray diffraction patterns of SC-BTO indicating different phases below and above the Curie temperature (T_C=120 °C). (d) P-E loop of SC-BTO at room temperature showing characteristic ferroelectric hysteresis.

5.4 Temperature effects on charge carrier dynamics in MOx

So that ferroelectric influences on carrier lifetimes can be distinguished from any effect of increased temperature, the temperature dependence of charge carrier dynamics are first examined in non-ferroelectric metal oxides α-Fe_2O_3, $BiVO_4$ and TiO_2.

Transient absorption decay kinetics ($\lambda_{ex} = 355$ nm) as a function of sample temperature are plotted in Figure 5.3 (a)–(d) for films of α-Fe_2O_3, $BiVO_4$ and TiO_2 at intervals between 25 and 152 °C. Room temperature lifetimes are similar to those reported previously in the literature for films of these materials.[8, 18, 32] As seen in Figure 5.3(e), the decays can be described reasonably well by power-law decays, with exponents (α) ranging from 0.17–0.27. Since smaller α values can arise from deeper traps, this indicates that, on average, traps are deepest in α-Fe_2O_3 and shallowest in TiO_2.[25] It should be noted that excitation densities were not chosen to ensure equivalent number of photons absorbed for each material in this instance. Bimolecular recombination rates are expected to vary with excitation density, and thus the obtained values of α should not be treated as exactly comparable between the materials. The obtained α values are of similar magnitude to those previously reported for TiO_2 (0.21 for anatase, 0.34 for rutile).[25]

As expected, for both α-Fe_2O_3 and $BiVO_4$ films, TA signals are observed to decay more rapidly with increasing temperature, indicating an increase in recombination rates on µs–s timescales.

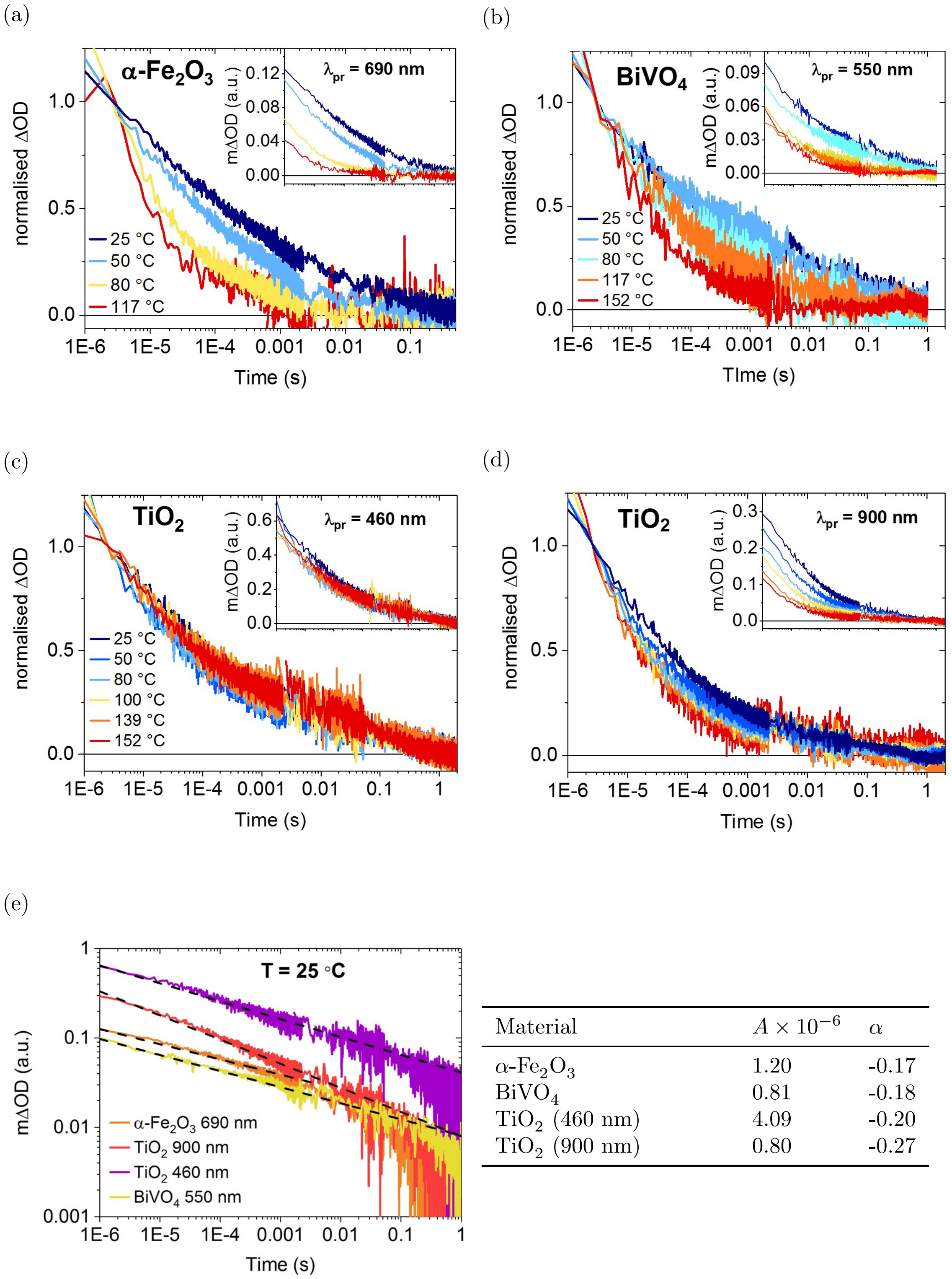

Material	$A \times 10^{-6}$	α
α-Fe_2O_3	1.20	-0.17
$BiVO_4$	0.81	-0.18
TiO_2 (460 nm)	4.09	-0.20
TiO_2 (900 nm)	0.80	-0.27

FIGURE 5.3: Normalised transient absorption decay kinetics of (a) α-Fe_2O_3, (b) $BiVO_4$ and (c)-(d) TiO_2. Inset images show unnormalised decays. $\lambda_{ex} = 355\,\mathrm{nm}$, 0.33 Hz to 2 Hz, $150\,\mu\mathrm{J\,cm^{-2}}$ to $300\,\mu\mathrm{J\,cm^{-2}}$. (e) Room temperature transient absorption decays of α-Fe_2O_3 (orange), $BiVO_4$ (yellow) and TiO_2 (purple) hole signals, and TiO_2 electron (red) signal plotted on a log-log scale. The dashed black lines are the power-law decay fits, such that $\Delta OD \propto t^{-\alpha}$. The exponent of the power-law (α) for each material is listed in the table.

This is consistent with increased thermal excitation of trapped carriers. Additionally, unnormalised TA amplitudes decrease with increasing temperature, which indicates an increase in recombination at sub-µs timescales. The same trend is observed for the electron signal in TiO_2 (λ_{pr} = 900 nm, Figure 5.3(d)). Surprisingly, however, no significant temperature dependence is observed for either the TA amplitude or $t_{50\%}$ for the hole signal in TiO_2 (λ_{pr} = 460 nm, Figure 5.3(c)). This indicates that the dominant decay process of electrons and holes differs with the electron decay being faster and more temperature dependent. This may be a result of photogenerated electrons reducing residual O_2 which may be adsorbed onto the surface of the TiO_2 film. Although all cuvettes was degassed prior to measurements, it is difficult to remove all traces of O_2. Since both α-Fe_2O_3 and $BiVO_4$ have lower-lying (more positive) conduction bands than TiO_2, it is possible that this only occurs during measurements of the latter.[33, 34] The difference may also be due to traps states or impurities. Notably, no detectable TA signal was found on µs–s timescales in the single crystal TiO_2 which was investigated in Chapter 4 on ultrafast timescales. This is consistent with a lower number of impurities and traps in a single crystal than a nanostructured thin film, and further indicates that the charge carriers being probed here are shallowly trapped.

Quantification of the observed temperature dependence of charge carrier dynamics is made using Arrhenius analysis. Plots of $\ln(1/t_{50\%})$ vs $1/T$ and derived activation energy (E_a) values are displayed in Figure 5.4 (the gradient of the straight line is equal to $-E_a/R$ where R is the gas constant). The obtained activation barrier is largest in the α-Fe_2O_3 sample at 0.30 eV, whilst smaller barriers of 0.14 and 0.09 eV are obtained for $BiVO_4$ and TiO_2 (900 nm), respectively. Since there is no significant temperature dependence observed in TiO_2 at a probe wavelength of 460 nm, no Arrhenius plot is included. These samples were measured under inert atmosphere, and thus significant surface band bending is not expected. Therefore, the temperature dependences and derived energy barriers are likely to be due to detrapping of charges from tail/shallow trap states, consistent with trap-limited recombination models.[14, 17, 18, 24] The magnitude of the barriers obtained here — a few hundred meV — is consistent with trap depths previously reported.[4, 35, 36] Further, the trend in trap depths obtained from activation energies qualitatively matches that predicted by the α values from room-temperature power-law decays (that is, that traps are deepest in α-Fe_2O_3 and shallowest in TiO_2).

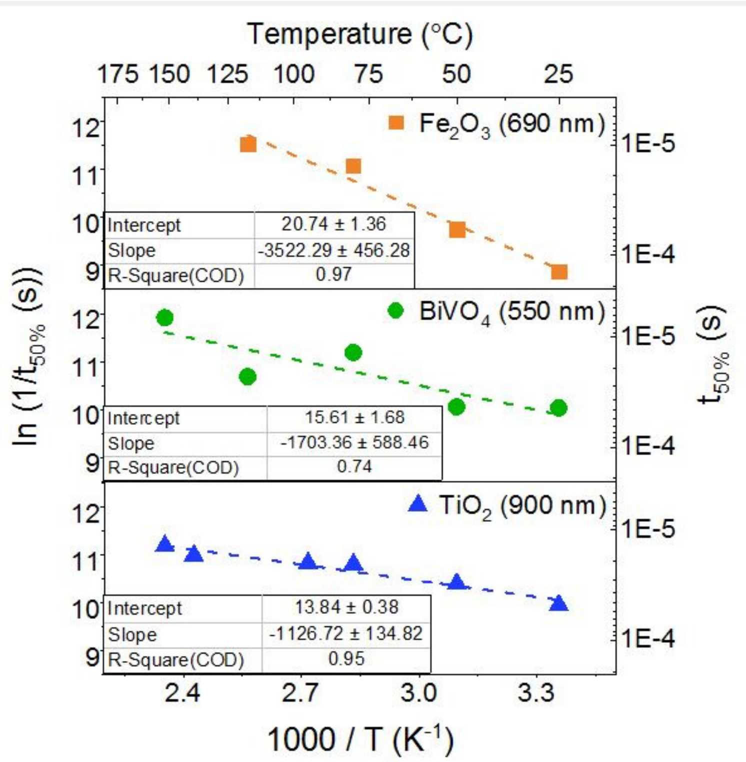

Material	Gradient $(-E_a/R)$	E_a (eV)
α-Fe_2O_3	-3522	0.30 ± 0.039
$BiVO_4$	-1703	0.14 ± 0.048
TiO_2	-1127	0.09 ± 0.011

FIGURE 5.4: Arrhenius plots of the temperature dependence of $t_{50\%}$ of α-Fe_2O_3 hole absorption signals (top, orange), $BiVO_4$ hole absorption signals (middle, green) and TiO_2 electron absorption signals (bottom, blue). All three exhibit exponential dependence on temperature, as evidenced by the straight line fits (dashed lines). Gradients and corresponding activation energy (E_a) values are shown in the table on the right.

5.5 Temperature and ferroelectric effects in $BaTiO_3$

Variable-temperature decays of single crystal $BaTiO_3$ (SC-BTO) excited at 355 nm and probed at 550 nm (corresponding to hole absorption) are shown in Figure 5.5 for temperatures between 25 and 152 °C. It is clear that the $t_{50\%}$ value in this material is significantly more sensitive to temperature than the metal oxides shown above; across the temperature range the value decreases by four orders of magnitude in $BaTiO_3$, compared to only ~ 1 for α-Fe_2O_3, TiO_2 and $BiVO_4$. Further, in contrast to the non-ferroelectric metal oxides reported above, the recombination does not follow a power-law, suggesting that trap-limited recombination is not the dominant decay mechanism here. Rather, the traces fit well to a combination of stretched exponential (where the stretching component, β, equal to 1 corresponds to a monoexponential decay) and logarithmic decay such that

$$\Delta OD(t) = Be^{-(\frac{t}{\tau})^{\beta}} + C\log_{10}(\frac{D}{t}) \tag{5.1}$$

where B, C and D are constants and τ is the time constant of the exponential component. Variation of the fitting parameters is shown in Table 5.1. Stretched exponential decays typically arise when one carrier is in excess; recombination follows pseudo-first order kinetics.[14] This is consistent with the excitation density studies presented in Chapter 4, which showed that, on µs–s timescales, $t_{50\%}$ values in SC-BTO were insensitive to the intensity of the pump beam.

The stretched exponential component dominates at low temperatures but shows a strong temperature dependence, showing little contribution to the trace at 152 °C. The decay half time of this component, τ, is particularly dependent on temperature, decreasing by four orders of magnitude over the temperature range explored. The pre-exponential factor, B (proportional to the initial signal amplitude), also decreases with increasing temperature, whilst the stretch exponent, β, remains approximately stable (0.58 ± 0.03). Since it is known that the strength of the spontaneous polarisation decreases with increasing temperature below T_C,[30] the substantial temperature dependence of this phase suggests that the associated recombination pathway is influenced by the ferroelectric nature of tetragonal $BaTiO_3$. The slower log decay phase, on the other hand, becomes more prominent at higher temperatures, but shows little temperature dependence, particularly noticeable in Figure 5.5(b). It is therefore unlikely that the recombination mechanism associated with the logarithmic phase is related to ferroelectricity. Logarithmic decays have previously been suggested to be due to tunnelling mediated recombination, arising from the presence of deep traps,[8, 25] which would not be expected to be as strongly temperature dependent.

Notably, measurements taken at the two highest temperatures (139 and 152 °C, orange and red traces, respectively), which are both above the T_C of $BaTiO_3$, do not differ significantly in their decays. This is consistent with a T_C of 120 °C; below this temperature, $BaTiO_3$ possesses a temperature-dependent polarisation, whilst heating above this results the collapse of P_S to zero. The long carrier lifetimes are recovered upon cooling back to room temperature (data not shown), consistent with the reversible switching of $BaTiO_3$ between tetragonal (ferroelectric) and cubic (non-ferroelectric) crystal structures below and above T_C.[37]

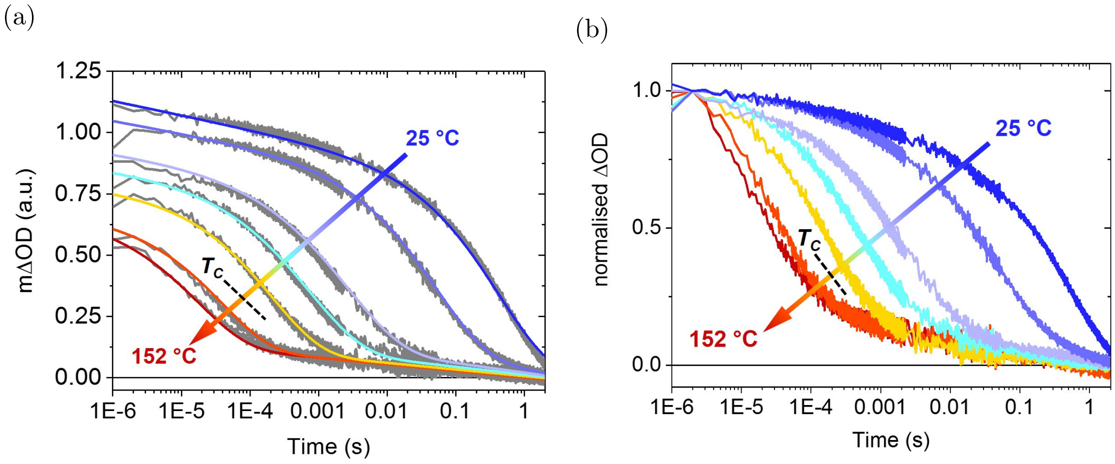

Figure 5.5: (a) Transient absorption decays of single crystal $BaTiO_3$ as a function of temperature at a probe wavelength of 550 nm. Raw data is plotted in grey, mathematical fittings (stretched exponential plus log decay components) are overlaid in colour. (b) Decays normalised at 2 µs. Dashed black lines indicate the position of the Curie temperature (120 °C).

To quantify the remarkably high temperature dependence of the stretched exponential phase of the carrier lifetime, an Arrhenius-type analysis can again be used as illustrated in Figure 5.6. The lifetime component of the stretched exponential, τ, displays an exponential dependence on temperature, T, such that $\tau \propto e^{-E_a/k_B T}$ (k_B is Boltzmann's constant). An activation energy, E_a, of 0.85 eV can be extracted from the linear fit of $\ln(1/\tau)$ vs $1/T$. This is significantly larger than the activation energies extracted for the analogous studies on α-Fe_2O_3 ($E_a = 0.30$ eV, $BiVO_4$ ($E_a = 0.14$ eV) and TiO_2 ($E_a = 0.09$ eV). As discussed above, these smaller values are consistent with detrapping-limited recombination with trap depths of a few hundered meV, which is typical for decays on these timescales for such metal oxides.[4, 38]

TABLE 5.1: Parameters for TA decay fits of SC-BTO as a function of temperature.

	Stretched exponential parameters			*Log decay parameters*	
Temperature (°C)	$B \times 10^{-4}$	β	τ (s)	$C \times 10^{-5}$	D
25	7.36	0.60	0.432	5.8	6.00
50	7.14	0.58	0.053	5.0	4.86
80	6.63	0.54	0.003	3.9	3.50
100	6.47	0.55	$7.45{\times}10^{-4}$	3.2	2.5
117	6.03	0.60	$2.12{\times}10^{-4}$	2.7	1.8
139	4.90	0.62	$4.03{\times}10^{-5}$	2.7	1.13
152	4.82	0.60	$1.77{\times}10^{-5}$	2.7	1.13

Since spontaneous polarisation in BaTiO3 is dependent on temperature, the Arrhenius analysis yields only an *apparent* activation energy. The fact that the barrier height (that is, the polarisation-induced band bending) will decrease with increasing temperature means that the temperature dependence will be exaggerated, which can explain the large E_a value obtained for SC-BTO. Further rationalisation of this number is made in the Discussion section.

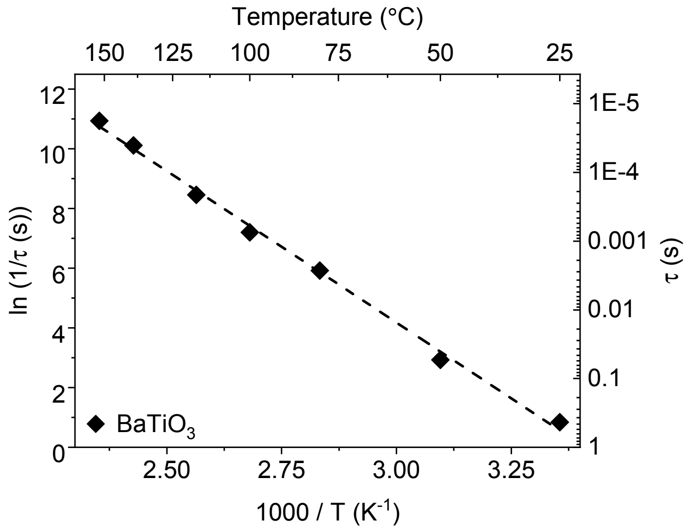

FIGURE 5.6: Arrhenius plot showing linear behaviour of τ, the stretched exponential decay phase lifetime, with temperature for SC-BTO. Symbols are experimental data points, the dashed line is the linear fit.

5.5.1 Tetragonal vs. cubic BaTiO3 at room temperature

Further investigation of the influence of ferroelectricity on carrier dynamics was conducted by comparing a cubic (non-ferroelectric) film of BaTiO3 (cTF-BTO) to the ferroelectric single crystal BaTiO3 (see Chapter 4), both at room temperature. The TA spectrum and corresponding decay kinetics are plotted in Figure 5.7. The TA spectrum, characterised by broad positive absorption which is stronger towards the blue end of the spectrum, is comparable to that of SC-BTO as discussed in Chapter 4. The kinetics, however, are remarkably different; lifetimes are < 15 µs, almost four orders of magnitude shorter than carrier lifetimes observed in SC-BTO at room temperature (~ 100 ms). These fast decay dynamics in cubic BaTiO3 are more typical of those observed for other non-ferroelectric metal oxides reported here (α-Fe_2O_3, $BiVO_4$ and TiO_2 as in Figure 5.3) and elsewhere.[4, 17, 39]

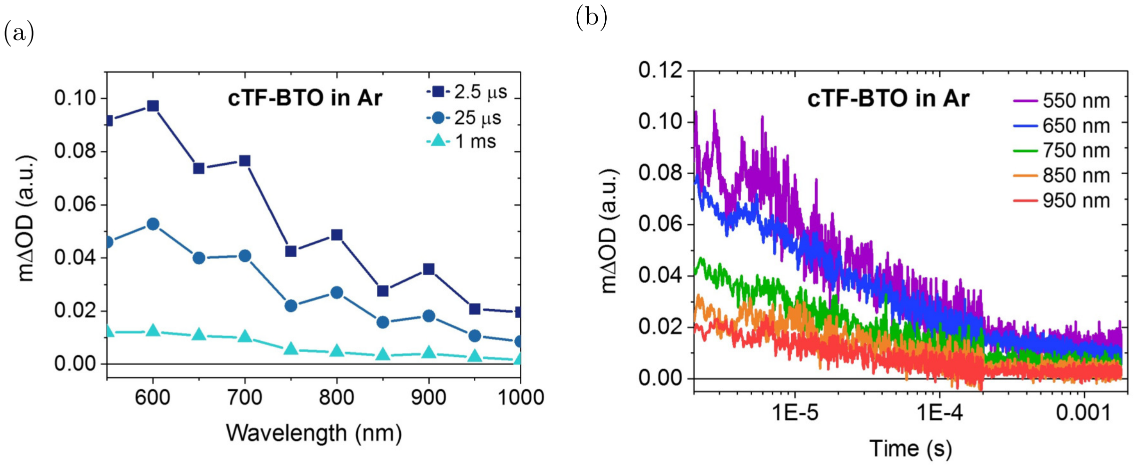

FIGURE 5.7: (a) Transient absorption spectrum and (b) corresponding decay kinetics of a thick (~4 µm) film of cubic (non-ferroelectric) $BaTiO_3$, cTF-BTO (λ_{ex} = 355 nm). (b) Corresponding decay kinetics.

Further support to the argument that electron–hole recombination rates in $BaTiO_3$ are dictated by the crystal structure — and thus by the presence or absence of an internal electric field — comes from a comparison of the kinetics cTF-BTO and SC-BTO when the latter is above T_C. Figure 5.8 shows that the decay dynamics of SC-BTO at 152 ℃ are, other than amplitude, equivalent to those of the non-ferroelectric cTF-BTO. This comparison confirms that the long lifetime in SC-BTO does not originate from the single crystal nature of this material; rather, it is the ferroelectric nature of the tetragonal phase of $BaTiO_3$ which is responsible for the long lifetimes observed in SC-BTO at room temperature. “Switching off” the internal electric field, both by nanostructuring and by heating above T_C, causes an increase in recombination rate of four orders of magnitude. The stark contrast in recombination rates between the two forms of $BaTiO_3$ — cubic and tetragonal — provides strong evidence that the driving force for charge separation is linked to the ferroelectric effect.

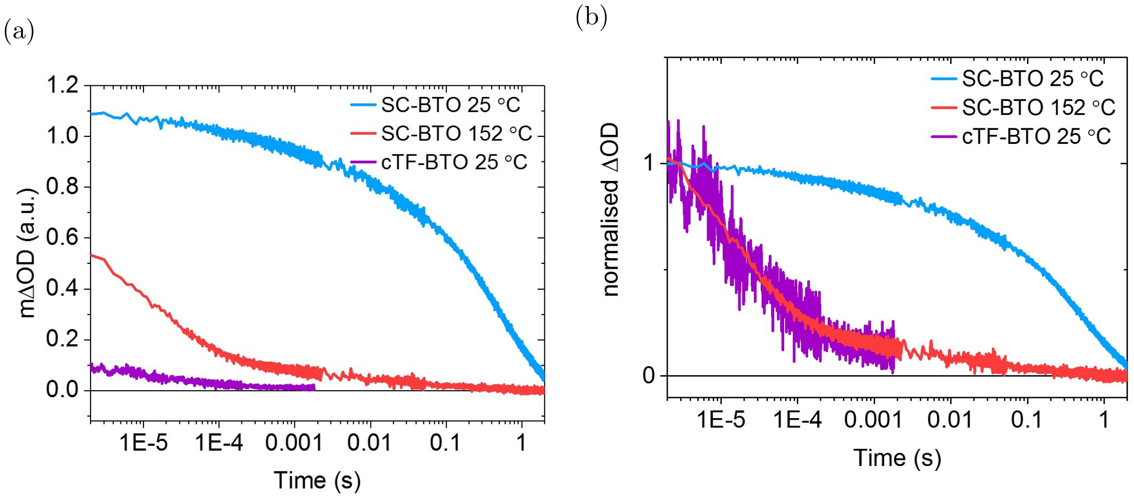

FIGURE 5.8: (a) Comparison of recombination in SC-BTO at 25 and 152 ℃ and cTF-BTO at 25 ℃ (λ_{ex} = 355 nm, λ_{pr} = 550 nm). (b) Decays normalised at 2.5 µs. SC-BTO, which is ferroelectric, exhibits very long-lived charges ($t_{50\%}$ = 0.12 s) only at room temperature. At 152 ℃, SC-BTO exhibits decay kinetics comparable with those of non-ferroelectric cTF-BTO, consistent with a loss of ferroelectricity above the Curie temperature (120 ℃)

.

5.5.2 Crystal orientation

The effect of crystal orientation was investigated by performing analogous variable-temperature TAS measurements on a (111) oriented single crystal of $BaTiO_3$, which is expected to have a lower polarisation value than the (100) oriented crystal. As can be from Figure 5.9, recombination rates in the (111) oriented $BaTiO_3$ single crystal are approximately four times faster than in the (100) oriented single crystal. This is consistent with the theory that a decreased polarisation will result in reduced band bending relative to the (100) oriented sample, and thus the barrier to electron–hole recombination will be smaller.[28]

Also apparent is the difference in the temperature dependence between charge carriers in the (111) and (100) oriented samples. As with the (100) sample, the amplitude here decreases significantly with increasing temperature, indicating more recombination at sub-µs timescales. However, as can be seen from Figure 5.9(b), no dependence on temperature is observed for the $t_{50\%}$ values of the (111) oriented sample below T_C (120 ℃). This may be due to the lower initial polarisation value resulting in a negligible change between room temperature and $\sim T_C$. Above T_C, the decay rate accelerates, which is consistent with a loss of polarisation as the material switches from tetragonal (ferroelectric) to cubic (non-ferroelectric). As with the (100) $BaTiO_3$ crystal, little difference in TA decays is observed between the two measurements taken at the highest temperatures (131 and 152 ℃), again consistent with a T_C of 120 ℃.

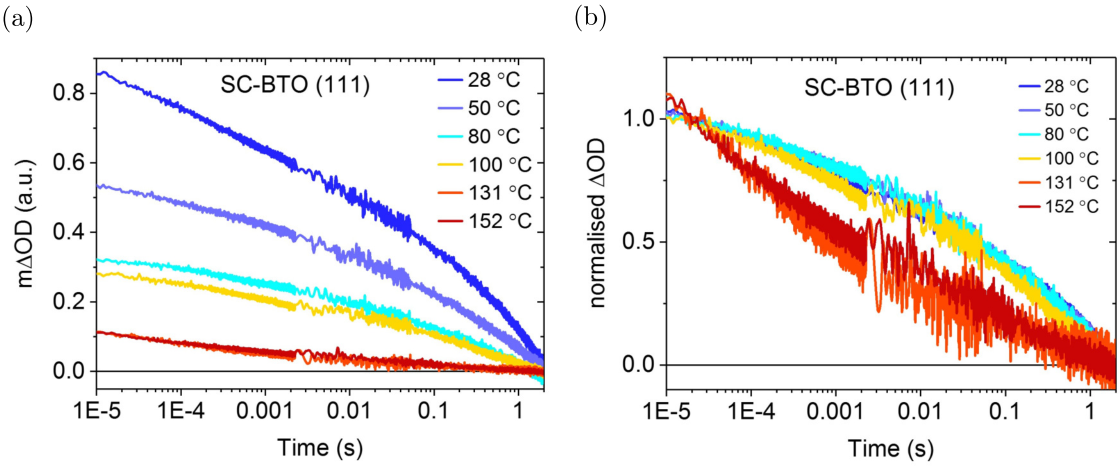

Figure 5.9: (a) Unnormalised and (b) normalised transient absorption decays of a (111)-oriented single crystal of $BaTiO_3$ as a function of temperature at a probe wavelength of 550 nm.

5.6 Discussion

All metal oxides investigated here exhibited faster charge carrier decays with increasing temperature, either at sub-µs or µs–s timescales, as expected for detrapping-limited recombination.[20, 21] The strength of the temperature dependence in α-Fe_2O_3 and $BiVO_4$ films, interpreted using an Arrhenius-type analysis, equates to activation energies on the order of a few hundred meV. Since these materials are in inert atmospheres (TAS cuvettes purged with Ar prior to measurements), little, if any, band bending should be present at the materials' surface. Therefore, it is plausible that the barriers to electron–hole recombination obtained here in α-Fe_2O_3 and $BiVO_4$ arise from the thermally activated release of trapped carriers, illustrated schematically in Figure 5.10 and similar values of trap depths have previously been reported in the literature.[4, 35, 36]

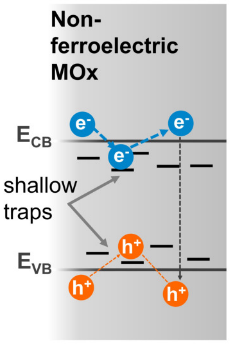

Figure 5.10: Schematic illustration of detrapping-limited recombination in metal oxides (MOx) such as α-Fe_2O_3, TiO_2 and $BiVO_4$. Electrons and holes trapped in shallow, localised trap states are be thermally detrapped to the conduction (E_{CB}) and valence (E_{VB}) band edges, before recombining. For clarity, the Fermi level has been omitted.

Surprisingly, the temperature dependence in mesopourous TiO_2 (anatase) films is different when probed at 460 nm (dominated by hole absorption) and 900 nm (dominated by electron absorption). Very little, if any, temperature dependence is observed for hole decays, in terms of both signal amplitude and carrier lifetime. Electron lifetimes, on the other hand, show a slight decrease with increasing temperature, whilst signal amplitudes show a more pronounced dependence, suggesting faster recombination at higher temperatures on sub-µs timescales. This is in contrast to previous TAS studies of TiO_2 films which found that the time constants of TA decays were identical for both electrons ($\lambda_{pr} \sim 900$ nm probe) and holes ($\lambda_{pr} \sim 460$ nm) when under inert atmospheres.[14, 40] Under such conditions, it is expected that electron–hole recombination should be the only significant process occurring, and thus decay rates should be consistent across the spectrum.[41] The change in kinetics with probe wavelength here may be due to scavenging by O_2 left in the cuvette or some residual surface-adsorbed species. It could also possibly be caused by the presence of impurities or trap states which may differ (e.g. in density or depth) between the surface and bulk. Since the TA spectrum is not completely flat,[8, 14] long and short wavelength probe beams are likely to penetrate to different depths in the material. Thus, it is possible that the difference in sensitivity to temperature observed between electrons and holes in TiO_2 is caused by a change in trap states upon heating. Further investigation into the temperature-dependence of TiO_2 are required to determine the nature of this asymmetric energy barrier. For example, conducting analogous measurements at sub-µs timescales to elucidate the early timescale temperature-dependence could aid in the explanation of why a discrepancy exists between photogenerated electrons and holes in this sample. Extended studies on different polymorphs, morphologies and fabrication methods, which could be expected to contain different levels and natures of trap states, may also aid in the understanding of these results. It is worth noting that analogous data for electron absorptions in α-Fe_2O_3 and $BiVO_4$ are not presented here; to date, neither are well characterised by transient absorption techniques, and are suggested to absorb further into the near-IR (or IR) region.[4, 18]

It is clear that the carrier lifetimes probed here in single crystals of (100) oriented $BaTiO_3$ (attributed in Chapter 4 to photogenerated holes) display a much more pronounced dependence on temperature than other metal oxides studied. The decays can be fit well by a combination of stretched exponential and logarithmic decay components, with the former becoming less dominant at higher temperatures. Each of these components shows a different relationship to temperature; the long-lived logarithmic decay component shows little variation with temperature and is thus attributed to tunnelling recombination by deeply trapped electrons and holes. The assignment of the faster, stretched exponential decay to a mechanism which is affected by the ferroelectric nature of the material has been made mainly considering the strength of the temperature dependence of this phase compared to those of other metal oxides presented here. The spontaneous polarisation in ferroelectric materials induces strong band bending, even under inert atmospheres. This band bending can be expected to act as a barrier to electron–hole recombination, and thus the activation energy extracted from an Arrhenius analysis should yield information regarding the height of the band bending. It is well known that P_S decreases with increasing temperature below T_C. It would therefore be expected that a recombination mechanism affected by ferroelectricity would have an exaggerated dependence on temperature, since to extract E_a using an Arrhenius analysis, the barrier height itself must remain constant across the investigated temperature range. Thus, the Arrhenius analysis carried out here yields only an 'apparent' activation energy of $\sim$ 850 meV for SC-BTO. To extract the true value of band bending (at a given temperature), the change in the strength of P_S must be considered.

P_S reduces with increasing temperature until T_C, when $BaTiO_3$ switches from a tetragonal crystal system to a fully centrosymmetric cubic one. This causes a drop in P_S to zero as the ferroelectric dipole is lost.[30] Since the band bending is related to the strength of P_S, the extent to which this will act as an energetic barrier (i.e. the magnitude of E_a) will decrease with increasing temperature, even below T_C, as illustrated in Figure 5.11. Literature values of P_S for $BaTiO_3$ are reported as $26\,\mu C\,cm^{-2}$ at 30 °C, reducing approximately linearly to $20\,\mu C\,cm^{-2}$ at 100 °C (a reduction of $\sim$ 25 %) and dropping to $0\,\mu C\,cm^{-2}$ at $\sim$ 120 °C.[30, 42] Similar changes have also been reported using scanning surface potential microscopy, where a 10–20 % change in surface potential was measured between room temperature and the Curie temperature,[43] and using photoelectron emission spectroscopy (PEEM), which detected a 30 % reduction in band bending upon heating.[44] Theoretical modelling has also predicted such temperature dependencies of P_S and band bending.[45] The absolute magnitude of the band bending in $BaTiO_3$ measured by PEEM under ultrahigh vacuum is reported as 0.65 V at each interface.[44] Under atmospheric conditions, the extent of band bending is likely to be reduced by screening of the polarisation, either externally (e.g. by chemisorbed surface species) or internally (by mobile charges/impurities).[46] Using the single crystalline form of $BaTiO_3$, it is likely that screening by external mechanisms will be minimal; the lack of change in TA in chemical scavengers using this sample suggests little influence of external species on charge carrier dynamics. Further, $BaTiO_3$ is a known photocatalyst,[9] thus under super-bandgap illumination conditions (as in TAS measurements) it is likely that any surface contaminants will be removed. Heating of the sample to 152 °C is also likely to aid in removal of any surface adsorbed species. On the other hand, the spectroscopic data collected herein suggest that SC-BTO contains some impurities. Therefore, it is probable that band bending in the single crystal sample of $BaTiO_3$ studied is less than that reported for a sample under vacuum.

Taking previous literature values, then, a model is proposed for the change in barrier height (E_b, attributed to band bending) across the investigated temperature range (in Kelvin) in Figure 5.11. The room temperature band bending in the sample studied here is likely to be of the order $\sim$ 0.3 V to 0.5 V, with a reduction of $\sim$ 20% upon heating to 373 K. In this temperature range, we assume that E_b decreases linearly with increasing temperature, such that

$$E_b(T) = E_b(303\,K) - \Delta E_b \frac{T - 303}{70} \tag{5.2}$$

We can therefore apply this temperature dependent barrier energy in the Arrhenius-type activation energy analysis to rationalise the apparent activation energy, E_a^{app} obtained:

$$\frac{1}{\tau} = Ae^{-\frac{E_a^{app}}{kT}} \tag{5.3}$$

Since $E_a^{app} = E_b(T)$ then

$$\begin{aligned} \frac{1}{\tau} &= Ae^{-\left(\frac{E_b(303\,K) - \Delta E_b\left(\frac{T-303}{70}\right)}{kT}\right)} \\ &= Ae^{-\left(\frac{E_b}{kT} - \frac{\Delta E_b}{70k} + \frac{303\Delta E_b}{70kT}\right)} \\ &= A'e^{-\left(\frac{E_b(303\,K)+4.3\Delta E_b}{kT}\right)} \end{aligned} \tag{5.4}$$

where $A' = Ae^{\left(\frac{\Delta E_b}{70k}\right)}$

and

$$E_a^{app} = E_b(303\,K) + 4.3\Delta E_b \tag{5.5}$$

Since the thermal barrier to recombination is itself linearly dependent on temperature, then, Arrhenius-type behaviour is still observed between room temperature and T_C, but with an increased activation energy, E_a^{app}. From ferroelectric literature, $E_b(303\,K)$ and ΔE_b are likely to be ~ 0.4 eV and ~ 0.1 eV, respectively, and an E_a^{app} value of the order of 0.83 eV is obtained. This is in good agreement with the experimentally obtained value of $E_a = 0.85$ eV, measured by variable-temperature transient absorption, supporting this proposed simple model. Thus, the strong temperature dependence of charge carrier lifetimes observed in SC-BTO is in good agreement with the expected change in polarisation-induced band bending in this material.

Lending further support to this simple model is the observation that the magnitudes of ferroelectric band bending used here are similar to the magnitudes of the electrical bias-induced band bending required in non-ferroelectric materials, such as α-Fe_2O_3, to achieve carrier lifetimes on the order of 0.1 s to 1 s, reported here for $BaTiO_3$ with no applied bias. Above T_C, TA decays display no sharp decrease in $t_{50\%}$ values. This is probably due to a shift in the dominant limitation on carrier recombination from ferroelectric-induced band bending to charge trapping effects. In addition, the lack of significant change in decay dynamics in SC-BTO above T_C is consistent with this model. Below this transition temperature, a strong temperature dependence is observed, whilst the two measurements acquired above 120 ℃ show little change. This is consistent with the loss of the temperature-dependent P_S when $BaTiO_3$ switches from the tetragonal to the cubic crystal system.

The charge carrier dynamics in the (111) oriented $BaTiO_3$ differ from this model in both the room temperature $t_{50\%}$ value, which is around four times shorter than the (100) oriented crystal, and in the lack of dependence of this value on temperature below T_C. It is known that deviation of the crystal orientation from the polar axis decreases the value of P_S, and thus is plausible that both observations can be explained by the reduced surface band bending in this sample relative to the (100) oriented crystal. The weaker P_S will induce a smaller electron–hole recombination barrier, and may be less sensitive to temperature. The marked acceleration in decays observed at temperature above 120 ℃ is consistent with the accepted value of T_C for $BaTiO_3$, which is not affected by crystallographic orientation.

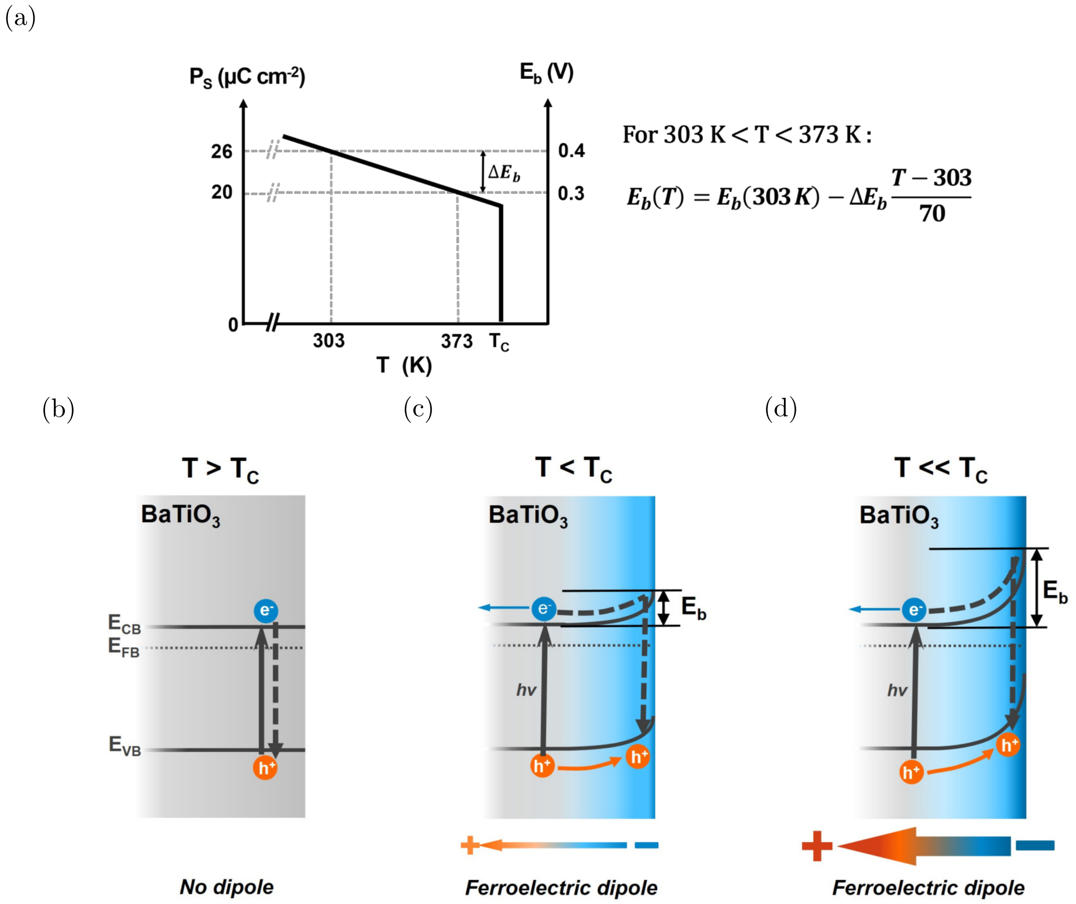

FIGURE 5.11: (a) Temperature dependence of spontaneous polarisation (P_S, left axis) and resultant band bending (right axis) in single crystal BaTiO$_3$, approximated as a linear correlation below the Curie temperature T_C for simplicity. At T_C, P_S collapses to zero, consistent with a first order phase transition from tetragonal (ferroelectric) to cubic (non-ferroelectric). (b)-(d) Schematic representations of the change in polarisation-induced band bending with temperature. Above T_C (b) BaTiO$_3$ is cubic — it has no spontaneous polarisation and thus no band bending (for clarity, any band bending induced by atmospheric or other effects has been omitted here). Below T_C (c,d), the polarisation causes the conduction and valence bands (E_c and E_v, respectively) to bend upwards (or downwards, depending on the orientation of the dipole) relative to the bulk. Dashed arrows indicate a possible recombination pathway between bulk and surface accumulated charge carriers.

These results demonstrate that ferroelectric materials have the potential to significantly increase solar conversion efficiencies in devices limited by electron–hole recombination. The magnitude of the spontaneous polarisation-induced band bending (several hundred meV) in tetragonal BaTiO$_3$, of similar magnitude to the band bending achieved by device designs such as p/n junctions and semiconductor-electrolyte junctions, is enough to induce a 10^4 increase in charge carrier lifetimes compared to the non-ferroelectric cubic BaTiO$_3$. This evidence adds to the body of literature showing that internal fields can spatially separate photogenerated charge carriers, and shows spectroscopically that this leads to a pronounced reduction in recombination rates. This reduction could lead to enhancements in solar conversion device performance in both solar fuels and photovoltaic fields. For example, carrier lifetimes observed here match the timescales reported for photoelectrochemical water oxidation on metal oxides, indicating that ferroelectrics could have particularly high impact for solar water splitting. Further, it has previously been shown that an order of magnitude decrease in recombination rate can result in an improvement of the voltage output of organic solar cells of the order of

100 mV, which could lead to significant efficiency enhancements.[47]

This study also demonstrates that optical techniques (such as transient absorption spectroscopy) can be used to investigate and estimate the magnitude of the surface band bending caused by spontaneous polarisation. Although the body of literature on ferroelectricity has been growing since the discovery of the phenomenon in the late 19th Century, reports on the barrier heights caused by band bending are surprisingly few. The simple model described herein combines variable-temperature TAS with knowledge of the temperature dependence of spontaneous polarisation in $BaTiO_3$ to estimate a band bending value which is in good agreement with literature-reported values. It is expected that this approach can be extended to estimate band bending values at other free ferroelectric surfaces.

5.7 Conclusions

The temperature dependence of charge carrier dynamics in films of non-ferroelectric metal oxides α-Fe_2O_3, TiO_2 and $BiVO_4$ was found to correlate with detrapping of charge carriers from trap depths of a few hundred meV. The very strong temperature dependence and long lifetimes of charge carriers in ferroelectric $BaTiO_3$ were attributed to the polarisation-induced band bending. Switching off this polarisation resulted in rapidly increasing electron–hole recombination, attributed to the associated decrease in band bending. Lifetimes in ferroelectric $BaTiO_3$ were found to be four orders of magnitude longer than in non-ferroelectric $BaTiO_3$, indicating that the band bending is an effective barrier to electron–hole recombination. Using variable-temperature transient absorption spectroscopy, a simple thermodynamic model was proposed which is capable of estimating the magnitude of this polarisation-induced band bending. This study clearly demonstrates the potential for ferroelectrics to significantly enhance the efficiency of solar energy conversion devices, and is applicable to both photovoltaic and solar fuels fields.

References

[1] L. M. Peter, "Towards sustainable photovoltaics: the search for new materials", *Philosophical Transactions of the Royal Society A: Mathematical, Physical and Engineering Sciences* 369, 1840–1856 **2011**.

[2] Y. Tachibana, L. Vayssieres, and J. R. Durrant, "Artificial photosynthesis for solar water-splitting", *Nature Photonics* 6, 511–518 **2012**.

[3] F. Fresno, R. Portela, S. Suárez, and J. M. Coronado, "Photocatalytic materials: recent achievements and near future trends", *J. Mater. Chem. A* 2, 2863–2884 **2014**.

[4] M. Barroso, S. R. Pendlebury, A. J. Cowan, and J. R. Durrant, "Charge carrier trapping, recombination and transfer in hematite (α-Fe2O3) water splitting photoanodes", *Chemical Science* 4, 2724–2734 **2013**.

[5] A. J. Cowan, C. J. Barnett, S. R. Pendlebury, M. Barroso, K. Sivula, M. Grätzel, J. R. Durrant, and D. R. Klug, "Activation Energies for the Rate-Limiting Step in Water Photooxidation by Nanostructured α-Fe2O3 and TiO2", *Journal of the American Chemical Society* 133, 10134–10140 **2011**.

[6] S. V. Kalinin, D. A. Bonnell, T. Alvarez, X. Lei, Z. Hu, J. H. Ferris, Q. Zhang, and S. Dunn, "Atomic Polarization and Local Reactivity on Ferroelectric Surfaces: A New Route toward Complex Nanostructures", *Nano Letters* 2, 589–593 **2002**.

[7] J. Giocondi, and G. S. Rohrer, "Spatial separation of photochemical oxidation and reduction reactions on the surface of ferroelectric BaTiO3", *The Journal of Physical Chemistry B* 105, 2–4 **2001**.

[8] X. Wang, A. Kafizas, X. Li, S. J. Moniz, P. J. Reardon, J. Tang, I. P. Parkin, and J. R. Durrant, "Transient absorption spectroscopy of anatase and rutile: The impact of morphology and phase on photocatalytic activity", *Journal of Physical Chemistry C* 119, 10439–10447 **2015**.

[9] Y. Cui, J. Briscoe, and S. Dunn, "Effect of Ferroelectricity on Solar-Light-Driven Photocatalytic Activity of BaTiO3 - Influence on the Carrier Separation and Stern Layer Formation", *Chemistry of Materials* 25, 4215–4223 **2013**.

[10] M. H. Frey, and D. A. Payne, "Grain-size effect on structure and phase transformations for barium titanate.", *Physical review. B, Condensed matter* 54, 3158–3168 **1996**.

[11] B. Begg, E. Vance, and J. Nowotny, "Effect of Particle Size on the Room Temperature Crystal Structure of Barium Titanate", *Journal of the American Ceramic Society* 77, 3186–3192 **1994**.

[12] F. Yen, H. Hsiang, and Y. Chang, "Cubic to tetragonal phase transformation of ultrafine BaTiO3 crystallites at room temperature", *Japanese Journal of Applied Physics* 34, 6149–6155 **1995**.

[13] K. Uchino, E. Sadanaga, and T. Hirose, "Dependence of the crystal structure on particle size in barium titanate", *Journal of the American Ceramic Society* 72, 1555–1558 **1989**.

[14] J. Tang, J. R. Durrant, and D. R. Klug, "Mechanism of Photocatalytic Water Splitting in TiO 2 . Reaction of Water with Photoholes, Importance of Charge Carrier Dynamics, and Evidence for Four-Hole Chemistry", *Journal of the American Chemical Society* 130, 13885–13891 **2008**.

[15] M. Sachs, E. Pastor, A. Kafizas, and J. R. Durrant, "Evaluation of Surface State Mediated Charge Recombination in Anatase and Rutile TiO 2", *The Journal of Physical Chemistry Letters* 7, 3742–3746 **2016**.

[16] T. Yoshihara, R. Katoh, A. Furube, Y. Tamaki, M. Murai, K. Hara, S. Murata, H. Arakawa, and M. Tachiya, “Identification of Reactive Species in Photoexcited Nanocrystalline TiO 2 Films by Wide-Wavelength-Range (400-2500 nm) Transient Absorption Spectroscopy”, *The Journal of Physical Chemistry B* 108, 3817–3823 **2004**.

[17] S. R. Pendlebury, M. Barroso, A. J. Cowan, K. Sivula, J. Tang, M. Grätzel, D. Klug, and J. R. Durrant, “Dynamics of photogenerated holes in nanocrystalline α-Fe 2 O 3 electrodes for water oxidation probed by transient absorption spectroscopy”, *Chem. Commun.* 47, 716–718 **2011**.

[18] Y. Ma, S. R. Pendlebury, A. Reynal, F. Le Formal, and J. R. Durrant, “Dynamics of photogenerated holes in undoped BiVO4 photoanodes for solar water oxidation”, *Chemical Science* 5, 2964 **2014**.

[19] N. Aiga, Q. Jia, K. Watanabe, A. Kudo, T. Sugimoto, and Y. Matsumoto, “Electron-phonon coupling dynamics at oxygen evolution sites of visible-light-driven photocatalyst: Bismuth vanadate”, *Journal of Physical Chemistry C* 117, 9881–9886 **2013**.

[20] J. Nelson, “Continuous-time random-walk model of electron transport in nanocrystalline TiO2 electrodes”, *Physical Review B* 59, 15374–15380 **1999**.

[21] J. Nelson, and R. E. Chandler, “Random walk models of charge transfer and transport in dye sensitized systems”, *Coordination Chemistry Reviews* 248, 1181–1194 **2004**.

[22] B. C. O’Regan, and J. R. Durrant, “Calculation of activation energies for transport and recombination in mesoporous TiO2/dye/electrolyte films-taking into account surface charge shifts with temperature”, *Journal of Physical Chemistry B* 110, 8544–8547 **2006**.

[23] A. J. Cowan, J. Tang, W. Leng, J. R. Durrant, and D. R. Klug, “Water Splitting by Nanocrystalline TiO 2 in a Complete Photoelectrochemical Cell Exhibits Efficiencies Limited by Charge Recombination”, *The Journal of Physical Chemistry C* 114, 4208–4214 **2010**.

[24] J. Nelson, S. Haque, D. Klug, and J. R. Durrant, “Trap-limited recombination in dye-sensitized nanocrystalline metal oxide electrodes”, *Physical Review B* 63, 205321 **2001**.

[25] B. Moss, K. K. Lim, A. Beltram, S. Moniz, J. Tang, P. Fornasiero, P. Barnes, J. R. Durrant, and A. Kafizas, “Comparing photoelectrochemical water oxidation, recombination kinetics and charge trapping in the three polymorphs of TiO2”, *Scientific Reports* 7, 1–7 **2017**.

[26] X.-h. Du, U. Belegundu, and K. Uchino, “Crystal Orientation Dependence of Piezoelectric Properties in Lead Zirconate Titanate: Theoretical Expectation for Thin Films”, *Japanese Journal of Applied Physics* 36, 5580–5587 **1997**.

[27] S. Wada, H. Kakemoto, and T. Tsurumi, “Enhanced Piezoelectric Properties of Piezoelectric Single Crystals by Domain Engineering”, *Materials Transactions* 45, 178–187 **2004**.

[28] A. H. Hubmann, S. Li, S. Zhukov, H. von Seggern, and A. Klein, “Polarisation dependence of Schottky barrier heights at ferroelectric BaTiO 3 / RuO 2 interfaces: influence of substrate orientation and quality”, *Journal of Physics D: Applied Physics* 49, 295304 **2016**.

[29] M. Barroso, A. J. Cowan, S. R. Pendlebury, M. Grätzel, D. R. Klug, and J. R. Durrant, “The role of cobalt phosphate in enhancing the photocatalytic activity of α-Fe2O3 toward water oxidation.”, *Journal of the American Chemical Society* 133, 14868–71 **2011**.

[30] W. J. Merz, “Double hysteresis loop of BaTiO3 at the curie point”, *Physical Review* 91, 513–517 **1953**.

[31] Y. Bai, K. Ding, G.-P. Zheng, S.-Q. Shi, and L. Qiao, “Entropy-change measurement of electrocaloric effect of BaTiO3 single crystal”, *physica status solidi (a)* 209, 941–944 **2012**.

[32] M. Barroso, C. a. Mesa, S. R. Pendlebury, A. J. Cowan, T. Hisatomi, K. Sivula, M. Grätzel, D. R. Klug, and J. R. Durrant, “Dynamics of photogenerated holes in surface modified α-Fe2O3 photoanodes for solar water splitting.”, *Proceedings of the National Academy of Sciences of the United States of America* 109, 15640–5 **2012**.

[33] M. Grätzel, “Photoelectrochemical cells”, *Nature* 414, 338–344 **2001**.

[34] H. S. Park, K. E. Kweon, H. Ye, E. Paek, G. S. Hwang, and A. J. Bard, “Factors in the metal doping of BiVO4 for improved photoelectrocatalytic activity as studied by scanning electrochemical microscopy and first-principles density-functional calculation”, *Journal of Physical Chemistry C* 115, 17870–17879 **2011**.

[35] C. Sanchez, K. D. Sieber, and G. A. Somorjai, “The photoelectrochemistry of niobium doped α-Fe2O3”, *Journal of Electroanalytical Chemistry* 252, 269–290 **1988**.

[36] F. Le Formal, S. R. Pendlebury, M. Cornuz, S. D. Tilley, M. Grätzel, and J. R. Durrant, “Back Electron–Hole Recombination in Hematite Photoanodes for Water Splitting”, *Journal of the American Chemical Society* 136, 2564–2574 **2014**.

[37] H. D. Megaw, “Crystal structure of double oxides of the perovskite type”, *Proceedings of the Physical Society* 58, 340–340 **1946**.

[38] A. Saeki, Y. Yasutani, H. Oga, and S. Seki, “Frequency-modulated gigahertz complex conductivity of TiO2 nanoparticles: Interplay of free and shallowly trapped electrons”, *Journal of Physical Chemistry C* 118, 22561–22572 **2014**.

[39] Z. Huang, Y. Lin, X. Xiang, W. Rodríguez-Córdoba, K. J. McDonald, K. S. Hagen, K.-S. Choi, B. S. Brunschwig, D. G. Musaev, C. L. Hill, D. Wang, and T. Lian, “In situ probe of photocarrier dynamics in water-splitting hematite (α-Fe2O3) electrodes”, *Energy & Environmental Science* 5, 8923 **2012**.

[40] A. Reynal, F. Lakadamyali, M. a. Gross, E. Reisner, and J. R. Durrant, “Parameters affecting electron transfer dynamics from semiconductors to molecular catalysts for the photochemical reduction of protons”, *Energy & Environmental Science* 6, 3291 **2013**.

[41] A. J. Cowan, W. Leng, P. R. F. Barnes, D. R. Klug, and J. R. Durrant, “Charge carrier separation in nanostructured TiO2 photoelectrodes for water splitting”, *Physical Chemistry Chemical Physics* 15, 8772 **2013**.

[42] T. Lee, and I. A. Aksay, “Hierarchical Structure-Ferroelectricity Relationships of Barium Titanate Particles”, *Crystal Growth & Design* 1, 401–419 **2001**.

[43] S. V. Kalinin, and D. A. Bonnell, “Effect of phase transition on the surface potential of the BaTiO3 (100) surface by variable temperature scanning surface potential microscopy”, *Journal of Applied Physics* 87, 3950–3957 **2000**.

[44] A. Höfer, M. Fechner, K. Duncker, M. Hölzer, I. Mertig, and W. Widdra, “Persistence of Surface Domain Structures for a Bulk Ferroelectric above TC”, *Physical Review Letters* 108, 087602 **2012**.

[45] H. Matsuura, “Calculation of band bending in ferroelectric semiconductor”, *New Journal of Physics* 2, 8–8 **2000**.

[46] S. V. Kalinin, C. Y. Johnson, and D. A. Bonnell, “Domain polarity and temperature induced potential inversion on the BaTiO[sub 3](100) surface”, *Journal of Applied Physics* 91, 3816 **2002**.

[47] C. G. Shuttle, B. O’Regan, A. M. Ballantyne, J. Nelson, D. D. C. Bradley, and J. R. Durrant, “Bimolecular recombination losses in polythiophene: Fullerene solar cells”, *Physical Review B - Condensed Matter and Materials Physics* 78, 1–4 **2008**.

Chapter 6

$BaTiO_3$ photocatalysis

> *"God made the bulk. Surfaces were invented by the Devil."*
>
> WOLFGANG PAULI

6.1 Introduction

As detailed in Chapter 2, the knowledge that the ferroelectric polarisation, P_S, can influence surface chemistry is well established. Studies have shown that photoreduction is promoted on $C+$ domain surfaces due to polarisation-induced downward band bending, whilst photooxidation is enhanced by upward band bending at $C-$ faces, indicating spatial separation of photogenerated charge carriers by the internal electric field.[1–3] Previous studies which have reported enhancements in photocatalytic rates using ferroelectric metal oxides have attributed the improvements, in large part, to a reduction in electron–hole recombination facilitated by this polarisation-induced band bending.[4–8] These studies generally use control systems (e.g. non-ferroelectric phases or material comparisons) to assess the influence of ferroelectricity on photocatalytic activity. However, they are lacking valuable spectroscopic studies which would allow a more complete understanding of how charge carriers are affected by an internal electric field, and how this influence relates to photocatalytic activity.

In Chapter 5 it was demonstrated, spectroscopically, that photogenerated charge carriers in $BaTiO_3$ single crystals recombine almost 4 orders of magnitude faster when the polarisation is switched off. In this chapter, spectroscopic techniques are combined with photocatalytic measurements to assess the relationship between P_S, carrier dynamics and photocatalytic activity. So that surface reactions can be monitored (and so that temperatures of 120 ℃ are not required to turn off the internal field), $BaTiO_3$ is investigated in high surface area nanopowder form, rather than bulk single crystals. As detailed in Chapter 2, $BaTiO_3$ nanoparticles can exist in tetragonal (ferroelectric) or cubic (non-ferroelectric) phases at room temperature depending on the diameters of the powders and processing conditions.[9–12] Two commercially available $BaTiO_3$ nanopowders were obtained:

1. 'Cubic' $BaTiO_3$, 50 nm diameter (BTO50)
2. 'Tetragonal' $BaTiO_3$, 500 nm diameter (BTO500)

By using these two samples, photocatalytic activities of ferro- and non-ferro-electric $BaTiO_3$ can be compared without adding temperature as an extra experimental parameter. Transient absorption spectroscopy (TAS) is used to compare charge carrier dynamics in each of the samples at room temperature under ambient conditions. The photocatalytic activity is then compared by performing both degradation of Rhodamine B (RhB) dye and water oxidation. RhB degradation by $BaTiO_3$ has already been reported in the literature, and thus provides a good comparison for the samples used here.[4–6] As discussed in detail in Chapter 2 two reported studies found that $BaTiO_3$ was a better photocatalyst for RhB photodegradation when it was 'more ferroelectric.' Cui et al. found that a sample of $BaTiO_3$ nanopowders showed a higher photocatalytic activity when the tetragonal content had been increased by annealing.[4] Su et al. also reported faster dye degradation rates using $BaTiO_3$ nanopowders at room temperature than at 80 ℃, which they attributed to the reduced P_S strength at higher temperatures.[6] Photocatalytic water splitting on bare $BaTiO_3$ surfaces is, to the best of my knowledge, currently unreported. The valence band of $BaTiO_3$ lies at a sufficiently oxidising potential ($\sim +2.7$ V vs RHE) to drive the water oxidation half-reaction.[13] Although the conduction band of $BaTiO_3$ should lie at a slightly more reducing potential than the proton reduction reaction (~ -0.5 V vs RHE [13]) it likely that this will not provide sufficient overpotential to enable overall water splitting at a measurable rate. Thus, for practicality, the water oxidation half reaction is monitored in the presence of a chemical electron scavenger.

Finally, photoinduced absorption spectroscopy (PIAS) is used to further compare charge carrier dynamics between the $BaTiO_3$ samples under water oxidation conditions. PIAS can be a useful tool for probing long-lived charge carriers which accumulate at the surface of photoelectrodes before reacting, and therefore is used for investigating the behaviour of charge carriers under working conditions (i.e. continuous light). It has recently been used in conjunction with electrochemical techniques to carry out rate law analyses of photocatalytic reactions on metal oxide surfaces, including water oxidation, methanol oxidation and proton reduction.[14–16] Here, PIAS is used to compare, qualitatively, the accumulation and reaction rates of photogenerated holes in ferroelectric (tetragonal) and non-ferroelectric (cubic) $BaTiO_3$ nanopowders under different light intensities to assess whether an internal ferroelectric field will affect carrier behaviour on reaction timescales (ms–s).

The combination of these methods of time-resolved spectroscopy with empirical reaction rate determination is used to extract useful information about the photochemistry of ferroelectric and non-ferroelectric $BaTiO_3$.

6.2 Experimental

6.2.1 Materials

Commercially bought (US Nanoresearch Materials Inc.) $BaTiO_3$ powders of diameters stated as 50 nm (BTO50) and 500 nm (BTO500) in diameter were used as-received in the monitoring of photocatalytic activity throughout this chapter. Commercially bought (US Nanoresearch Materials Inc.) TiO_2 powders of diameter 500 nm ($TiO_2$500) were also used in water oxidation reactions as a control material.

6.2.2 Spectroscopic techniques

Transient absorption spectroscopy

Transient absorption measurements were obtained in reflectance mode using bandgap excitation (355 nm, 200 µJ per pulse) on µs–s timescales. Full details of the instrument set-up are given in Chapter 3. The probe wavelength was set at 550 nm, close to the hole absorption of both $BaTiO_3$ and TiO_2, and the pulse rate was set at 0.33 Hz to allow samples to return to ground state before being excited again. Powder samples were not degassed prior to measurements.

Photoinduced absorption spectroscopy

Photoinduced absorption measurements were collected in reflectance mode using monochromatic 365 nm LED light with a photon flux which was varied between 1.4 and 5.5 mW by varying the current passing through the LED. Table 6.1 lists the set currents and corresponding power at the sample position. PIA signals were measured continuously for a 60 s period (5 s on/55 s off). A probe wavelength of 550 nm was chosen to allow monitoring of photogenerated holes in $BaTiO_3$. The set-up of the equipment is described in more detail in Chapter 3.

$BaTiO_3$ and nanopowders were affixed to a glass slide using an epoxy resin. The area illuminated and exposed to electrolyte is comparable between the samples, however it should be noted that the powder coverage was not highly uniform. Slides were submerged in the electrolyte (0.1 M $Na_2S_2O_8$) and not degassed prior to measurements.

Table 6.1: Current passing through 365 nm LED light and corresponding power measured at sample position.

Current (A)	Power (mW)
0.05	1.4
0.1	2.7
0.2	5.5

6.2.3 Photocatalysis set-up

Rates of degradation of rhodamine B ([9-(2-carboxyphenyl)-6-diethylamino-3-xanthenylidene]-diethylammonium chloride, RhB, 10 ppm) and of water oxidation in the presence of an electron scavenger (sodium persulfate, $Na_2S_2O_8$, 0.1 M) were monitored under super-bandgap LED light (365 nm, 30–70 mW). Solutions were not degassed prior to measurements. Reaction rates were determined by measuring the evolution of UV–vis absorption (dye degradation) and oxygen production (water oxidation). Oxygen evolution was measured in the gas phase using a Clark electrode (Unisense OX-NP).

Full details of experimental set-ups and conditions can be found in Chapter 3.

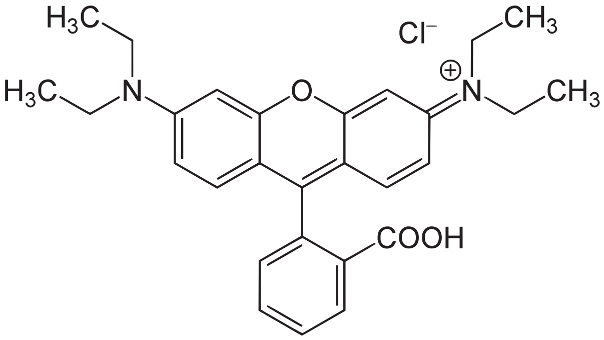

Figure 6.1: Structure of Rhodamine B, [9-(2-carboxyphenyl)-6-diethylamino-3-xanthenylidene]-diethylammonium chloride.

Oxygen quantification

The oxygen sensor (Clark electrode) was manually calibrated by injecting known volumes of air (and hence known volumes of O_2, V_{O_2}) into the vial following water oxidation experiments, and measuring the change in sensor reading ($\Delta sensor$, mV). The ideal gas equation was used to obtain the number of moles of oxygen injected:

$$moles\ O_2 = \frac{pV_{O_2}}{RT} \tag{6.1}$$

where p is the pressure (1 atm) and R is the gas constant (0.082 L atm mol^{-1} K^{-1}). Plotting $\Delta sensor$ vs $moles\ O_2$ gives a calibration curve which can be used to calculate the rate of oxygen production for each of the samples. An example calibration curve is shown in Figure 6.2. Individual calibrations were performed for each sample.

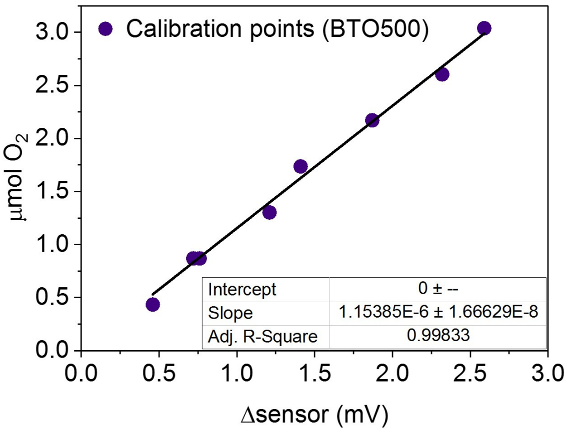

Figure 6.2: Clark electrode (O_2 sensor) calibration curve under conditions of BTO500 measurements.

6.3 Results

6.3.1 Materials Characterisation

UV–vis diffuse reflectance spectra of the as-received $BaTiO_3$ nanopowders are shown in Figure 6.3. The Kubelka–Munk (K–M) function, $F(R)$, can be derived from the diffuse reflectance spectrum and used as an absorption coefficient equivalent:

$$F(R) = \frac{(100 - R)^2}{2R} \tag{6.2}$$

where R is the diffuse reflectance relative to a reference sample.[17] This value can then be used to determine the bandgaps, E_g by constructing Tauc plots (Figure 6.3, inset) according to the relation for a direct bandgap semiconductor

$$F(R)h\nu = A(h\nu - E_g)^{0.5} \tag{6.3}$$

where A is a constant and $h\nu$ is the photon energy in eV.[18] The obtained bandgaps are 3.10 and 3.15 eV for BTO500 and BTO50, respectively, within the expected range of 3.00–3.20 eV reported in the literature for $BaTiO_3$.[19, 20]

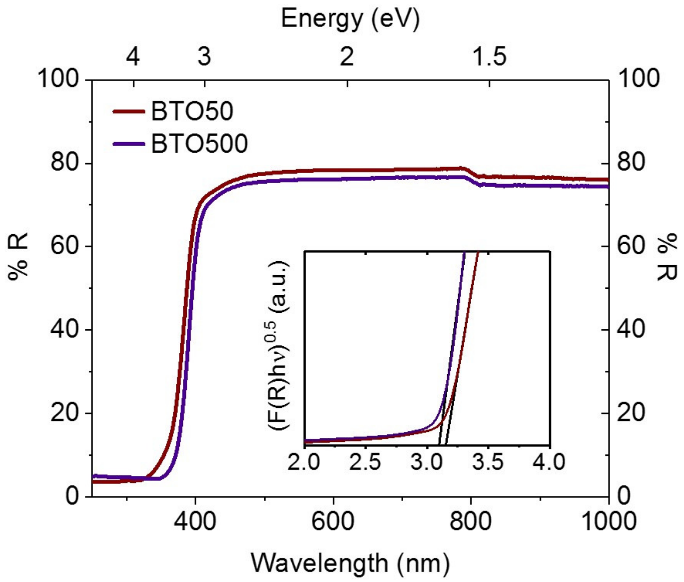

FIGURE 6.3: UV–vis diffuse reflectance of spectra of $BaTiO_3$ nanopowders of diameters ∼ 50 and ∼ 500 nm.

Scanning electron microscopy (SEM) micrographs are shown in Figure 6.4 (a-c), revealing the difference in particle size between BTO50 and BTO500. Whilst both have non-uniform size distributions, the former generally has particle diameters of ∼ 50 nm, whilst the latter has much larger particles of diameters > 300 nm.

Since ferroelectric and non-ferroelectric $BaTiO_3$ have different unit cell symmetries, structural characterisation can be used to identify whether or not a sample will possess a spontaneous polarisation. The phase composition of the powders was determined by X-ray diffraction (XRD) (Figure 6.4 (d-e)). The single peak observed at $2\theta = 45.2°$ for BTO50 indicates a predominantly cubic structure, consistent with literature reports that surface-related strain effects in small (< 100 nm diameter) can stabilise the non-ferroelectric phase at room temperature.[9, 11, 21] BTO500, which has a much larger diameter, displays clear peak splitting due to its lower symmetry tetragonal structure. This sample is therefore assumed to be predominantly ferroelectric.* Further confirmation of the difference in structure is given qualitatively by solid state ^{137}Ba NMR (Figure 6.4 (f)). The asymmetry present in tetragonal BTO500 results in a complex peak pattern, whilst the totally symmetric BTO50 has a simple spectrum with a single dominant peak.[24]

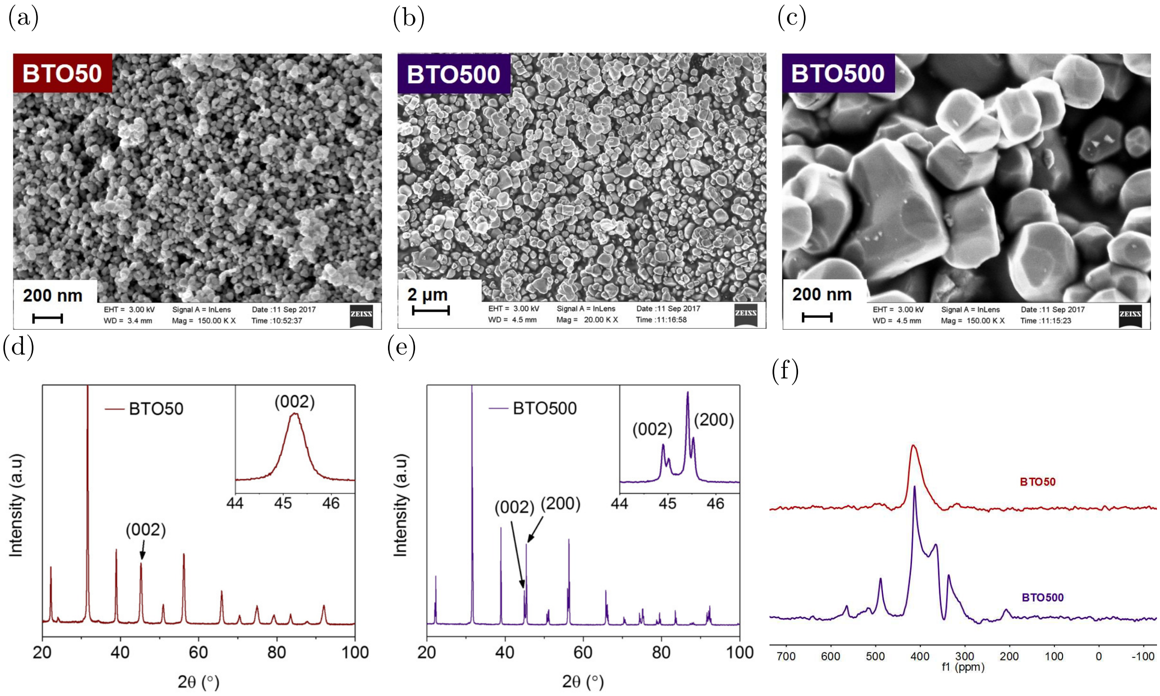

Figure 6.4: SEM images of commercially obtained nanopowders of $BaTiO_3$ with diameters of (a) ~ 50 nm (BTO50) and (b-c) ~ 500 nm (BTO500). Powder XRD patterns of (d) BTO50 and (e) BTO500, confirming two different crystal phases (cubic and tetragonal, respectively). Inset images are high-resolution analyses of the region around $2\theta = 45°$. (f) Solid state ^{137}Ba NMR spectra of BTO50 (red, top) and BTO500 (purple, bottom).

6.3.2 Transient absorption spectroscopy

Transient absorption spectra

Transient absorption spectroscopy was used to compare the nanopowders used in this chapter to the $BaTiO_3$ sample used in Chapter 4 and literature reports of TiO_2. TA spectra, obtained using an excitation wavelength of 355 nm are shown in Figure 6.5. Due to experimental constraints, measurements of powder samples were conducted in air. O_2 was therefore present, which can act as an electron scavenger and thus result in a TA spectrum dominated by hole absorption.

As with the single crystal form of $BaTiO_3$ (Chapter 4), the excited state absorption of BTO500 nanopowders (mounted onto glass using epoxy adhesive) is characterised by broad, positive

---

[*] No P–E hysteresis loops were performed on these sample, however it is widely accepted that ferroelectricity arises from the asymmetry in the tetragonal unit cell, and thus BTO500 should be ferroelectric, whilst the centrosymmetric structure of BTO50 is cubic and non-ferroelectric.[22, 23]

absorption which is strongest towards the blue end of the spectrum. Compared to the single crystal $BaTiO_3$ measured in Chapter 4, absorption is more dominant at shorter wavelengths, indicating the occurrence of some electron scavenging. Similarly, the TA spectrum of the TiO_2 nanopowder is broad and positive with stronger absorption of shorter wavelengths. Whilst previous TAS reports for TiO_2 under inert atmospheres are usually characterised by a flatter, less defined spectrum, the spectrum reported here more closely resembles that of the TiO_2 hole absorption previously reported.[25, 26] This again indicates that the TA spectrum is dominated by hole absorption due to scavenging of electrons by O_2.

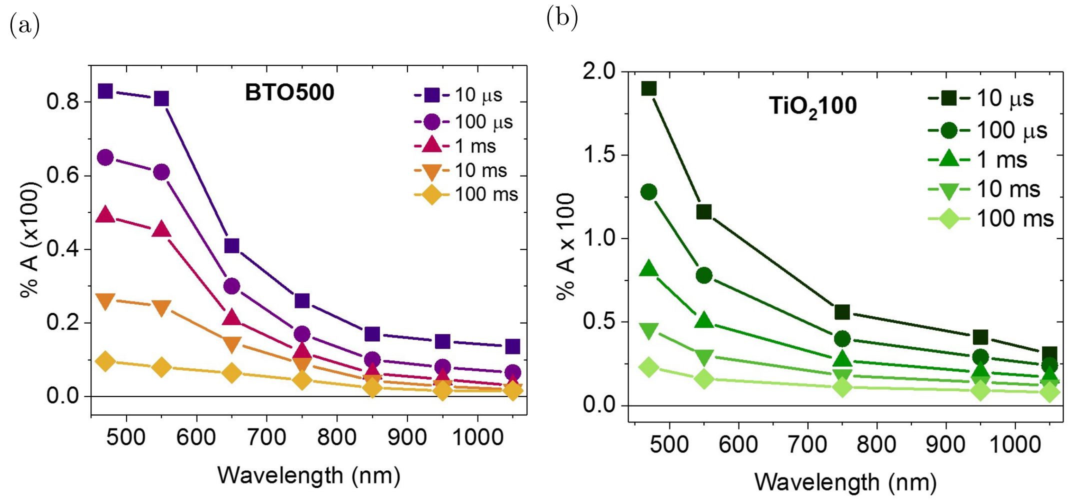

FIGURE 6.5: Time evolution of the transient absorption spectra of (a) $BaTiO_3$ nanopowder (500 nm diameter) mounted onto a glass slide using an epoxy resin and (b) TiO_2 nanopowder, both in air.

Transient absorption decays

The TA decay kinetics of the $BaTiO_3$ and TiO_2 nanopowders of different diameters are shown in Figure 6.6 (a) and (b), respectively. Notably, whilst the signal amplitude of TiO_2 does not vary with particle size, BTO500 was found to consistently show $\%A$ values approximately three times that of BTO50. Since both are expected to absorb the same number of photons at 355 nm, this difference indicates that more charge carriers live to µs–ms timescales in the ferroelectric BTO500 than in the non-ferroelectric BTO50. This result is consistent with those presented in Chapter 4 which found that electron–hole recombination is slowed by the internal field present in ferroelectric $BaTiO_3$. Interestingly, however, the normalised decays of both $BaTiO_3$ nanopowders are identical, suggesting identical nature of recombination pathway. TAS studies in Chapter 4 found that the lifetimes of charge carriers in tetragonal, ferroelectric $BaTiO_3$ are almost four orders of magnitude longer lived than those in non-ferroelectric $BaTiO_3$, and thus a similar observation is expected here. This suggests that, although XRD patterns indicate that BTO50 is predominantly cubic, some tetragonal phase is also present, which would induce ferroelectricity and thus slow recombination. Mixed phases of $BaTiO_3$ nanostructures have been reported in the literature.[4] Also apparent from these decay kinetics is the difference in recombination rates between $BaTiO_3$ and TiO_2. $TiO_2$500 shows fast power law kinetics consistent with trapping/detrapping limited bimolecular recombination,[25, 27] whilst BTO500 shows slower, more stretched exponential-type kinetics analogous to those observed in the ferroelectric single crystal $BaTiO_3$ presented in Chapter 4.

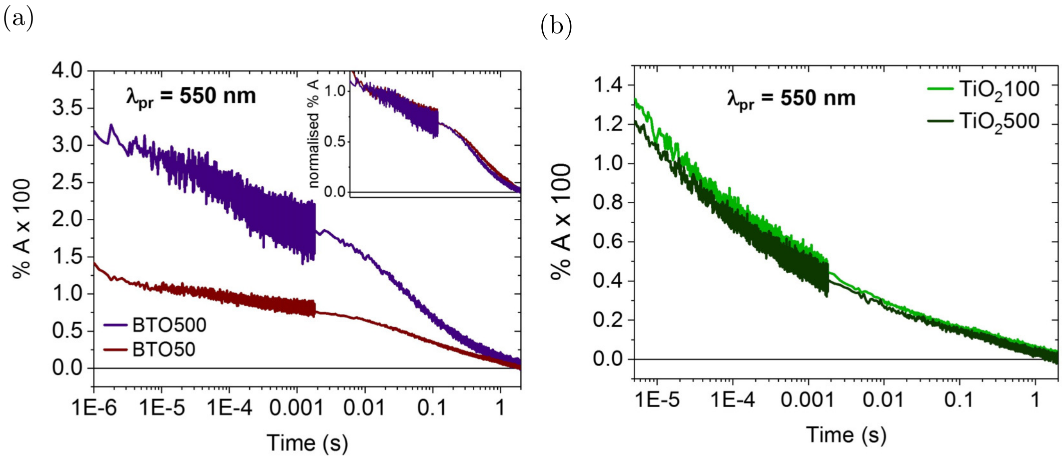

Figure 6.6: Transient absorption decays of commercially-obtained nanopowders of (a) $BaTiO_3$ (50 and 500 nm diameters, normalised data inset) and (b) TiO_2 (100 and 500 nm diameters). Decay lifetimes are not observed to vary with particle size for either metal oxide. A difference in amplitude between the two $BaTiO_3$ samples is apparent, indicating a higher concentration of excited state species (holes) in the larger, ferroelectric particles than in the smaller, non-ferroelectric particles.

6.3.3 Degradation of Rhodamine B

In Chapter 4, chemical scavengers were used to characterise the transient absorption spectrum of $BaTiO_3$. The change in absorption spectrum with chemical environment also confirmed that, in samples with a high surface area, the photogenerated charges are reactive and can participate in chemical reactions. Therefore, it is possible to investigate any effect of ferroelectricity on photocatalytic activity by monitoring photocatalytic reactions of BTO50 and BTO500.

The photocatalytic activities of BTO50 and BTO500 were first assessed through decolourisation of RhB under super-bandgap (365 nm) light. Results are summarised in Figure 6.7 and Table 6.2. The peak of maximum RhB absorption (λ_{max} = 554 nm), which is proportional to dye concentration, decreased with increasing irradiation time for both photocatalysts, indicating that photodecolourisation occurs in the presence of both ferroelectric and non-ferroelectric $BaTiO_3$. The sample taken at 0 min represents the concentration of dye after reaching adsorption–desorption equilibrium (30 min in the dark), and the absorption intensity at 554 nm was then taken as $Abs(0)$. It is noticeable that the $Abs(0)$ values are comparable between experiments. Previous reports of dye degradation by ferroelectrics have reported that stronger adsorption of dye molecules on ferroelectric surfaces are associated with the internal electric field which can enhance photochemical activity.[4, 28] Here, however, the similarity in $Abs(0)$ values suggests little difference in levels of dye adsorption to BT50 and BT500 surfaces.

Table 6.2: Summary of change in concentration and number of moles of Rhodamine and observed rates of decolourisation by BTO50 and BTO500.

	ΔC (mol L^{-1})	Δn (mol)	Time (min)	Rate (mol min^{-1})	Area-normalised rate (mol min^{-1} cm^{-2})
BTO50	1.23×10^{-5}	2.46×10^{-7}	200	1.23×10^{-9}	1.02×10^{-13}
BTO500	8.6×10^{-6}	1.72×10^{-7}	259	6.64×10^{-10}	5.35×10^{-13}

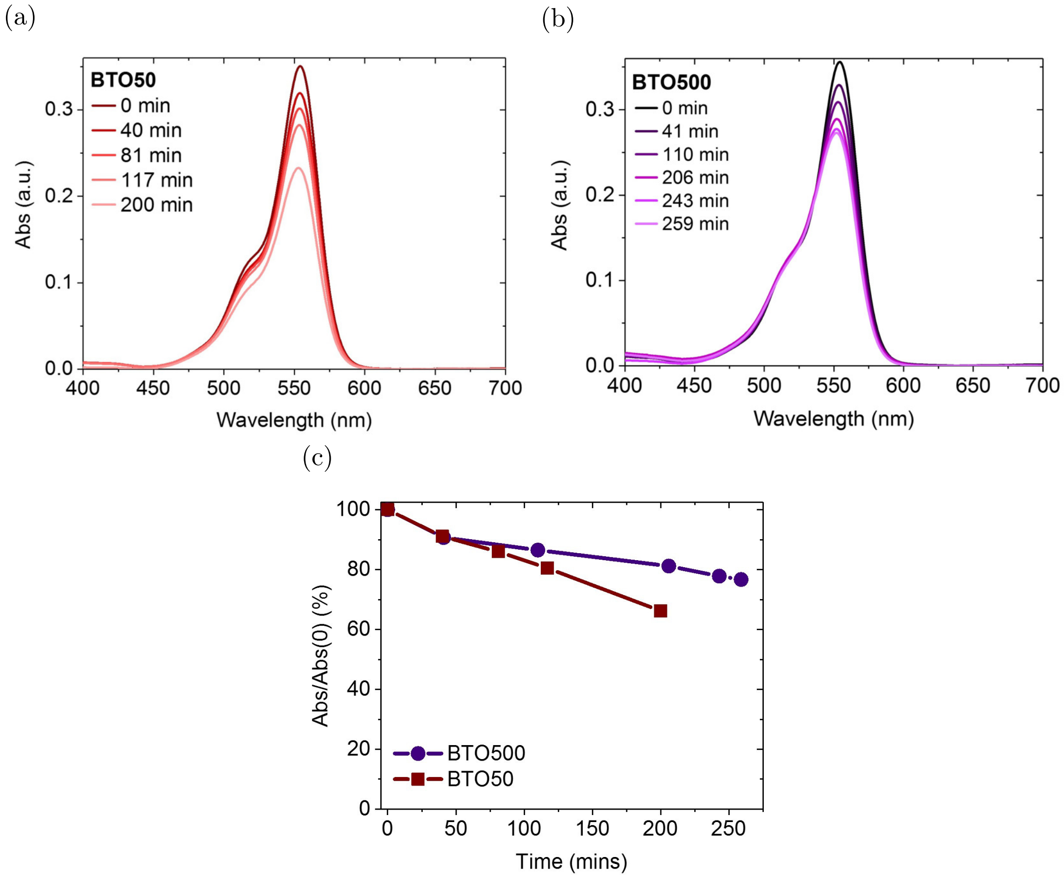

FIGURE 6.7: Evolution of UV–vis absorption spectra of RhB solution (10 ppm) loaded with (a) BTO50 and (b) BTO500 and exposed to monochromatic light (365 nm LED, 30 mW) for an extended period of time. (c) Corresponding photodecolourisation profiles of RhB using BTO50 (maroon, squares) and BTO500 (purple, circles).

Generally, it is assumed that the rate of photocatalytic decolourisation of organic compounds, such as RhB, is proportional to surface area; the greater the surface area, the higher the number of adsorption sites and thus the faster the reaction. The rate should therefore follow a Langmuir–Hinshelwood (LH) kinetic model.[4, 29] For dilute solutions ($< 1\,\mathrm{mmol\,L^{-1}}$), the observed rate constant, k_{obs} can be described by Equation 6.4:

$$ln(\frac{C(0)}{C}) = k_{obs}t \tag{6.4}$$

where C(0) is related to the initial dye concentration ($\mathrm{mol\,L^{-1}}$, using absorption at λ_{max}). Plotting $ln(C(0)/C)$ vs t (Figure 6.8) then allows determination of the photodecolourisation rate, k_{obs}. k_{obs} values and rate constants normalised for surface area, k_{norm} are shown in Table 6.3. Sample surface areas were estimated using the supplier-stated particle diameters (50 and 500 nm), $BaTiO_3$ density ($6.02\,\mathrm{g\,cm^{-3}}$) and mass of photocatalyst used in photodegradation measurements ($\sim 60\,\mathrm{mg}$).

Using this method of analysis, observed rate constants of 0.0020 and $0.0012\,\mathrm{min^{-1}}$ are obtained for BTO50 and BTO500, respectively. These values are of the same order of magnitude reported by Cui et al., ($k_{obs} = 0.0012\,\mathrm{min^{-1}}$ for ~390 nm diameter $BaTiO_3$ nanopowders under 1 Sun solar simulated light).[4] However, the results presented here differ in that the k_{obs} value of the tetragonal BTO500 is lower than that of the predominantly cubic BTO50.

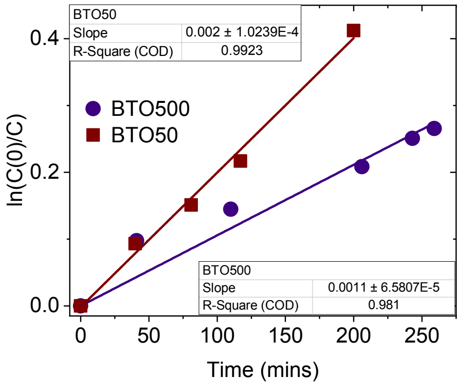

FIGURE 6.8: Rate of photodecolourisation of RhB by $BaTiO_3$ photocatalysts, determined using a Langmuir-Hinshel model.

TABLE 6.3: Experimentally observed rate constants for photo-decolourisation of RhB by $BaTiO_3$ nanopowders under 365 nm LED light.

	Total surface area (cm^2)	k_{obs} (min^{-1})	k_{norm} ($min^{-1}\,cm^{-2}$)
BTO50	1.21×10^4	$0.0020 \pm 1.02 \times 10^{-4}$	$1.65 \times 10^{-7} \pm 8.4 \times 10^{-9}$
BTO500	1.24×10^3	$0.0012 \pm 6.58 \times 10^{-5}$	$9.68 \times 10^{-7} \pm 5.3 \times 10^{-8}$

Cui et al. reported that, despite having a much lower surface area, the annealed sample with a higher tetragonal content had a k_{obs} value 3 times that of the unannealed, less tetragonal sample.[4] This was attributed by the authors to the expectation of enhanced charge separation in the annealed sample, however any effects due to a change in crystallinity or surface defect levels were not discussed. In the results presented here, BTO500 has k_{norm} value more than five times that of BTO50. This is in closer agreement with the TAS results in which BTO500 was shown to have a higher number of charge carriers as BTO50 on µs–s timescales (on which the photocatalytic reaction is likely to take place). It is also in agreement with the findings of Chapter 5 which showed that the spontaneous polarisation in ferroelectric $BaTiO_3$ reduce electron–hole recombination, and thus more charges are available to participate in photocatalysis than in the non-ferroelectric sample. Such findings of ferroelectric-enhanced activity have been reported previously for dye degradation on $BaTiO_3$[4] as well as other photocatalytic reactions on ferroelectric surfaces.[28, 30, 31]

6.3.4 Water oxidation

In addition to the dye degradation studies, the photocatalytic activities of BTO50 (predominantly cubic, non-ferroelectric) and BTO500 (predominantly tetragonal, ferroelectric) were investigated by measuring water oxidation in the presence of an electron scavenger ($Na_2S_2O_8$) under 365 nm LED light. For comparison, analogous studies were conducted on BTO500 in water without an electron scavenger, and using 500 nm diameter TiO_2 powders ($TiO_2$500) in 0.1 M $Na_2S_2O_8$. A Clark electrode was used to measure the oxygen produced in the head-space of the reaction vessel. Calibration of the Clark electrode allowed conversion of sensor changes (in V) to moles of O_2 produced. Results of the measurements are summarised in Figure 6.9 and Table 6.4.

Both BTO50 and BTO500 produce oxygen under super-bandgap illumination. The unnormalised rate of BTO50 is ~ 40 % higher than BTO500, however when normalised for surface

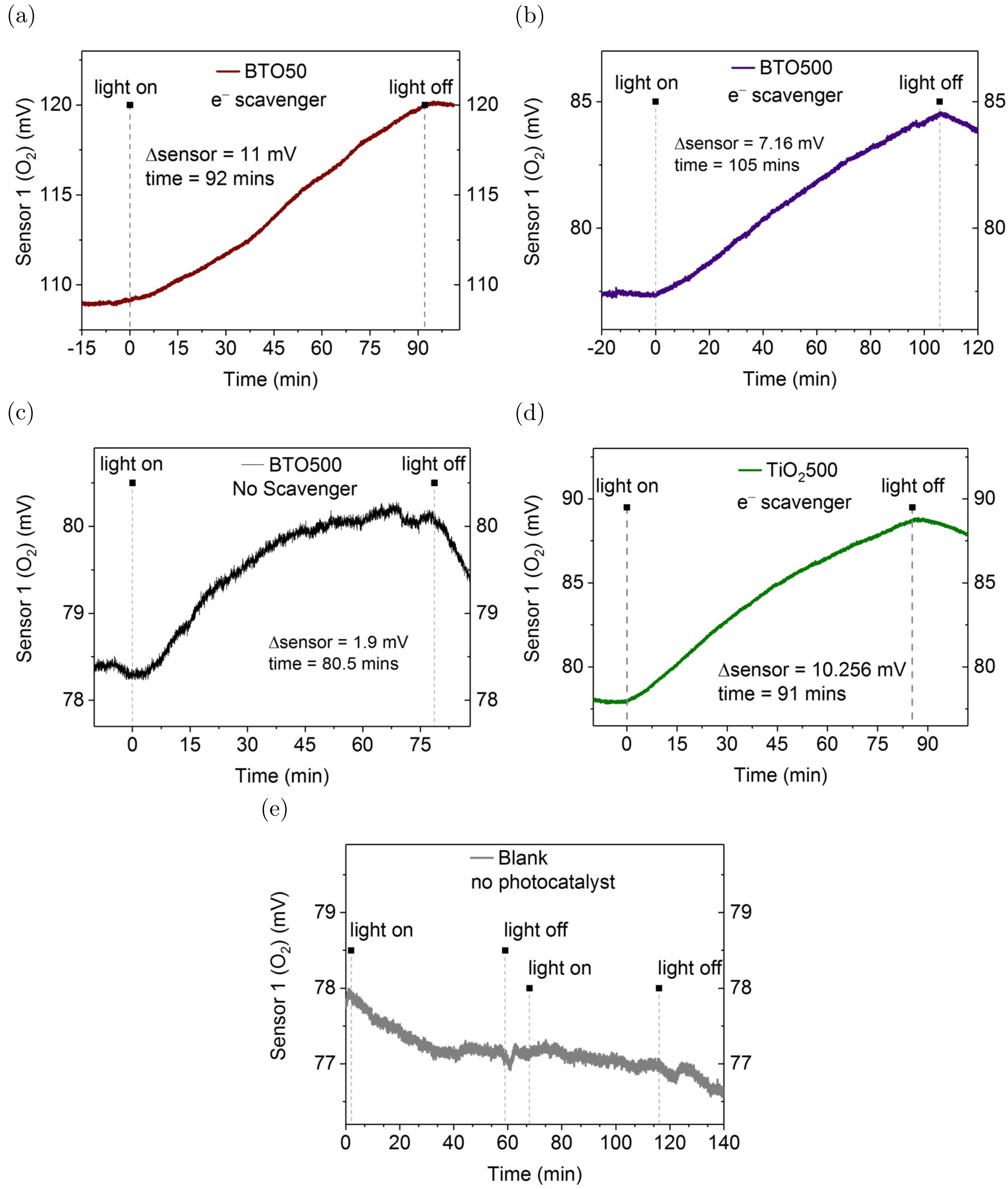

FIGURE 6.9: Oxidation production from water using (a) BTO50 (b-c) BTO500 and (d) $TiO_2$500 under 365 nm LED light (70 mW). (e) Shows the sensor response of a blank control measurement which contains no photocatalyst.

TABLE 6.4: Rates of O_2 evolution by $BaTiO_3$ and TiO_2 nanopowders under 365 nm LED light.

	Electrolyte	Total surface area (cm^2)	Rate (mol O_2 h^{-1})	Area-normalised rate (mol O_2 h^{-1} cm^{-2})
BTO50	$Na_2S_2O_8$	7970	6.6×10^{-6}	8.28×10^{-10}
BTO500	$Na_2S_2O_8$	825	4.72×10^{-6}	5.72×10^{-9}
BTO500	Water	813	2.4×10^{-6}	2.95×10^{-9}
$TiO_2$500	$Na_2S_2O_8$	1140	8.5×10^{-6}	7.35×10^{-9}

area, BTO500 outperforms BTO50 by a factor of almost 7. This higher rate is consistent with a decreased rate of electron–hole recombination in BTO500 due to its higher degree of tetragonality and hence ferroelectricity. As confirmed by the TAS measurements (Figure 6.6(a)), more charge carriers are present on µs–s timescales; a faster rate of water oxidation is therefore expected. It is worth noting that whilst the amplitude of TA signals of BTO500 are ~ 3 times those of BTO50, these measurements were not conducted in an electron scavenger. It is likely that in the presence of $Na_2S_2O_8$, the difference in amplitude would be larger and perhaps comparable to the factor of 7 difference in observed reaction rate.

Analogous measurements were conducted using BTO500 in water in the absence of a scavenger (Figure 6.9(c)). The change in sensor reading is of similar magnitude to that seen in the blank control measurement (Figure 6.9(e)), however does appear to correlate with the illumination time, unlike the control. If the increase in sensor reading is, in fact, due to oxygen generation, the significantly reduced rate could be attributed to the fact that, without an electron scavenger, the slow reduction reaction (proton reduction) becomes the bottleneck because of the lack of a strong driving force provided by the position of the $BaTiO_3$ conduction band. Oxygen production is therefore hindered in the absence of an electron scavenger. Figure 6.9(e) shows the response of the O_2 sensor during a measurement of a blank control sample. No photocatalyst was added and the reaction vessel was exposed to same intensity of 365 nm light. Throughout the duration of the measurement, the change in the sensor reading is $< 1.2\,\mathrm{mV}$, and does not correlate with the light being switched on and off. The change in the sensor reading is therefore not attributable to any consequences of illuminating water with the LED light (e.g. liberation of dissolved oxygen over time or changes in pressure due to temperature changes). In all measurements the O_2 level no longer increases once the light is switched off. The decrease in sensor reading in the experiment using BTO500 may be due to a leak in reaction vessel; the observed reaction rates are therefore estimates.

The rate of oxygen evolution by $TiO_2$500 in an electron scavenger is faster than that of BTO500. This indicates that, although the concentration of charge carriers in $TiO_2$500 is significantly lower than in BTO500 on µs–s timescales, TiO_2 is a better photocatalyst for water oxidation than $BaTiO_3$. This may be due to inherent material properties (e.g. different surfaces result in a difference in bond/adsorption strengths of reaction intermediates), or could be a result of a difference in trap densities and ability of long-lived charges to react with the electrolyte.

6.4 Photoinduced absorption study of water oxidation on $BaTiO_3$

The water oxidation reaction on $BaTiO_3$ was investigated further using photoinduced absorption spectroscopy (PIAS). Conditions were similar to the oxygen evolution measurements reported above (i.e. 0.1 M $Na_2S_2O_8$, 365 nm LED illumination). Figure 6.10 shows the PIA signals of $BaTiO_3$ nanopowders BTO50 (left) and BTO500 (right) measured as a function of LED light intensity in water (top) and $Na_2S_2O_8$ (bottom). For all signals, a positive absorption signal is seen to increase when the light is switched on, which decays when the light is switched off. In such measurements, decays can be attributed to carrier recombination or to charge transer to the electrolyte. Here, it is clear that hole accumulation and decay dynamics are affected by environment; in water, both BTO50 and BTO500 optical signals reach a steady state in $< 5\,\mathrm{s}$, whilst in the persulfate electron scavenger, charge carrier accumulation takes considerably longer, particularly in the predominantly cubic BTO50. Signal amplitudes are also larger in $Na_2S_2O_8$ than in water. Since amplitudes are directly proportional to the accumulated density of photogenerated species, this is consistent with efficient electron scavenging by $Na_2S_2O_8$, which results in a larger yield of long-lived holes than in the absence of scavenger.[32]

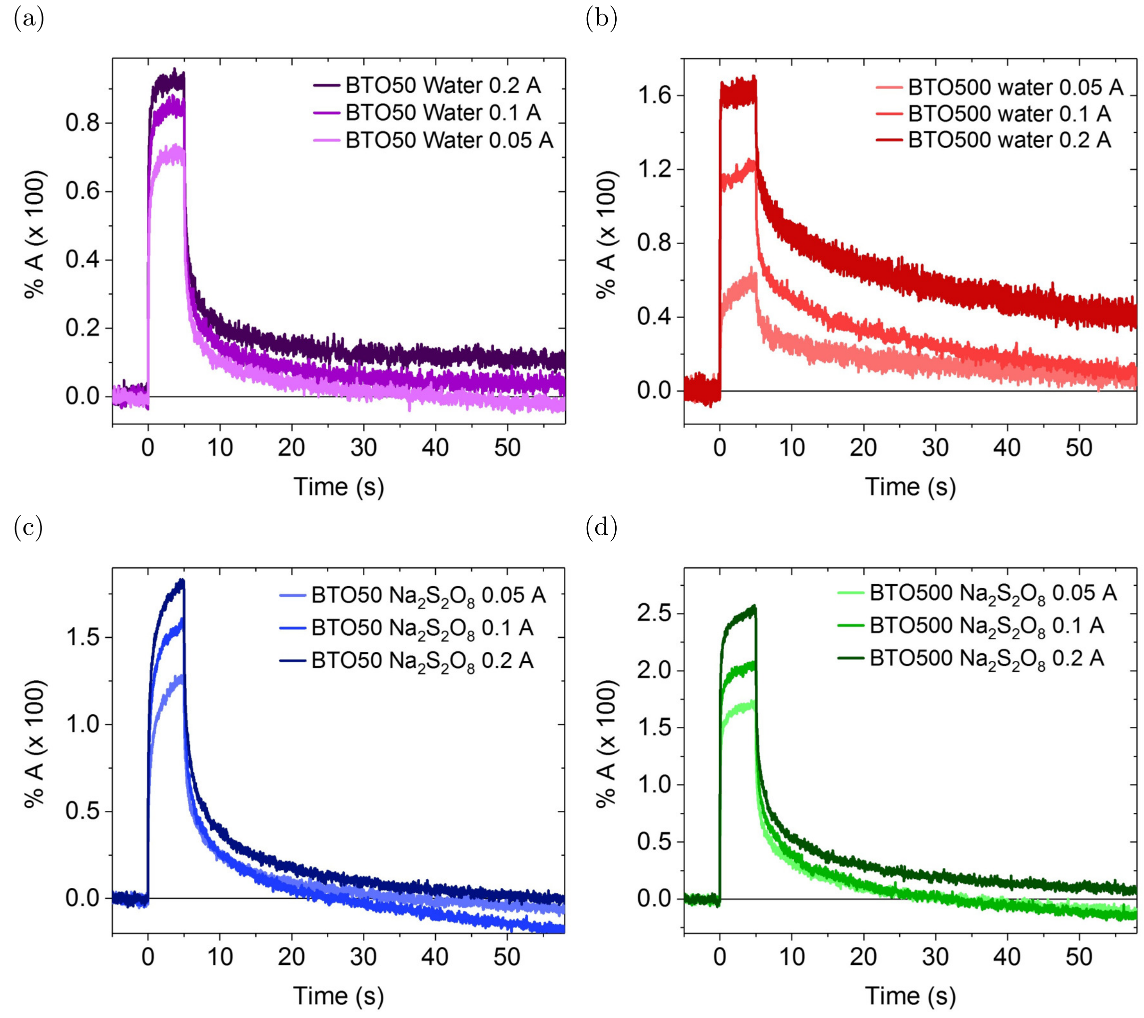

FIGURE 6.10: Photoinduced absorption signals of $BaTiO_3$ nanopowder samples as a function of 365 nm LED light intensity. (a) BTO50 in water, (b) BTO500 in water, (c) BTO50 in 0.1 M $Na_2S_2O_8$, and (d) BTO500 in $Na_2S_2O_8$. The light is switched on at 0 s and off at 5 s.

Figure 6.11(a) graphs the normalised PIA traces of BTO500 in water and $Na_2S_2O_8$ with comparable signal amplitudes. The electron scavenging effects of $Na_2S_2O_8$ means that a much lower light intensity is required to reach the same charge carrier concentration as in water. In $Na_2S_2O_8$, the signal fully decays to zero within 30 s, whereas in water the decay is significantly slower. It is possible that the long-lived 'tail' which is apparent in the absence of electron scavenger (for both BTO50 and BTO500 measurements) is due to electron absorption. The PIA spectrum was not measured in this case. The slow transients observed in water could also be caused by charge trapping effects and the differences in reactions with persulfate and water (both in terms of thermodynamic and kinetics). Reduction of persulfate is known to generate many subproducts (such as peroxide and, in some cases, superoxide), which may be more easily oxidised than water, which requires the accumulation of four holes.[33] In water, therefore, it is possible that accumulated holes are trapped and unable to react, or react extremely slowly.

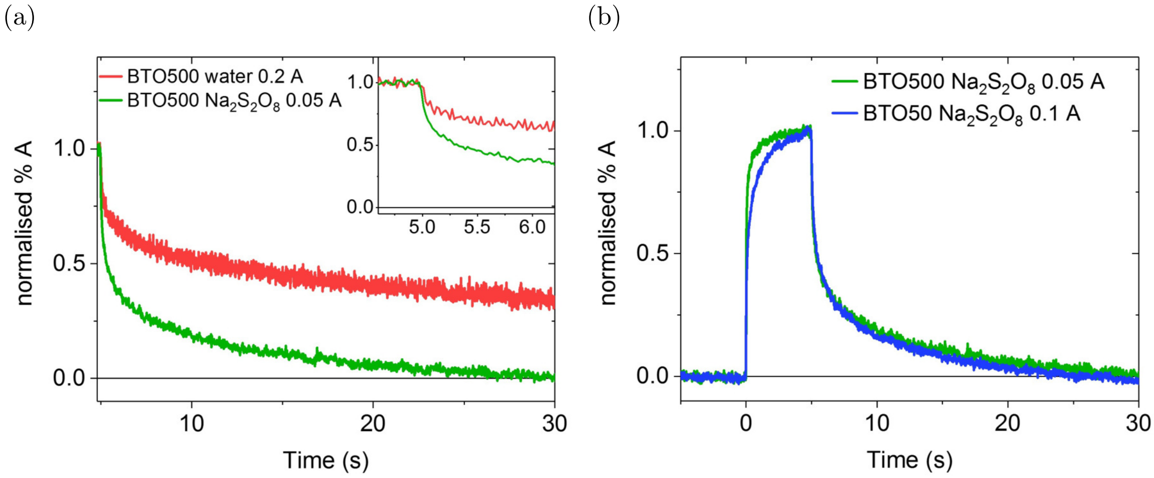

FIGURE 6.11: (a) Normalised photoinduced absorption traces of $BaTiO_3$ nanopowder sample BTO500 in water (red) and $Na_2S_2O_8$ (green) after illumination with 365 nm LED light has been ceased. Light intensities were chosen such that unnormalised signal amplitudes were comparable. The inset image shows a zoom of the traces; the light is switched off at 5 s. (b) Photoinduced absorption traces of BTO50 and BTO500 in $Na_2S_2O_8$ illuminated with 365 nm LED light (from 0–5 s), normalised at maximum $\%A$.

BTO50 vs BTO500

Figure 6.11(b) compares the normalised PIA traces of BTO50 and BTO500 in $Na_2S_2O_8$ at comparable $\%A$ values. A higher light intensity is required to reach the same hole concentration in BTO50 and BTO500. Further, despite the higher light intensity, hole accumulation in BTO50 takes significantly longer than in BTO500. Both observations are consistent with the theory that the higher degree of tetragonality in BTO500 reduces electron–hole recombination rates; equilibrium is reached more quickly in BTO500, and a higher hole concentration can be reached. Once the light is switched off, both traces display identical decays, indicating that once accumulated, holes oxidise water at the same rate on both BTO50 and BTO500. This indicates that the structure of the BTO50 and BTO500 surfaces are similar, and that the interaction with water on the surface is comparable. The observation is in contrast to literature reports which suggest that the polarisation of ferroelectric surfaces can interact with surface adsorbed species such that the energy required to break bonds is reduced.[28, 34, 35] However, these previously reported studies generally utilised single crystal samples with uniform surfaces exposed, and certain ferroelectric domains were found to enhance photochemical reactivity more than others.[35] The mixed phase and polycrystalline nature of the samples used here is likely to result in exposure of all surfaces to electrolyte, which may cause a reduction in disparity between reaction rates on BTO50 and BTO500.

6.5 Discussion

Unlike the TAS results of Chapter 5, which indicated that electron–hole recombination in cubic (non-ferroelectric) $BaTiO_3$ films is 4 orders of magnitude faster than in tetragonal (ferroelectric) $BaTiO_3$, charge carrier dynamics of BTO50 and BTO500 exhibit equivalent lifetimes on the timescales of the measurements, differing only in their amplitudes. This indicates that BTO50 contains some ferroelectric content. Since suppression of the spontaneous polarisation in nanostructured ferroelectrics is dependent on both intrinsic (free energy) and extrinsic (e.g. defects) effects, the phase of nanostructured $BaTiO_3$ is sensitive to synthesis and processing parameters, so mixed-phase samples can occur.[4] It seems probable, then, that this is the case with BTO50; although the XRD pattern indicates the sample is entirely cubic, the similarity of decay kinetics of BTO50 and BTO500 suggests that electron–hole recombination in *tetragonal* $BaTiO_3$ is in fact being monitored on µs–s timescales. The difference in amplitude, however, suggests that more recombination occurs in BTO50 than in BTO500 at sub-µs timescales. Thus, it is proposed that the higher cubic content in BTO50 results in fewer charge carriers remaining on µs–s timescales than in the tetragonal BTO500. Figure 6.12 shows a simple schematic of the proposed model of TA decay kinetics in fully tetragonal (red), fully cubic (blue) and mixed phase (purple) $BaTiO_3$ samples. In a purely tetragonal sample, such as the single crystal investigated in Chapters 4 and 5, the internal electric fields suppress recombination on both sub-µs and µs–s timescales, consistent with observations from both ultrafast and slow TAS studies reported in this thesis.[†] In a purely cubic sample, such as the thick film (cTF-BTO) investigated in Chapter 5, recombination is fast, resulting in very few charge carriers surviving until ms timescales. In a mixed-phased sample, such as the BTO50 nanopowder presented in this chapter, fast recombination occurs in the cubic phase on fs–ns timescales, with long-lived charge carriers surviving in the tetragonal portions of the samples which contain internal electric fields. If correct, this is the first known example of using time-resolved spectroscopy to observe the crystal phase of a material. It is not possible, however, to determine the quantity of each phase in the samples using these limited results. Since the XRD characterisation shows no peak splitting, it is likely that the BTO50 sample is predominantly cubic with some tetragonal content, whilst BTO500 is, given its particle diameter, likely to be predominantly tetragonal. The apparent lack of peak splitting could also be caused by the small crystallite size of BTO50, which is known to cause peak broadening.[36] The $t_{50\%}$ of TA decays in BTO500 is $\sim$ 10 ms, which is an order of magnitude shorter than of the single crystal $BaTiO_3$ (SC-BTO) measured in Chapter 4. This could be the result of some cubic content, however it may also be due to the difference in length scales between BTO500 and SC-BTO. Upon visual inspection, ferroelectric domains in SC-BTO appear to be of approximately millimetre length scales. Since the diffusion lengths of charge carriers metal oxides are typically on the order of 10^1 nm to 10^2 µm,[37–40] the majority of photogenerated charge carriers will 'feel' the effects of one domain (i.e. P_S pointing in one direction). In the nanostructured polycrystalline BTO500, on the other hand, individual particles will contain multiple ferroelectric domains, and photogenerated charge carriers are more likely to be in the vicinity of polarisation vectors lying in opposing directions. It is possible, then, that the effect of the macroscopic polarisation is lessened, resulting in shorter carrier lifetimes in BTO500 than in SC-BTO.

Reaction Rates

Since a number of charge carriers survive to µs–s timescales in BTO500, faster reaction rates should be achievable. Table 6.5 summarises the normalised rates of dye degradation and water oxidation using BTO50 and BTO500. To be able to understand the difference in reaction rates of photocatalytic degradation of RhB on $BaTiO_3$ surfaces, the reaction mechanism must be considered as well as the polarisation-induced band bending at the ferroelectric surface. It has previously been found that photodegradation of RhB proceeds primarily via a photocatalytic (PCO), rather than a photoassisted (PAO), oxidation reaction using $BaTiO_3$.[5] In other

---

[†] For simplicity, this schematic assumes bimolecular recombination with little contribution from trapped charges, as observed for hole kinetics (i.e. probe wavelengths of $\sim$ 550 nm.

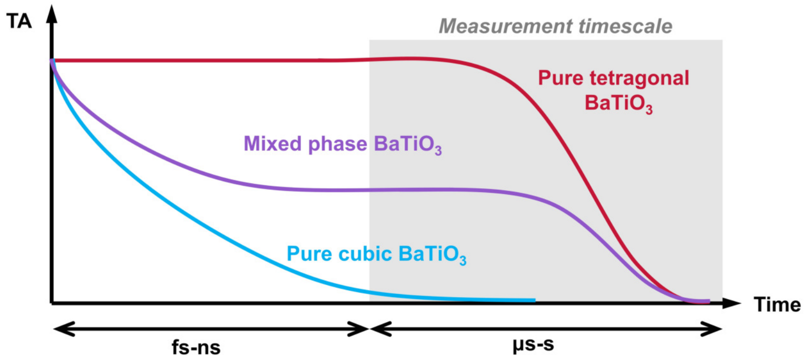

Figure 6.12: Model demonstrating the difference in transient absorption decay kinetics in pure tetragonal (red), pure cubic (blue) and mixed-phase (purple) $BaTiO_3$. The shaded area indicates the timescale of TAS measurements on BTO50 and BTO500. This model assumes recombination of free electrons and holes, and excludes effects of charge trapping.

words, charges generated within the dye itself do not significantly contribute to photodegradation; when illuminated with visible light only (i.e. using a UV filter), no decolourisation of RhB occured in a previously reported study.[5] In the predominantly tetragonal and relatively large BTO500 particles, polarisation-induced surface band bending is expected, and it has previously been suggested that this band bending, which is reported to be on the order of a few hundred meV, will dominate even when the ferroelectric is submerged in an electrolyte.[41–44] Figure 6.13 shows a schematic representation of the band diagram and degradation pathway of RhB on ferroelectric $BaTiO_3$. Since the $BaTiO_3$ powder sample is not poled, the polarisation vectors will be randomly orientated, with both $C+$ and $C-$ surfaces — and hence both upwards and downwards band bending — exposed. The cationic RhB dye molecules are likely to preferentially adsorb to $C-$ surfaces, which will have a net negative surface charge. The polarisation-induced upward band bending at these surfaces block electron transfer between the dye and the semiconductor, thus blocking the photoassisted degradation pathway (initiated by injection of electrons into $BaTiO_3$).[5]

Table 6.5: Comparison of area-normalised rates of photocatalytic dye degradation and water oxidation (using an electron scavenger) using BTO50 and BTO500 and super-bandgap (365 nm) light.

	Dye degradation (mol min^{-1} cm^{-2})	**Water oxidation** (mol O_2 h^{-1} cm^{-2})
BTO50	1.02×10^{-13}	8.28×10^{-10}
BTO500	5.53×10^{-13}	5.72×10^{-9}

The study by Cui et al. did not discuss any difference in mechanism on cubic (non-ferroelectric) $BaTiO_3$ surfaces.[5] Analogous studies of RhB decolourisation on TiO_2 nanopowders have, however, previously demonstrated that PAO degradation can occur due to the close proximity of the TiO_2 conduction band and RhB LUMO,[5, 45] but that the degradation pathway is comparable (that is, via cleavage of the chromophore).[5, 46] Thus, it is likely that the cubic (non-ferroelectric) BTO50 sample studied here, which is expected to have the same bulk energy levels as ferroelectric BTO500 but which lacks the polarisation-induced band bending, will facilitate degradation of RhB mainly by photocatalytic oxidation but also by photoassisted oxidation. As discussed in Chapter 2, band bending in non-ferroelectric semiconductors occurs when submerged in an electrolyte due to a difference in E_f and E_{redox}, and

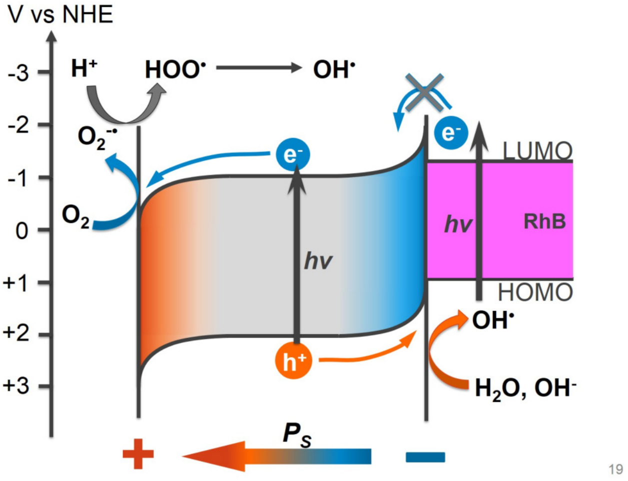

FIGURE 6.13: Schematic representation of the photocatalytic degradation of Rhodamine B dye on C- surfaces of $BaTiO_3$ nanopowders.

a space-charge layer (SCL) develops at the semiconductor/electrolyte junction.[47] Typical SCL widths of metal oxides are likely to be on the order of 10^1–10^2 nm.[48–50] In nanostructured materials, if the width of the SCL is of similar magnitude to the radial dimension, complete depletion can occur which limits the degree of band bending achievable.[51, 52] It is therefore likely that little, if any, band bending is present in BTO50. Therefore, it might be expected that, if no other factors were at play in the comparison of BTO500 (PCO plus PAO) vs BTO50 (PCO only), the rate of decolourisation would be slower on BTO500. The results presented both here and by Cui et al.[4] find that this is not the case; the area-normalised rate constant of dye degradation by BTO500 (predominantly tetragonal, ferroelectric) is $>$ 5 times higher than than by BTO50 (predominantly cubic). This indicates that the higher concentration of long-lived charge carriers in BTO500, facilitated by the internal electric field and evidenced by the TAS and PIAS measurements, outweighs any effect of PAO in BTO50.

As with the dye degradation, observed rates of water oxidation are faster on BTO500 than BTO50 (when surface area is accounted for) by a factor of ~ 7. The more pronounced difference in reaction rate could be a result of the use of $Na_2S_2O_8$ as an electron scavenger, which would enable the accumulation of more holes at the surface for oxidation. The valence band energy of $BaTiO_3$ is such that a strong thermodynamic driving force for water oxidation exists.[13] Since the polarisation vectors will be randomly oriented, not all $C-$ surfaces — which will have beneficial polarisation-induced upwards band bending — will be in contact with the electrolyte. Despite this, a significant improvement in reaction rates on BTO500 are observed, suggesting that the potential enhancement in efficiencies of solar water splitting devices using ferroelectric materials could be even greater with domain control and/or poling. Compared to $TiO_2$500, however, which is of comparable particle size, water oxidation on BTO500 is slower, indicating a higher reactivity of TiO_2 than $BaTiO_3$ despite the latter having an internal electric field. This suggests that, although ferroelectrics can significantly reduce electron–hole recombination, being able to exploit this enhanced charge is essential for improved device efficiencies. This could perhaps be achieved with the use of a co-catalyst deposited on the surface, which can lead to better performances.[53]

6.6 Further work

Although the results presented in this chapter do not provide a quantitative analysis of how the presence of an internal electric field can increase the photoactivity of a ferroelectric material, they do indicate that lower rates of electron–hole recombination attributed to polarisation-induced band bending result in higher rates of photocatalytic activity. For a more complete understanding, it would be necessary to expand this study further. For example, valuable information could be drawn from studies of $BaTiO_3$ which are confirmed to be purely cubic and non-ferroelectric to those confirmed to be purely tetragonal and ferroelectric. The study of ferroelectric nanoparticles carries many inherent complications, such as the random orientation of polarisation vectors. Although poling techniques have been demonstrated on powder samples,[54] the extent to which dipoles can be uniformly oriented is limited by the polycrystalline nature of these samples. It may therefore be useful to instead study thin films in which the orientation can be controlled, for example those synthesised by epitaxial growth.[55–57] Such samples would also allow for manipulation of the internal electric field; as well as the possibility of external poling, it has been shown that through careful selection of the substrate, strain within the ferroelectric film can be altered which affects the strength of P_S.[58] Thin films deposited on a conductive substrate would also allow for the application of an externally applied bias, as well as the use of techniques such as transient photocurrent measurements. This would enable comparison of, for example, rate law analyses of photochemical processes on cubic and tetragonal $BaTiO_3$, as has been previously reported for non-ferroelectric metal oxides.[14–16]

6.7 Conclusions

In this chapter, time-resolved spectroscopic techniques were combined with photocatalysis measurements to compare the photocatalytic activities of a (predominantly) cubic, non-ferroelectric sample of $BaTiO_3$ (BTO50) to a tetragonal, ferroelectric one (BTO500). Degradation of Rhodamine B was found to be 5 times faster on BTO500 than BTO50, and water oxidation was 7 times faster on BTO500 than BTO50 in the presence of an electron scavenger. The faster rates were attributed to the internal electric fields present in BTO500; spectroscopic results showed that electron–hole recombination on sub-µs timescales is reduced which facilitated the accumulation of a higher charge carrier concentration at the surface of the ferroelectric. Further, it was found that, once accumulated, photogenerated holes in BTO50 and BTO500 oxidise water at the same rate, confirming that the difference in rates of oxygen evolution is not the result of a difference in surface structure of the two samples but of the enhanced carrier lifetime in the ferroelectric phase. Although these studies focussed on $BaTiO_3$, it is expected that the observations made here will be applicable to other ferroelectrics materials, and to both water oxidation and proton reduction efficiencies by photocatalytic and photoelectrochemical methods. These results demonstrate that the use of ferroelectric materials could result in the achievement of significantly higher efficiencies of photocatalytic water splitting.

References

[1] Y. Inoue, I. Yoshioka, and K. Sato, “Polarization effects upon adsorptive and catalytic properties. 1. CO oxidation over Pd deposited on LiNbO3 ferroelectrics”, *J. Phys. Chem.* 209, 1148–1151 **1984**.

[2] J. Giocondi, and G. S. Rohrer, “Spatially Selective Photochemical Reduction of Silver on the Surface of Ferroelectric Barium Titanate”, *Chemistry of Materials* 13, 241–242 **2001**.

[3] S. V. Kalinin, D. A. Bonnell, T. Alvarez, X. Lei, Z. Hu, J. H. Ferris, Q. Zhang, and S. Dunn, “Atomic Polarization and Local Reactivity on Ferroelectric Surfaces: A New Route toward Complex Nanostructures”, *Nano Letters* 2, 589–593 **2002**.

[4] Y. Cui, J. Briscoe, and S. Dunn, “Effect of Ferroelectricity on Solar-Light-Driven Photocatalytic Activity of BaTiO3 - Influence on the Carrier Separation and Stern Layer Formation”, *Chemistry of Materials* 25, 4215–4223 **2013**.

[5] Y. Cui, S. M. Goldup, and S. Dunn, “Photodegradation of Rhodamine B over Ag modified ferroelectric BaTiO 3 under simulated solar light: pathways and mechanism”, *RSC Advances* 5, 30372–30379 **2015**.

[6] R. Su, Y. Shen, L. Li, D. Zhang, G. Yang, C. Gao, and Y. Yang, “Silver-modified nanosized ferroelectrics as a novel photocatalyst”, *Small* 11, 202–207 **2015**.

[7] Y. Cui, J. Briscoe, Y. Wang, N. V. Tarakina, and S. Dunn, “Enhanced Photocatalytic Activity of Heterostructured Ferroelectric BaTiO3/α-Fe2O3 and the Significance of Interface Morphology Control”, *ACS Applied Materials & Interfaces* 9, 24518–24526 **2017**.

[8] X. Huang, K. Wang, Y. Wang, B. Wang, L. Zhang, F. Gao, Y. Zhao, W. Feng, S. Zhang, and P. Liu, “Enhanced charge carrier separation to improve hydrogen production efficiency by ferroelectric spontaneous polarization electric field”, *Applied Catalysis B: Environmental* 227, 322–329 **2018**.

[9] F. Yen, H. Hsiang, and Y. Chang, “Cubic to tetragonal phase transformation of ultrafine BaTiO3 crystallites at room temperature”, *Japanese Journal of Applied Physics* 34, 6149–6155 **1995**.

[10] B. Begg, E. Vance, and J. Nowotny, “Effect of Particle Size on the Room Temperature Crystal Structure of Barium Titanate”, *Journal of the American Ceramic Society* 77, 3186–3192 **1994**.

[11] M. H. Frey, and D. A. Payne, “Grain-size effect on structure and phase transformations for barium titanate.”, *Physical review. B, Condensed matter* 54, 3158–3168 **1996**.

[12] N. Nuraje, and K. Su, “Perovskite ferroelectric nanomaterials”, *Nanoscale* 5, 8752 **2013**.

[13] J.-i. Fujisawa, T. Eda, and M. Hanaya, “Comparative study of conduction-band and valence-band edges of TiO 2 , SrTiO 3 , and BaTiO 3 by ionization potential measurements”, *Chemical Physics Letters* 685, 23–26 **2017**.

[14] A. Kafizas, Y. Ma, E. Pastor, S. R. Pendlebury, C. Mesa, L. Francàs, F. Le Formal, N. Noor, M. Ling, C. Sotelo-Vazquez, C. J. Carmalt, I. P. Parkin, and J. R. Durrant, “Water Oxidation Kinetics of Accumulated Holes on the Surface of a TiO2 Photoanode: A Rate Law Analysis”, *ACS Catalysis* 7, 4896–4903 **2017**.

[15] C. A. Mesa, A. Kafizas, L. Francàs, S. R. Pendlebury, E. Pastor, Y. Ma, F. Le Formal, M. T. Mayer, M. Grätzel, and J. R. Durrant, “Kinetics of Photoelectrochemical Oxidation of Methanol on Hematite Photoanodes”, *Journal of the American Chemical Society* 139, 11537–11543 **2017**.

[16] E. Pastor, F. Le Formal, M. T. Mayer, S. D. Tilley, L. Francàs, C. A. Mesa, M. Grätzel, and J. R. Durrant, “Spectroelectrochemical analysis of the mechanism of (photo)electrochemical hydrogen evolution at a catalytic interface”, *Nature Communications* 8 **2017**.

[17] P. Kubelka, “New Contributions to the Optics of Intensely Light-Scattering Materials Part II: Nonhomogeneous Layers*”, *Journal of the Optical Society of America* 44, 330 **1954**.

[18] J. Tauc, “Optical properties and electronic structure of amorphous Ge and Si”, *Materials Research Bulletin* 3, 37–46 **1968**.

[19] G. A. Cox, G. G. Roberts, and R. H. Tredgold, “The optical absorption edge of barium titanate”, *British Journal of Applied Physics* 17, 743–745 **1966**.

[20] K. Suzuki, and K. Kijima, “Optical Band Gap of Barium Titanate Nanoparticles Prepared by RF-plasma Chemical Vapor Deposition”, *Japanese Journal of Applied Physics* 44, 2081–2082 **2005**.

[21] K. Uchino, E. Sadanaga, and T. Hirose, “Dependence of the crystal structure on particle size in barium titanate”, *Journal of the American Ceramic Society* 72, 1555–1558 **1989**.

[22] W. J. Merz, “The electric and optical behavior of BaTiO3 single-domain crystals”, *Physical Review* 76, 1221–1225 **1949**.

[23] G. H. Kwei, a. C. Lawson, S. J. L. Billinge, and S. W. Cheong, “Structures of the ferroelectric phases of barium titanate”, *The Journal of Physical Chemistry* 97, 2368–2377 **1993**.

[24] T. Bastow, and H. Whitfield, “137Ba and 47,49Ti NMR: electric field gradients in the non-cubic phases of BaTiO3”, *Solid State Communications* 117, 483–488 **2001**.

[25] J. Tang, J. R. Durrant, and D. R. Klug, “Mechanism of Photocatalytic Water Splitting in TiO 2 . Reaction of Water with Photoholes, Importance of Charge Carrier Dynamics, and Evidence for Four-Hole Chemistry”, *Journal of the American Chemical Society* 130, 13885–13891 **2008**.

[26] X. Wang, A. Kafizas, X. Li, S. J. Moniz, P. J. Reardon, J. Tang, I. P. Parkin, and J. R. Durrant, “Transient absorption spectroscopy of anatase and rutile: The impact of morphology and phase on photocatalytic activity”, *Journal of Physical Chemistry C* 119, 10439–10447 **2015**.

[27] J. Nelson, S. Haque, D. Klug, and J. R. Durrant, “Trap-limited recombination in dye-sensitized nanocrystalline metal oxide electrodes”, *Physical Review B* 63, 205321 **2001**.

[28] M. Stock, and S. Dunn, “Linbo 3 - A new material for artificial photosynthesis”, *IEEE Transactions on Ultrasonics, Ferroelectrics and Frequency Control* 58, 1988–1993 **2011**.

[29] J. Herrmann, “Heterogeneous photocatalysis: fundamentals and applications to the removal of various types of aqueous pollutants”, *Catalysis Today* 53, 115–129 **1999**.

[30] M. Stock, and S. Dunn, “Influence of the ferroelectric nature of lithium niobate to drive photocatalytic dye decolorization under artificial solar light”, *Journal of Physical Chemistry C* 116, 20854–20859 **2012**.

[31] Y. Inoue, M. Okamura, and K. Sato, “A thin-film semiconducting titanium dioxide combined with ferroelectrics for photoassisted water decomposition”, *The Journal of Physical Chemistry* 89, 5184–5187 **1985**.

[32] F. Le Formal, E. Pastor, S. D. Tilley, C. A. Mesa, S. R. Pendlebury, M. Grätzel, and J. R. Durrant, “Rate law analysis of water oxidation on a hematite surface.”, *Journal of the American Chemical Society* 137, 6629–37 **2015**.

[33] P. Scott, R. Menzel, R. Mullholand, and R. White, “Technical information”, *Building Research & Information* 22, 141–142 **1994**.

[34] A. L. Cabrera, F. Vargas, and R. A. Zarate, “Adsorption of carbon dioxide by barium titanate: Evidence of adsorption process mediated by a dipole-dipole interaction”, *Journal of Physics and Chemistry of Solids* 55, 1303–1307 **1994**.

[35] M. H. Zhao, D. A. Bonnell, and J. M. Vohs, “Effect of ferroelectric polarization on the adsorption and reaction of ethanol on BaTiO3”, *Surface Science* 602, 2849–2855 **2008**.

[36] J. I. Langford, and A. J. C. Wilson, “Scherrer after sixty years: A survey and some new results in the determination of crystallite size”, *Journal of Applied Crystallography* 11, 102–113 **1978**.

[37] M. P. Dare-Edwards, J. B. Goodenough, A. Hamnett, and P. R. Trevellick, “Electrochemistry and photoelectrochemistry of iron(III) oxide”, *Journal of the Chemical Society, Faraday Transactions 1: Physical Chemistry in Condensed Phases* 79, 2027 **1983**.

[38] W. H. Leng, P. R. F. Barnes, M. Juozapavicius, B. C. O’Regan, and J. R. Durrant, “Electron Diffusion Length in Mesoporous Nanocrystalline TiO2 Photoelectrodes during Water Oxidation”, *The Journal of Physical Chemistry Letters* 1, 967–972 **2010**.

[39] F. F. Abdi, T. J. Savenije, M. M. May, B. Dam, and R. Van De Krol, “The origin of slow carrier transport in BiVO4 thin film photoanodes: A time-resolved microwave conductivity study”, *Journal of Physical Chemistry Letters* 4, 2752–2757 **2013**.

[40] R. A. Pala, A. J. Leenheer, M. Lichterman, H. A. Atwater, and N. S. Lewis, “Measurement of minority-carrier diffusion lengths using wedge-shaped semiconductor photoelectrodes”, *Energy Environ. Sci.* 7, 3424–3430 **2014**.

[41] S. Dunn, and D. Tiwari, “Influence of ferroelectricity on the photoelectric effect of LiNbO3”, *Applied Physics Letters* 93, 092905–1 **2008**.

[42] D. Tiwari, and S. Dunn, “Influence of annealing on the photochemical deposition of silver onto PZT thin films under UV irradiation”, *Journal of the European Ceramic Society* 29, 2799–2805 **2009**.

[43] A. Höfer, M. Fechner, K. Duncker, M. Hölzer, I. Mertig, and W. Widdra, “Persistence of Surface Domain Structures for a Bulk Ferroelectric above TC”, *Physical Review Letters* 108, 087602 **2012**.

[44] N. G. Apostol, L. E. Stoflea, G. A. Lungu, C. A. Tache, D. G. Popescu, L. Pintilie, and C. M. Teodorescu, “Band bending at free Pb(Zr,Ti)O3 surfaces analyzed by X-ray photoelectron spectroscopy”, *Materials Science and Engineering B: Solid-State Materials for Advanced Technology* 178, 1317–1322 **2013**.

[45] J. Zhao, T. Wu, K. Wu, K. Oikawa, H. Hidaka, and N. Serpone, “Photoassisted Degradation of Dye Pollutants. 3. Degradation of the Cationic Dye Rhodamine B in Aqueous Anionic Surfactant/TiO 2 Dispersions under Visible Light Irradiation: Evidence for the Need of Substrate Adsorption on TiO 2 Particles”, *Environmental Science & Technology* 32, 2394–2400 **1998**.

[46] Q. Wang, C. Chen, D. Zhao, W. Ma, and J. Zhao, “Change of Adsorption Modes of Dyes on Fluorinated TiO 2 and Its Effect on Photocatalytic Degradation of Dyes under Visible Irradiation”, *Langmuir* 24, 7338–7345 **2008**.

[47] M. Grätzel, “Photoelectrochemical cells”, *Nature* 414, 338–344 **2001**.

[48] Y. Ma, S. R. Pendlebury, A. Reynal, F. Le Formal, and J. R. Durrant, “Dynamics of photogenerated holes in undoped BiVO4 photoanodes for solar water oxidation”, *Chemical Science* 5, 2964 **2014**.

[49] L. Li, P. A. Salvador, and G. S. Rohrer, “Photocatalysts with internal electric fields.”, *Nanoscale* 6, 24–42 **2014**.

[50] A. Bhardwaj, N. V. Burbure, and G. S. Rohrer, “Enhanced photochemical reactivity at the ferroelectric phase transition in Ba1-xSrxTiO3”, *Journal of the American Ceramic Society* 93, 4129–4134 **2010**.

[51] M. Law, L. E. Greene, J. C. Johnson, R. Saykally, and P. Yang, “Nanowire dye-sensitized solar cells”, *Nature Materials* 4, 455–459 **2005**.

[52] F. M. Pesci, G. Wang, D. R. Klug, Y. Li, and A. J. Cowan, “Efficient Suppression of Electron-Hole Recombination in Oxygen-Deficient Hydrogen-Treated TiO2 Nanowires for Photoelectrochemical Water Splitting.”, *The journal of physical chemistry. C, Nanomaterials and interfaces* 117, 25837–25844 **2013**.

[53] S. J. a. Moniz, S. a. Shevlin, D. J. Martin, Z.-X. Guo, and J. Tang, “Visible-light driven heterojunction photocatalysts for water splitting – a critical review”, *Energy & Environmental Science* 8, 731–759 **2015**.

[54] S. Park, C. W. Lee, M.-G. Kang, S. Kim, H. J. Kim, J. E. Kwon, S. Y. Park, C.-Y. Kang, K. S. Hong, and K. T. Nam, “A ferroelectric photocatalyst for enhancing hydrogen evolution: polarized particulate suspension”, *Physical Chemistry Chemical Physics* 16, 10408 **2014**.

[55] C. Daumont, W. Ren, I. C. Infante, S. Lisenkov, J. Allibe, C. Carrétéro, S. Fusil, E. Jacquet, T. Bouvet, F. Bouamrane, S. Prosandeev, G. Geneste, B. Dkhil, L. Bellaiche, A. Barthélémy, and M. Bibes, "Strain dependence of polarization and piezoelectric response in epitaxial BiFeO3 thin films", *Journal of Physics: Condensed Matter* 24, 162202 **2012**.

[56] W. Ji, K. Yao, Y. F. Lim, Y. C. Liang, and A. Suwardi, "Epitaxial ferroelectric BiFeO3 thin films for unassisted photocatalytic water splitting", *Applied Physics Letters* 103, 1–5 **2013**.

[57] I. Pintilie, C. M. Teodorescu, C. Ghica, C. Chirila, A. G. Boni, L. Hrib, I. Pasuk, R. Negrea, N. Apostol, and L. Pintilie, "Polarization-control of the potential barrier at the electrode interfaces in epitaxial ferroelectric thin films", *ACS Applied Materials and Interfaces* 6, 2929–2939 **2014**.

[58] J. Lyu, I. Fina, R. Solanas, J. Fontcuberta, and F. Sánchez, "Tailoring Lattice Strain and Ferroelectric Polarization of Epitaxial BaTiO3Thin Films on Si(001)", *Scientific Reports* 8, 1–10 **2018**.

Chapter 7

Ferro-/non-ferro-electric $BaTiO_3/\alpha$-Fe_2O_3 heterostructures

> *"But we are changing the world! We're changing the way people think about things."*
>
> James Durrant

7.1 Introduction

In the previous chapters, it was shown that electron–hole recombination rates in ferroelectric $BaTiO_3$ are significantly lower than many of the metal oxides currently being investigated for solar-driven water splitting (Chapter 4), and that this can be attributed to the presence of an internal electric field (Chapter 5). Evidence was also presented which suggested that, as a result of this, ferroelectrics may exhibit higher catalytic activity than non-ferroelectrics (Chapter 6). It seems entirely possible, then, that inclusion of ferroelectric materials in solar energy conversion devices could lead to greater efficiencies.

The wide bandgap of $BaTiO_3$ (and most other ferroelectrics) and slow water oxidation kinetics exhibited in Chapter 6 mean that, despite the remarkably long carrier lifetimes induced by the ferroelectric polarisation, this material is highly unlikely to be used — on its own — for water oxidation. However, there is compelling evidence that ferroelectric substrates could be used to enhance the properties of a non-ferroelectric thin over-layer, as discussed in Chapter 2.[1–3] Previously reported studies have demonstrated, empirically, that the photochemistry of a non-ferroelectric film can mimic the domain pattern of a ferroelectric substrate, provided the layer is very thin (on the order of 10^1 nm).[2, 4–9] The benefit of such a heterostructure is the potential ability to manipulate the behaviour of charge carrier dynamics in a light-absorbing, non-ferroelectric semiconductor which shows promise as a water splitting material but which suffers from fast electron–hole recombination. Hematite, for example, is one of the most studied materials for water oxidation due to its relatively low bandgap ($\sim$ 1.9–2.2 eV), high stability and abundance, but, as discussed earlier in this thesis (Chapter 2) its fast recombination means that its performance as a water oxidation photocatalyst is severely limited.[10–12] A recent study demonstrated improved dye degradation by $BaTiO_3/\alpha$-Fe_2O_3 heterostructures when compared to bare α-Fe_2O_3 or $BaTiO_3$ nanoparticles.[13] This performance was more pronounced when the $BaTiO_3$ was of tetragonal (ferroelectric) crystal phase than cubic (non-ferroelectric) phase. Interestingly, however, the increased performance was not attributed to improved charge carrier dynamics in α-Fe_2O_3, but to enhanced charge separation at the interface due to the polarisation-induced upward band bending at $C+$ faces in the $BaTiO_3$. No spectroscopic measurements of charge carrier dynamics were reported in this study, however.

Currently, little spectroscopic evidence of charge carrier dynamics being influenced by substrate polarisation currently exists in the literature, although computational studies have predicted domain-specific reactivity on coated ferroelectric surfaces as a result of such an effect.[14, 15] The first spectroscopic study showing internal electric fields influencing recombination rates in a non-ferroelectric was conducted on hybrid organic/inorganic solar cells incorporating ZnO, a piezoelectric material, and P3HT.[16] It was found that, under mechanical stress (acoustic vibrations), efficiency enhancements of up to 45 % were achieved, correlated with a three-fold increase in carrier lifetime facilitated the field generated by the ZnO, indicating the potential advantage of internal electric fields. In this chapter, the effect of substrate polarisation on photogenerated carrier lifetimes in thin films of α-Fe_2O_3 is explored. Using transient absorption spectroscopy (TAS), electron–hole recombination rates are measured in α-Fe_2O_3 deposited on a ferroelectric single crystal $BaTiO_3$ substrate, and compared to those in α-Fe_2O_3 on a single crystal TiO_2 substrate. The smaller bandgap of α-Fe_2O_3 means that it can be selectively excited by choosing an excitation energy lower than the bandgap of $BaTiO_3$. Thus, it can be assessed if carrier dynamics in the non-ferroelectric semiconductor are influenced by the polarisation of the substrate. A further reason for choosing a $BaTiO_3/\alpha$-Fe_2O_3 heterostructure is the type I, or ‘straddling gap,’ junction formed, as illustrated in Figure 7.1. The conduction band edges of $BaTiO_3$ and α-Fe_2O_3 are reported to lie at approximately -0.3 and $+0.4$ V vs RHE, respectively, and valence bands at approximately $+2.8$ and $+2.5$ V vs RHE.[17, 18] Thus, photogenerated charge carriers in α-Fe_2O_3 should largely remain on the lower bandgap material. Charge transfer onto $BaTiO_3$ should therefore be minimal, allowing the effect of polarisation on carrier dynamics to be isolated from improvements due to charge transfer. As with previous chapters, TiO_2 provides a good control because of its conduction and valence band energies, which lie in close proximity to those of $BaTiO_3$.[17] By comparing the carrier dynamics of α-Fe_2O_3 thin films deposited on $BaTiO_3$ to those deposited on TiO_2, any differences induced by substrate ferroelectricity can be explored.

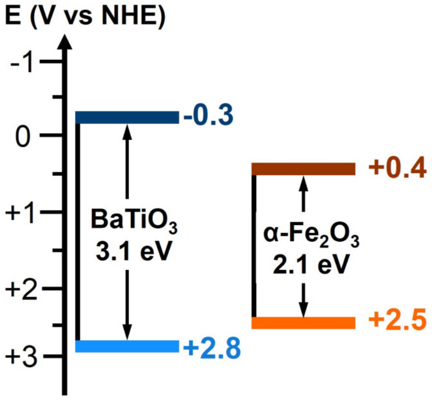

FIGURE 7.1: Band diagrams of $BaTiO_3$ and α-Fe_2O_3. The effects of polarisation-induced band bending are not considered in this scheme.

7.2 Experimental

Single crystals of $BaTiO_3$ and TiO_2 (investigated in Chapters 4 and 5) were purchased from MTI Corporation and used, as received, as substrates. Deposition of α-$Fe_2O_3$was conducted by Dr Ludmilla Steier using the facilities at École polytechnique fédérale de Lausanne, Switzerland.

Ultrasonic spray pyrolysis (USP) was used to deposit α-Fe_2O_3 (thickness 12 nm), as reported previously, onto the $BaTiO_3$ and TiO_2 substrates.[19] A 50 nm hematite film was also deposited on a separate $BaTiO_3$ substrate to investigate the depth to which P_S can propagate through the non-ferroelectric. Further details are given in Chapter 3.

TAS measurements were performed in transmission mode on a timescale of µs–s using the set-up described in Chapter 3. Selective excitation of the α-Fe_2O_3 thin film was facilitated by choosing a pump wavelength of 532 nm (2.3 eV, $0.9\,\mathrm{mJ\,cm^{-2}}$). A pulse rate of 0.4 Hz was chosen to allow samples to return to ground state prior to the next excitation pulse. Each measurement was obtained using a monochromatic probe beam over the range 600–950 nm. Samples were placed in sealed quartz cuvettes and purged with Ar prior to measurements.

7.3 Results

7.3.1 Steady-state absorption

Figure 7.2 shows the UV–vis absorption spectra of the bare substrates and thin film α-Fe_2O_3. Thin film spectra were obtained using the appropriate substrates as the background. It should be noted that the individual $BaTiO_3$ single crystals obtained from MTI Corp. had, by eye, had slight differences in their appearances; some had a slight yellowish tint, indicating different impurity/defect levels, and all had different ferroelectric domain structures. Thus, slight variations in absorption between the bare substrates and those coated with α-Fe_2O_3 may occur, although these are expected to be small. Traces were corrected for any scattering effects by subtracting a linear baseline.

Spectra are in good agreement with previously reported absorption data for thin α-Fe_2O_3 films and indicate that, by using an excitation wavelength of 532 nm, the α-Fe_2O_3 layers should be selectively excited.[20] The absorption coefficient of a film, $\alpha(\lambda)$, can be obtained from the absorption spectrum using the Beer–Lambert law:

$$\alpha(\lambda) = \frac{Abs(\lambda)}{l} \tag{7.1}$$

where l is the film length in metres. From this, the optical penetration depth of 532 nm light ($1/\alpha$) can be calculated. It is notable, however, that the absorbance values of 12 nm thick α-Fe_2O_3 layers on $BaTiO_3$ and TiO_2 substrates are not comparable. This could suggest that the thicknesses differ, which may be due to a difference in growth rate on the two substrates (the growth rate was measured on Si substrates). Without further characterisation, it is not currently possible to state accurate film thicknesses. Thus, obtained values of the light penetration depth, listed in Table 7.1, can only be treated as approximations. As expected,

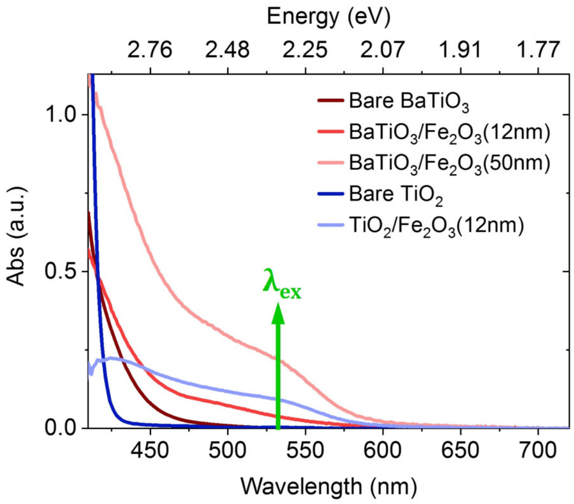

FIGURE 7.2: Steady-state absorption spectra of bare $BaTiO_3$ and TiO_2 substrates, and of the USP deposited α-Fe_2O_3 thin films. Spectra have been corrected for scattering effects by subtraction of a linear baseline. 532 nm (the wavelength used for transient absorption measurements) is below the bandgap of the substrates, but the α-Fe_2O_3 thin films absorb.

the obtained range of optical depths is large. However, it is reasonable to assume that the 532 nm light used in transient absorption measurements will not be fully absorbed by the α-Fe_2O_3 thin film, and that a significant portion will be transmitted through to the substrates.

TABLE 7.1: Absorption coefficients (α) and optical penetration depths (α^{-1}) at 532 nm of α-Fe_2O_3 thin films, obtained from steady-state absorption spectra.

Sample	Abs	α (m^{-1})	α^{-1} (nm)
$BaTiO_3/\alpha$-Fe_2O_3(12nm)	0.04	3.3×10^6	300
$BaTiO_3/\alpha$-Fe_2O_3(50nm)	0.220	4.4×10^6	227
TiO_2/α-Fe_2O_3(12nm)	0.093	7.5×10^6	133

7.3.2 Transient absorption spectroscopy

Figure 7.3 shows the transient absorption decay kinetics of α-Fe_2O_3 thin films on (a–b) $BaTiO_3$ and (c) TiO_2 substrates, following selective excitation of the α-Fe_2O_3 by a 532 nm laser pulse. To determine whether TA absorption could be due to the $BaTiO_3$, measurements were also performed of the bare $BaTiO_3$ using a wavelength of 532 nm (Figure 7.3(d)).

When deposited on the TiO_2 substrates, TA decay rates are fast with $t_{50\%}$ values of $\sim 10\,\mu s$. This is comparable to the unbiased α-Fe_2O_3 reported in Chapter 5 as well as elsewhere in the literature.[21] No TA signal could be detected in the bare TiO_2 single crystal using an excitation wavelength of 532 nm, consistent with the UV–vis absorption spectrum which indicates no steady-state absorption. Thus, the TA signals from the TiO_2/α-Fe_2O_3 heterostructure can be attributed to electron–hole recombination in the α-Fe_2O_3 thin film.

The $t_{50\%}$ of decays from the 12 nm thick α-Fe_2O_3 on $BaTiO_3$ are difficult to determine due to the small optical signal and low-frequency noise which appears from $\sim$ 500 ms, however appear to be $>$ 100 ms. Decays from the thicker 50 nm α-Fe_2O_3 film on $BaTiO_3$ are faster

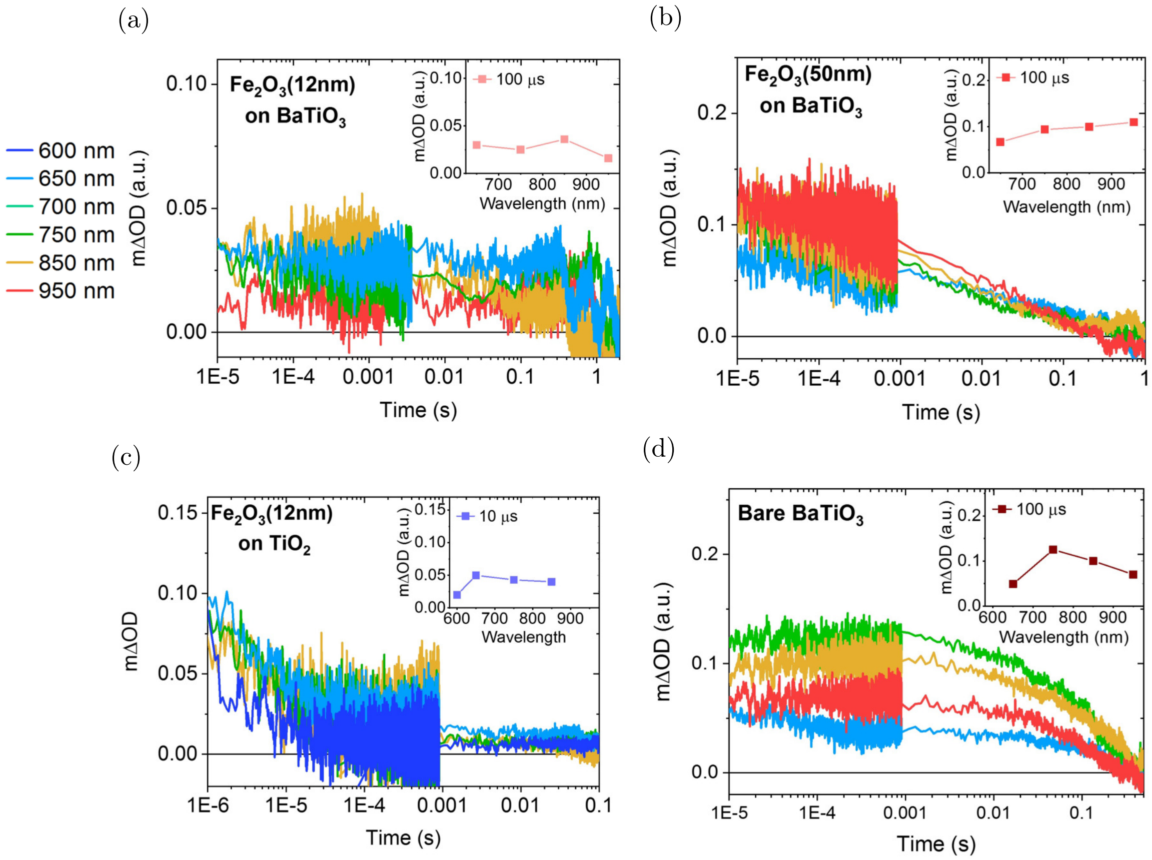

Figure 7.3: TA kinetics of (a) 12 nm α-Fe_2O_3 on $BaTiO_3$, (b) 50 nm α-Fe_2O_3 on $BaTiO_3$, (c) α-Fe_2O_3 on TiO_2 and (d) bare $BaTiO_3$ following 532 nm excitation ($0.9\,\mathrm{mJ\,cm^{-2}}$). Inset images show TA spectra 100 µs after laser excitation. All measurements were conducted under inert atmosphere (Ar).

than the 12 nm film, but still significantly slower than when the film is on the non-ferroelectric substrate, with $t_{50\%} \approx 4$ ms.

Although the UV–vis spectrum (Figure 7.2) of the $BaTiO_3$ suggests that no absorption occurs at 532 nm, Figure 7.3(d) shows that there are clear TA signals which resemble those obtained using an excitation wavelength of 355 nm (presented in Chapter 4). As mentioned, separate samples were used for measurements on bare and coated substrates, thus the impurity levels may cause differences in steady-state absorption. As with the super-bandgap excitation, decays have $t_{50\%}$ values of $\sim$ 100 ms. Thus, the origin of the TA signals from the $BaTiO_3/\alpha$-Fe_2O_3 heterostructures is unclear. Since the penetration depth of 532 nm light through α-Fe_2O_3 is » 50 nm, significant absorption by $BaTiO_3$ is possible in both $BaTiO_3/\alpha$-Fe_2O_3 samples. However, neither the spectra nor the kinetics entirely match those observed in the bare $BaTiO_3$, which suggests that a different excited state species is being monitored. The flatness of the spectra are comparable to the spectrum of α-Fe_2O_3 deposited on the non-ferroelectric TiO_2, and the signal amplitude is significantly lower than observed in the bare $BaTiO_3$. If the TA signals were partially due to the substrate, it would be expected (since the majority of the light is transmitted through the α-Fe_2O_3 film) that higher amplitude signals would be obtained. It is possible, therefore, that these signals instead arise from charge carriers in α-Fe_2O_3 which are influenced by the spontaneous polarisation in $BaTiO_3$, consistent with previous studies in the literature.[2, 4–9] The shorter lifetimes observed in the thicker film may be due to a reduced influence further away from the ferroelectric/non-ferroelectric interface, which agrees with previous reports that the ferroelectric polarisation can only propagate to short distances through a non-ferroelectric top layer.[4–6] Exactly how far the internal field can penetrate is not well understood; it is likely to vary between materials and with variables such as morphology, crystallinity and defects/impurities, all of which can affect the level of internal and external screening which occurs in the ferroelectric, however it is generally reported that the effect disappears beyond a few tens of nm.[4–6]

7.4 Discussion

At present, the origin of the TA signals from $BaTiO_3/\alpha$-Fe_2O_3 heterostructures is unclear. The unexpected TA signal from the $BaTiO_3$ using sub-bandgap excitation suggests that, since the penetration depth of light is greater than the film thickness, some contribution to the transient absorption signal from the substrate will occur. However, the observed charge carrier dynamics of the $BaTiO_3/\alpha$-Fe_2O_3 samples differ from those of the bare substrate. Two possible ways to interpret this data are considered.

The first assumes excitation of both the α-Fe_2O_3 thin film and the $BaTiO_3$ substrate, and that both contribute to the TA signal. Using this interpretation, the difference in kinetics between signals from two $BaTiO_3/\alpha$-Fe_2O_3 samples can explained by considering that, with a thinner film, the kinetics more closely resemble that of the ferroelectric substrate (that is, they are long lived with lifetimes of at least 100 ms), whilst a thicker film results in kinetics which decay with a rate somewhere between $BaTiO_3$ and α-Fe_2O_3. However, this does not explain the difference in the spectra of the $BaTiO_3/\alpha$-Fe_2O_3 samples, which is comparable to that of the TiO_2-supported α-Fe_2O_3, and the bare $BaTiO_3$. Nor does it explain the significant difference in signal amplitude, given that $\sim$ 80 % of the excitation beam is transmitted through to the substrate.

A second interpretation attributes the TA signals of the heterostructures to the α-Fe_2O_3 thin films only. This theory builds on previous reports in the literature which have found that the spontaneous polarisation of a ferroelectric substrate can influence the behaviour of photogenerated electrons and holes in a non-ferroelectric thin film. Typically, carrier lifetimes in unbiased α-Fe_2O_3 films are on the order of 10 µs, with longer lifetimes achieved under applied bias.[21] If the signals observed here do indeed arise from the α-Fe_2O_3, then the long lifetimes can be attributed to propagation of the ferroelectric polarisation through the thin film, resulting in enhanced spatial separation of carriers and recombination rates orders of magnitude lower than in α-Fe_2O_3 on a non-ferroelectric substrate. In other words, using a ferroelectric substrate can result in α-Fe_2O_3 behaving as if under applied bias, but without the requirement of an electrical energy input. Using this interpretation, the difference in decay lifetimes between the 12 and 50 nm films can be attributed to the fact that the ability of P_S to influence the carrier dynamics diminishes as the film thickness increases.

The preliminary results reported herein are clearly limited, and thus currently there is no certainty as to which, if either, interpretation is accurate. However, considering the results in the context of the existing body of literature — which indicates carrier dynamics of thin films are influenced by ferroelectric substrates — further research on these heterostructures seems highly worthwhile. The complication of TA signals from the substrate could be overcome by changing the excitation wavelength to one not absorbed by $BaTiO_3$ or by obtaining a single crystal with fewer defects which does not absorb below the bandgap. In this study, the effect of polarisation-induced band bending on charge transfer from α-Fe_2O_3 to TiO_2 has not been considered. The band diagram illustrated in Figure 7.1 uses values of the conduction and valence band energies reported in the literature, and therefore is not exact. Given the very small difference in valence bands energies between $BaTiO_3$ and α-Fe_2O_3, any variation could have significant effects on the movement of photogenerated holes from the film to the substrate. From the spectroscopic measurements carried out it is not possible to draw any conclusions regarding the role of charge transfer.

Knowledge of the extent to which carrier dynamics of light-absorbing materials can be advantageously influenced by substrate polarisation is essential for designing ferroelectric/non-ferroelectric heterostructures which have the potential to exceed current device efficiencies. Given the significant reduction in electron–hole recombination (potentially) observed here for α-Fe_2O_3, such heterostructures might be particularly beneficial for solar water-splitting, in which applied biases are currently required to achieve carrier lifetimes long enough to carry out redox reactions. However, it is expected that improved understanding of this phenomenon could also be used to enhance efficiencies of across both solar fuels and photovoltaic fields.

7.5 Conclusions

Preliminary transient absorption measurements of $BaTiO_3$/α-Fe_2O_3 heterostructures suggested that electron–hole recombination in α-Fe_2O_3 thin films could be reduced by several orders of magnitude due to the influence of the ferroelectric substrate. When deposited on TiO_2 single crystals, α-Fe_2O_3 displays characteristic fast recombination ($t_{50\%}$), which appears to be slowed significantly when deposited on $BaTiO_3$ single crystals ($t_{50\%} > 100$ ms). Additional studies are required to fully characterise spectroscopic signals, but these promising results suggest that further research will be valuable for both solar fuels and solar photovoltaic fields.

References

[1] Y. Inoue, K. Sato, and S. Suzuki, “Polarization Effects upon Adsorptive and Catalytic Properties. 2. Surface Electrical Conductivity of NiO Deposited on LiNbO3, and Its Changes upon Gas Adsorption”, *J. Phys. Chem.* 89, 2827–2831 **1985**.

[2] L. Li, G. S. Rohrer, and P. A. Salvador, “Heterostructured Ceramic Powders for Photocatalytic Hydrogen Production: Nanostructured TiO2 Shells Surrounding Microcrystalline (Ba,Sr)TiO3 Cores”, *Journal of the American Ceramic Society* 95, edited by E. Dickey, 1414–1420 **2012**.

[3] Y. Zhang, A. M. Schultz, P. a. Salvador, and G. S. Rohrer, “Spatially selective visible light photocatalytic activity of TiO2/BiFeO3 heterostructures”, *Journal of Materials Chemistry* 21, 4168 **2011**.

[4] Y. Inoue, M. Okamura, and K. Sato, “A thin-film semiconducting titanium dioxide combined with ferroelectrics for photoassisted water decomposition”, *The Journal of Physical Chemistry* 89, 5184–5187 **1985**.

[5] N. V. Burbure, P. A. Salvador, and G. S. Rohrer, “Influence of Dipolar Fields on the Photochemical Reactivity of Thin Titania Films on BaTiO3 Substrates”, *Journal of the American Ceramic Society* 89, 2943–2945 **2006**.

[6] N. V. Burbure, P. A. Salvador, and G. S. Rohrer, “Photochemical Reactivity of Titania Films on BaTiO 3 Substrates: Origin of Spatial Selectivity”, *Chemistry of Materials* 22, 5831–5837 **2010**.

[7] W. Yang, Y. Yu, M. B. Starr, X. Yin, Z. Li, A. Kvit, S. Wang, P. Zhao, and X. Wang, “Ferroelectric Polarization-Enhanced Photoelectrochemical Water Splitting in TiO 2 –BaTiO 3 Core–Shell Nanowire Photoanodes ”, *Nano Letters* 15, 7574–7580 **2015**.

[8] L. Li, Y. Zhang, A. M. Schultz, X. Liu, P. A. Salvador, and G. S. Rohrer, “Visible light photochemical activity of heterostructured PbTiO3–TiO2 core–shell particles”, *Catalysis Science & Technology* 2, 1945 **2012**.

[9] S. Li, J. Zhang, M. G. Kibria, Z. Mi, M. Chaker, D. Ma, R. Nechache, and F. Rosei, “Remarkably enhanced photocatalytic activity of laser ablated Au nanoparticle decorated BiFeO3 nanowires under visible-light”, *Chemical Communications* 49, 5856 **2013**.

[10] M. Barroso, S. R. Pendlebury, A. J. Cowan, and J. R. Durrant, “Charge carrier trapping, recombination and transfer in hematite (α-Fe2O3) water splitting photoanodes”, *Chemical Science* 4, 2724–2734 **2013**.

[11] E. Kim, A. Steinbrück, M. T. Buscaglia, V. Buscaglia, T. Pertsch, and R. Grange, “Second-harmonic generation of single BaTiO3 nanoparticles down to 22 nm diameter”, *ACS Nano* 7, 5343–5349 **2013**.

[12] A. Kafizas, R. Godin, and J. R. Durrant, “Charge Carrier Dynamics in Metal Oxide Photoelectrodes for Water Oxidation”, in *Semiconductors for photocatalysis*, 97 (2017), 3–46.

[13] Y. Cui, J. Briscoe, Y. Wang, N. V. Tarakina, and S. Dunn, “Enhanced Photocatalytic Activity of Heterostructured Ferroelectric BaTiO3/α-Fe2O3 and the Significance of Interface Morphology Control”, *ACS Applied Materials & Interfaces* 9, 24518–24526 **2017**.

[14] J. J. Glickstein, P. A. Salvador, and G. S. Rohrer, “Multidomain simulations of coated ferroelectrics exhibiting spatially selective photocatalytic activity with high internal quantum efficiencies”, *J. Mater. Chem. A* 4, 16085–16093 **2016**.

[15] J. J. Glickstein, P. A. Salvador, and G. S. Rohrer, "Computational Model of Domain-Specific Reactivity on Coated Ferroelectric Photocatalysts", *Journal of Physical Chemistry C* 120, 12673–12684 **2016**.

[16] S. Shoaee, J. Briscoe, J. R. Durrant, and S. Dunn, "Acoustic enhancement of polymer/ZnO nanorod photovoltaic device performance", *Advanced Materials* 26, 263–268 **2014**.

[17] J.-i. Fujisawa, T. Eda, and M. Hanaya, "Comparative study of conduction-band and valence-band edges of TiO 2 , SrTiO 3 , and BaTiO 3 by ionization potential measurements", *Chemical Physics Letters* 685, 23–26 **2017**.

[18] M. Grätzel, "Photoelectrochemical cells", *Nature* 414, 338–344 **2001**.

[19] L. Steier, I. Herraiz-Cardona, S. Gimenez, F. Fabregat-Santiago, J. Bisquert, S. D. Tilley, and M. Grätzel, "Understanding the role of underlayers and overlayers in thin film hematite photoanodes", *Advanced Functional Materials* 24, 7681–7688 **2014**.

[20] Z. Huang, Y. Lin, X. Xiang, W. Rodríguez-Córdoba, K. J. McDonald, K. S. Hagen, K.-S. Choi, B. S. Brunschwig, D. G. Musaev, C. L. Hill, D. Wang, and T. Lian, "In situ probe of photocarrier dynamics in water-splitting hematite (α-Fe2O3) electrodes", *Energy & Environmental Science* 5, 8923 **2012**.

[21] S. R. Pendlebury, M. Barroso, A. J. Cowan, K. Sivula, J. Tang, M. Grätzel, D. Klug, and J. R. Durrant, "Dynamics of photogenerated holes in nanocrystalline α-Fe 2 O 3 electrodes for water oxidation probed by transient absorption spectroscopy", *Chem. Commun.* 47, 716–718 **2011**.

Chapter 8

Concluding remarks

> *"We stand now where two roads diverge. But unlike the roads in Robert Frost's familiar poem, they are not equally fair. The road we have long been travelling is deceptively easy, a smooth superhighway on which we progress with great speed, but at its end lies disaster. The other fork of the road — the one less travelled by — offers our last, our only chance to reach a destination that assures the preservation of the earth."*
>
> RACHEL CARSON

8.1 Summary

The aim of this thesis has been to gain an insight into how (and, indeed, if) the internal field associated with ferroelectrics could be used to improve efficiencies of solar energy conversion devices, with a focus on solar-driven water splitting. Archetypal ferroelectric material, $BaTiO_3$, was chosen because of the accessibility of both the ferroelectric (tetragonal) and non-ferroelectric (cubic) phases. This allowed comparison of photophysical and photocatalytic properties between samples with near identical material properties, and deduction of whether any differences could be attributed to the presence (or lack) of an internal electric field. Time-resolved absorption spectroscopy was used on the two forms of this material to first characterise the charge carrier dynamics and determine how they are influenced by ferroelectricity. This knowledge was then used to rationalise differences in photocatalytic rates on predominantly ferro- and non-ferro-electric $BaTiO_3$ surfaces.

In Chapter 4, the charge carrier dynamics of ferroelectric single crystal $BaTiO_3$ were characterised for the first time over fs–ns and µs–s timescales, and compared to electronically and chemically similar — but non-ferroelectric — TiO_2 and $SrTiO_3$ single crystals. At ultrafast timescales, absorption spectra were comparable among the three metal oxides under inert atmosphere. Carrier lifetimes in $BaTiO_3$ matched those in TiO_2 ($\sim$ 7 ns), with bimolecular electron–hole recombination identified as the main decay process. On µs–s timescales (i.e. those expected to be relevant for water oxidation), the spectral signals of photogenerated holes and electrons in $BaTiO_3$ were similar to previously reported metal oxides (blue and NIR regions, respectively). Remarkably, however, carrier lifetimes in single crystal $BaTiO_3$ were found to be $\sim$ 100 ms under inert atmosphere, an order of magnitude longer than single crystal $SrTiO_3$. This indicated that a significant number of photogenerated holes survive to the timescales required for water oxidation.

In Chapter 5, the origin of these long-lived species was investigated. It was found that by 'switching off' the internal field in $BaTiO_3$, recombination rates increased by four orders of magnitude. Transient absorption studies of non-ferroelectric $BaTiO_3$ were conducted by both heating the single crystal to above its Curie temperature and by suppressing the ferroelectric polarisation via nanostructuring. Both approaches resulted in an acceleration in recombination, with lifetimes of just $\sim 10\,\mu s$. This difference was attributed to the polarisation-induced band bending present at the surface of ferroelectric of ferroelectric $BaTiO_3$, which acts as an effective barrier to electron–hole recombination and which decreases in height with increasing temperature as the polarisation strength decreases, before disappearing entirely as the material switches to its non-ferroelectric phase above the Curie temperature. Using literature values, a simple thermodynamic model was proposed to relate the polarisation strength to the band bending height, which was found to agree well with experimentally obtained results. The magnitude of polarisation-induced band bending estimated in $BaTiO_3$ ($\sim$ 0.4 eV) is of similar size to the magnitude of the electrical bias-induced band bending required in non-ferroelectric materials to achieve similar carrier lifetimes, which demonstrates the potential for ferroelectrics to eliminate the need for additional energy inputs in photocatalytic water splitting.

Chapter 6 investigated this theory further by measuring the difference in photocatalytic rates of two $BaTiO_3$ nanopowders with different levels of tetragonal (ferroelectric) content. Time-resolved absorption studies confirmed that a higher number of photogenerated carriers survived to µs–s timescale when a higher proportion of the sample was tetragonal, consistent with lower recombination rates in the ferroelectric phase. The more tetragonal sample was found to outperform the less tetragonal one in both photocatalytic dye degradation and water oxidation under UV light. Photoinduced absorption spectroscopy was used to monitor the water oxidation reaction. It was found that, although a higher concentration of holes accumulated at the surface under illumination in the more tetragonal sample, these holes reacted with the electrolyte at the same rate on both $BaTiO_3$ samples. Thus, a difference in photocatalytic rates was observed not due to a difference in surface structure but due to the slower recombination rates and resultant higher carrier concentration in the more ferroelectric sample. The higher water oxidation rate was, however, slower than an analogous sample of TiO_2 which showed faster recombination rates and lower concentrations of accumulated holes. This important observation indicates that, although ferroelectrics can advantageously influence carrier dynamics they may not necessarily improve conversion efficiencies, and that other factors (such as reaction kinetics) are important considerations in device design.

Finally, in Chapter 7, $BaTiO_3/\alpha$-Fe_2O_3 heterostructures were investigated to explore how a ferroelectric substrate might be able to influence carrier dynamics in a non-ferroelectric, visible light-absorbing top layer. Using transient absorption spectroscopy, photogenerated charges were selectively generated in a thin α-Fe_2O_3 layer and the recombination rates monitored. Although the results presented herein are preliminary, they indicate that carrier dynamics in α-Fe_2O_3 mimic those generated in the substrate when deposited on ferroelectric $BaTiO_3$. Transient absorption spectra and kinetics in α-Fe_2O_3 deposited on energetically comparable TiO_2 single crystals appeared to be several orders of magnitudes shorter than when deposited on $BaTiO_3$. Although previous evidence of ferroelectric substrates influencing the carrier behaviour in thin top layers, this has never been shown spectroscopically. These early studies suggest that whilst ferroelectrics alone may not be able to improve water splitting efficiencies, their ability to drastically reduce electron–hole recombination could be exploited to enhance the performance of currently used materials and devices.

8.2 Outlook

For solar fuels to become part of the essential transition to a low carbon future, their efficiencies must — soon — improve greatly. Whether ferroelectrics will lead to these improvements is currently unclear; as with many research projects, the work carried throughout this PhD has generated as many questions as (if not more than) it has answered. Crucially, however, the answer to the question 'Could ferroelectrics be used to improve solar energy conversions efficiencies?' is clearly not 'No,' based on the research presented in this thesis. The ability of the internal electric field to reduce recombination rates is demonstrably great, improving the yield of charge carriers on timescales relevant to solar-driven water splitting. Thus, more research could prove to be highly valuable for the field.

There are some clear drawbacks of currently known ferroelectrics. $BaTiO_3$, for example, is a wide bandgap semiconductor which oxidises water very slowly (and only in the presence of a sacrificial reagent). Thus, despite the exceptionally long carrier lifetimes, its limitations as a photoanode material are considerable. Finding a suitable visible-light absorbing ferroelectric could perhaps be viewed as the most straightforward solution, however most of the known ferroelectrics have wide bandgaps ($BiFeO_3$ is one of the few 'narrow' bandgap ferroelectrics). A great deal of materials engineering is focussed on synthesising narrow bandgap ferroelectrics using many approaches, including doping to narrow bandgaps, generating polarisation in conventional semiconductors by inducing strain, and creating entirely new materials (often multinary oxides). Whilst this venture may prove fruitful, it seems likely to involve complex — and therefore potentially expensive — synthesis and processing, and yield materials with suboptimal stabilities. This strategy may be more useful for the photovoltaics field; the additional requirement in solar fuels devices of appropriately placed conduction and valence bands mean that the goal of finding an ideal material might be unrealistic.

Using ferroelectrics to improve efficiencies of non-ferroelectrics might therefore be a less demanding task for solar fuels applications. The preliminary results presented here clearly need to be followed up on to gain a true understanding of the extent to which a ferroelectric substrate could improve carrier dynamics in a non-ferroelectric thin film. Assuming the slowing of recombination in the non-ferroelectric top layer can be confirmed, further fundamental studies on these heterojunctions are necessary to establish if the water oxidation properties of, for example, α-Fe_2O_3, could be improved. Beyond this, the next logical step might be the investigation of more 'useful' heterostructures. This could involve the selection of different materials (in which beneficial charge transfer is enabled) to promote different reactions (water oxidation, proton reduction, CO_2 reduction, for example) on the surface. It would also be interesting to investigate the limit of the length scales at which the ferroelectric can influence carrier dynamics. Will similar effects be seen in core-shell nanoparticles? Can the polarisation in ultrathin ferroelectric films penetrate to the same extent? Can the non-ferroelectric be nanostructured and still exert the same influence? Other possibly interesting avenues include investigating ferroelectric domain engineering to optimise the collection of reduction and/or oxidation products, or indeed the ability to switch the reaction promoted on a particular surface through poling/applied bias.

There is clearly much more work to be done in the field of ferroelectrics for solar energy conversion. Fundamental studies like those presented in this thesis can provide the knowledge and building blocks required to design more efficient devices. The hope is that — armed with efficient solar fuels — the transition to a low-carbon future will happen, before it's too late.